A CONTINUOUS IMPINGEMENT MIXING PROCESS FOR EFFECTIVE

DISPERSION OF NANOPARTICLES IN POLYMERS

A Dissertation

by

SANTHANA GOPINATH GANAPATHY SUBRAMANIAN

Submitted to the Office of Graduate Studies of
Texas A&M University
in partial fulfillment of the requirements for the degree of

DOCTOR OF PHILOSOPHY

August 2006

Major Subject: Mechanical Engineering

A CONTINUOUS IMPINGEMENT MIXING PROCESS FOR EFFECTIVE

DISPERSION OF NANOPARTICLES IN POLYMERS

A Dissertation

by

SANTHANA GOPINATH GANAPATHY SUBRAMANIAN

Submitted to the Office of Graduate Studies of
Texas A&M University
in partial fulfillment of the requirements for the degree of

DOCTOR OF PHILOSOPHY

Approved by:

Chair of Committee,	Malcolm J. Andrews
Committee Members,	Jaime C. Grunlan
	Roger J. Morgan
	Othon K. Rediniotis
Head of Department	Dennis O'Neal

August 2006

Major Subject: Mechanical Engineering

ABSTRACT

A Continuous Impingement Mixing Process for

Effective Dispersion of Nanoparticles in Polymers. (August 2006)

Santhana Gopinath Ganapathy Subramanian, B.S., University of Mysore;

M.S., Texas A&M University

Chair of Advisory Committee: Dr. Malcolm J. Andrews

Mixing refers to any process that increases the uniformity of composition and is an integral part of polymer processing. The effective mixing of nanoparticles into polymers continues to be one of the leading problems that limit large scale production of polymer nanocomposites. Impingement mixing is a novel, relatively simple, continuous flow mixing process wherein mixing is accomplished by immersing a high velocity jet in a slower co-flowing stream. The resulting recirculating flow produces an energy cascade that provides a wide range of length scales for efficient mixing. An impingement mixing process was developed and studied through experiments and simulations. Numerical simulations were conducted using FLUENT to understand better the mechanism of operation of the mixer. The formation of a recirculation zone was found to affect the dispersion of nanoparticles. Results of the simulations were compared with experimental data obtained under similar conditions. While this process may be used for any polymer-nanoparticle combination, the primary focus of this study was the dispersion of Single Walled Carbon Nanotubes (SWNTs) in an epoxy matrix. The dispersion of SWNTs was

evaluated by analyzing SEM images of the composites. The image analysis technique used the concept of Shannon Entropy to obtain an index of dispersion that was representative of the degree of mixing. This method of obtaining a dispersion index can be applied to any image analysis technique in which the two components that make up the mixture can be clearly distinguished. The mixing process was also used to disperse SWNTs into a limited number of other polymers. The mixing process is an "enabling" process that may be employed for virtually any polymer-nanoparticle combination. This mixing process was shown to be an effective and efficient means of quickly dispersing nanoparticles in polymers.

DEDICATION

To my parents,

Annapurani and Ganapathy Subramanian

ACKNOWLEDGEMENTS

I would like to express my gratitude to my advisor and committee chair, Dr. Malcolm J. Andrews, for his support and guidance throughout the course of this research. Thanks also to my committee members, Dr. Jaime Grunlan, Dr. Roger Morgan and Dr. Othon Rediniotis, for their helpful input and patience.

Thanks to my colleagues at the Advanced Mixing Laboratory, my friends and the departmental faculty and staff for their support. Thanks to Mr. Thomas Stephens of the Microscopy and Imaging Center at Texas A&M University for his help in SEM imaging. Thanks also to Mr. Yeon Seok Kim of the Polymer Nanocomposites Laboratory for help in preparing and testing the emulsion polymer composites.

TABLE OF CONTENTS

LIST OF FIGURES

LIST OF TABLES

1. INTRODUCTION

1.1   The Problem

Dispersion forces, also known as Van der Waals forces, are present in all materials. The origin of these forces is atomic. An atom contains an equal number of electrons and protons, with electrons orbiting the nucleus. Thus, far away from the atom, the effect of the protons cancels the effect of the electrons, thereby rendering the atom neutral. Close to the atom, however, on the order of the length scale of separation of the electron from the nucleus, the effect of the positive and negative charges can be felt. This positive-negative pair is referred to as a dipole. However, since the electrons are continuously moving around the nucleus, the dipole is not of a constant strength, and keeps changing. This type of dipole is said to be electrodynamic, as opposed to electrostatic. All atoms have electrodynamic dipoles. The presence of these dipoles in all materials thus leads to a net attraction between two atoms, which dies away exponentially as the distance between the two atoms, and is referred to as van der Waals forces. Another force that is of importance when dealing with particulate matter is the body force, due to gravity. While van der Waals forces are proportional to particle diameter, body forces are proportional to the cube of diameter [1]. Thus, for relatively large particles (greater than 10 μm), interparticle forces are small when compared with particle weight, and the effect of van der Waals attractions can be neglected.

_____

This dissertation follows the style of *Nanotechnology*.

Nanoparticles are by definition, a class of materials that have dimensions on the order of nanometers. Thus, they strongly experience van der Waals interactions. The small size of nanoparticles, while providing many interesting properties, thus poses some difficulties. The effective dispersion of nanoparticles into polymer matrices continues to be one of the leading problems that hinders the large-scale production of polymer nanocomposites. Numerous methods are currently in existence for the dispersion of nanoparticles in polymers. Many of them involve the use of high shear [2,3,4]. Ultrasonication is another method by which nanoparticles are dispersed in composites [5,6,7]. Chemical means, like stabilizing the nanoparticles with polymers [8,9,10], or functionalizing them with chemical groups have also been explored [11,12,13]. This dissertation focuses on the development and testing of a simple, cost and energy efficient method of effectively dispersing nanoparticles in polymers.

1.2   *Background and Previous Work*

For decades, materials like metals, fibers and organic fibers have been added to thermoplastic and thermoset polymers to improve one or more of their physical properties. Recently, with advances in synthesizing techniques and the ability to readily characterize materials on the atomic scale has led to interest in adding nanometer sized materials to polymers. The key significance of using nanometer sized filler materials is the dramatically increased surface area that alters the chemistry of these nanoparticles when compared with conventional fillers. Mixing is of critical importance in nanocomposite processing. There are two types of mixing, dispersive and distributive.

Dispersive mixing refers to mixing at a small scale, where the agglomerates of particles are broken up into smaller aggregates, and is characterized by high shear rates. This is the first step to mixing. The second step in obtaining a homogeneous mixture is distributive mixing, that spreads the nanoparticles throughout the matrix, and is characterized by low shear rates. Distributive mixing is relatively simple. Dispersive mixing, on the other hand, requires large amounts of energy input. Many different methods have been used to accomplish dispersive mixing. R. Andrews et al. have used a Haake Polylab shear mixer, to mix Multi-Wall Carbon Nanotubes with polypropylene and polystyrene where the polymer and nanoparticles are mixed by the action of counter rotating blades [14]. Wilson et al. have used a banbury mixer to mix iron nanoparticles with Poly Methyl Methacrylate [15]. Sennett et al. have used a twin screw extruder to disperse Single Walled Carbon Nanotubes in Polycarbonate [16]. Other processes are in existence and will not be discussed in detail, as there are too many of them. Many of the mixing processes described in the literature are batch processes that handle small volumes of material. These processes may in principle be geometrically scaled-up to handle large quantities of material, but would correspond to a proportional increase in the energy required to run the process. Some of the continuous processes, like twin screw extruders, are relatively slow, with a small output rate.

1.3   Ducted Jets – An Overview

This section provides a brief introduction to ducted jets, as they form the basis of the impingement mixer that is studied in this research. This section covers key points about ducted jets that is available in the literature.

1.3.1   Basic Principle

Ducted jets were studied in the mid 1950s [17,18] both experimentally and theoretically. A theoretical description that covered free, plane and confined jets was outlined by Hill [19]. Ducted jets consist of a small diameter nozzle (jet) placed coaxially with a larger duct (mixing tube, co-flowing stream). The jet velocity is typically higher than the co-flowing stream velocity. Figure 1.1 shows the streamlines obtained in a confined jet and the different flow regimes that can be distinguished. If the effects of the wall boundary layers are ignored, four idealized flow regimes can be distinguished: A) A transition regime, where the jet velocity is nearly constant. This regime is quite short, on the order of a few nozzle diameters. B) A regime where the jet starts to entrain fluid from the co-flowing stream. In this regime, the external flow from the co-flowing stream may be considered a potential flow. The jet velocity and shear stress distributions may be considered self preserving. The entrainment of fluid from the co-flowing stream by the jet is rapid enough to reduce the free stream velocity and establish a positive pressure gradient along the axial direction. C) A possible recirculation zone. The jet spreads to hit the walls of the co-flowing stream. If the jet entrains all the co-flowing stream fluid before spreading to the wall, a zone of recirculating fluid will be formed. The flow outside of the jet can no longer be considered potential, due to fluid recirculating through the jet itself. D) The fully developed regime, where the jet spreads to hit the walls of the duct and the flow velocity distribution becomes parabolic.
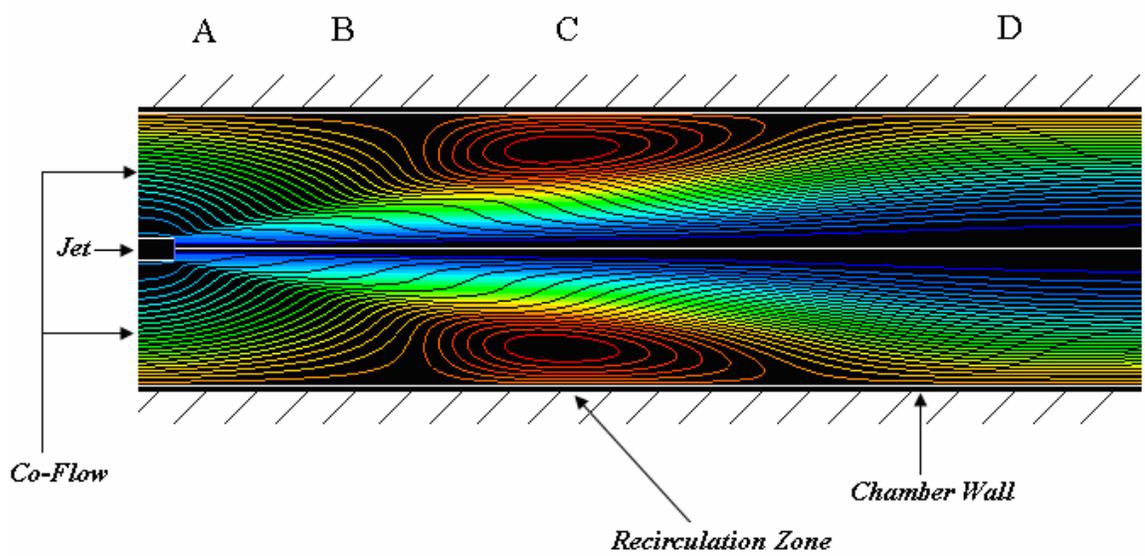
Figure 1.1   Schematic of flow regimes obtained in ducted streams

The recirculation zone is characterized by high velocity gradients and increases the residence time of the fluid within the mixer. These two characteristics of the recirculation zone make it particularly suitable for efficient mixing. The high-velocity jet induces a negative pressure gradient on the co-flowing stream, thereby pulling fluid from the co-flowing stream into the jet. This property is used to pump particulate matter and also in spray painting. Jets continue to be used in fuel injectors for efficient atomization of fuel and to improve the mixing of air and fuel. Such confined jets are also used in pumping applications.

There are two important parameters that are involved in confined jets. The first of these is called the Craya-Curtet number (C_t), in honor of Antoine Craya and Roger Curtet. It is a measure of the ratio of the jet momentum to the co-flowing stream momentum. The second parameter is the Reynolds number of the jet (Re_j). The velocity of the jet provides the energy that is required for mixing, and the Reynolds number is directly proportional to the square root of the energy contained in the jet. These non-dimensional numbers and their effect will be discussed in the following sections.

1.3.2   Craya-Curtet Number and Its Significance

The similarity parameter for jets in ducted streams has been defined variously by researchers, and they are listed below. The original definition proposed by Craya and Curtet follows from the Reynolds Averaged Navier Stokes (RANS) equations and is given by [17]

$$m = \frac{Mh^2}{Q^2} \qquad (1.1)$$

where   Q   = total fluid discharge

            M   = sum of momentum flux and pressure forces.

            h   = height of chamber (radius of co-flowing stream)

Other definitions of the similarity parameter are summarized in Table 1.1. The parameters, C_t, m and H are related by

$$H = \left(1 + 2/C_t^2\right)^{-0.5} \qquad (1.2)$$

$$C_t = m^{-0.5} \qquad (1.3)$$

It is worthwhile noting that all these definitions, in one way or another, consider the similarity parameter to be the ratio of the co-flowing stream momentum to the jet momentum. Except the definition by Brighton and Exley [20], all the definitions are complicated integral definitions and cannot be evaluated without knowledge of the velocity field that is present in the duct. Brighton and Exley proposed an algebraic definition that can readily be computed. Furthermore, the velocities used in this definition are fluid velocities at the exit plane of the jet, which, from an experimental point of view, can readily be set. This is the definition that will be used in this dissertation.

Table 1.1   Definitions of similarity parameter

Authors	Definition	Explanation of Terms
Hill [19]	$H = \dfrac{1}{\sqrt{2\pi}} \dfrac{Q}{R_o \sqrt{W/\rho}}$	$W = \displaystyle\int_0^{R_o} \left(P + \rho u^2\right) r\,dr$ Q = Total discharge P = Pressure ρ = Density R_o = Radius of co-flow duct
Woodfield et al. [21]	$C_t = \dfrac{U_o}{\sqrt{U_d^2 - 0.5 U_o^2}}$	$U_d^2 = \dfrac{1}{A_o} \displaystyle\int_{A_o} (u^2 - 0.5 U_f^2)\,dA$ $U_o = \dfrac{1}{A_o} \displaystyle\int_{A_o} u\,dA$ u = velocity A_o = Area of co-flowing stream U_f = Inlet velocity of the co-flowing stream
Becker et al. [22]	$m = \dfrac{u_d^2 - 0.5 u_k^2}{u_k^2}$	$u_k = -\dfrac{1}{A_o} \displaystyle\int_{A_o} \mathbf{n} \bullet \mathbf{u}\,dA_o$ $u_d^2 = -\dfrac{1}{A_o} \left\| \displaystyle\int_{A_o} (\mathbf{n} \bullet \mathbf{uu} - \mathbf{0.5u_{f,o}} \bullet \mathbf{u_{f,o}n})\,dA_o \right\|$ u = velocity A_o = area of exit plane of jet $u_{f,o}$ = inlet velocity of co-flowing stream
Brighton and Exley [20]	$C_t = \dfrac{U_r D_r^2 - D_r^2 + 1}{\sqrt{\dfrac{1}{2}\left[D_r^2 U_r^2 - D_r^4 - 1\right]}}$	Velocity Ratio $U_r = u_j / u_{cf}$ Diameter Ratio $D_r = D_j / D_{cf}$ u_j = Velocity of fluid exiting the jet u_c = Velocity of co-flowing stream of fluid D_j = Diameter of jet D_{cf} = Diameter of co-flowing stream

It has been observed experimentally that there exists a critical value of the Craya-Curtet Number (C_{tc}). If the operating C_t is greater than C_{tc}, the momentum demands of the jet are met by the co-flowing stream momentum, and the jet hits the walls of the duct before it has consumed all the fluid from the co-flowing stream. Thus, no recirculation zone is formed. If, however, the operating C_t is lower than the critical C_t, the jet still has some momentum left over after it has consumed all the co-flowing stream fluid, thereby leading to the formation of a recirculation zone. C_{tc} has been reported variously in the literature. Barchilon and Curtet [23] have suggested that $C_{tc} \approx 0.976$. Becker et al. [22] found $C_{tc} \approx 0.75$. Revuelta et al. [24] have found $C_{tc} = 0.77$ for a parabolic co-flow.

Once the recirculation zone is formed, both experiments and computations show that a reduction of C_t increases the size of the recirculation zone. The increased size of the recirculation zone, therefore, increases the residence time of the fluid within the mixer promoting mixing. The start of the recirculation zone is taken to be the point of separation of the co-flowing stream from the chamber walls, while the end is taken to be the point of re-attachment to the chamber wall. The effect of C_t variation on the start and end of the recirculation zone has been reported differently by different researchers. Woodfield et al. [20] have reported that the point of separation remains fixed, while the point of reattachment moves further downstream as C_t is lowered. Barchilon and Curtet [23] have found that the point of separation moves upstream, while the point of reattachment remains fixed as C_t is lowered. Brighton and Exley [20] as well as Revuelta

et al. [24] have noted an appreciable variation in both separation and reattachment points of the co-flow with C_t.

1.3.3   Reynolds Number and Its Significance

Reynolds number is the well-known ratio of inertial to viscous forces in a fluid flow, and is given by

$$\mathrm{Re} = \frac{\rho u D}{\mu} \qquad\qquad (1.4)$$

where

ρ = density of fluid

u   = mean velocity

D   = characteristic length-scale of the flow

μ = viscosity of fluid

For the case of jets in ducted streams, a jet Reynolds number (Re_j) can be computed by using the jet exit velocity as the mean velocity, and the diameter of the jet as the characteristic length-scale of the flow. The energy required for mixing is provided by the high velocity of the jet. Thus, the jet Reynolds number is directly proportional to the square root of the energy that is supplied to the fluid system for mixing. Therefore, intuitively, the jet Reynolds number is a dimensionless parameter that is of importance. The Reynolds number can be computed in another way, and is referred to as the tube Reynolds number. In this case, a mean velocity is computed by dividing the total

discharge (Q_{jet} + $Q_{co\text{-}flow}$) by the cross-sectional area of the co-flowing duct and taking the characteristic length scale to be the diameter of the co-flowing duct. This is referred to as the tube Reynolds number, and is a measure of turbulence in the fully developed regime of the flow. It must be noted, however, that for a given geometry, setting the jet Reynolds number and the Craya-Curtet number automatically fixes the tube Reynolds number, and therefore, both these definitions are equivalent.

The three regions of flow that may be identified are laminar, transitional and turbulent, depending on the jet Reynolds number. Varying limits have been reported for each flow regime. Lane and Rice [25] offered

$Re_j < 100$ Laminar Jet

$100 < Re_j < 2000$ Transitional Jet

$Re_j > 2000$ Turbulent Jet

The behavior of each of these jets is shown in Figure 1.2. The laminar jet is stable, with most flow instabilities being rapidly damped. Transitional jets are initially stable, but at some point in the flow, break down. For these jets, as Re_j is increased, the turbulent zone moves closer to the nozzle. Turbulent jets show the growth of turbulent eddies just beyond the jet nozzle. The velocity is no longer constant, and fluctuates back and forth. There exists a range of eddy sizes. While an eddy eludes precise definition, it is conceived to be a turbulent motion localized over a certain region that is at least moderately coherent over this region.
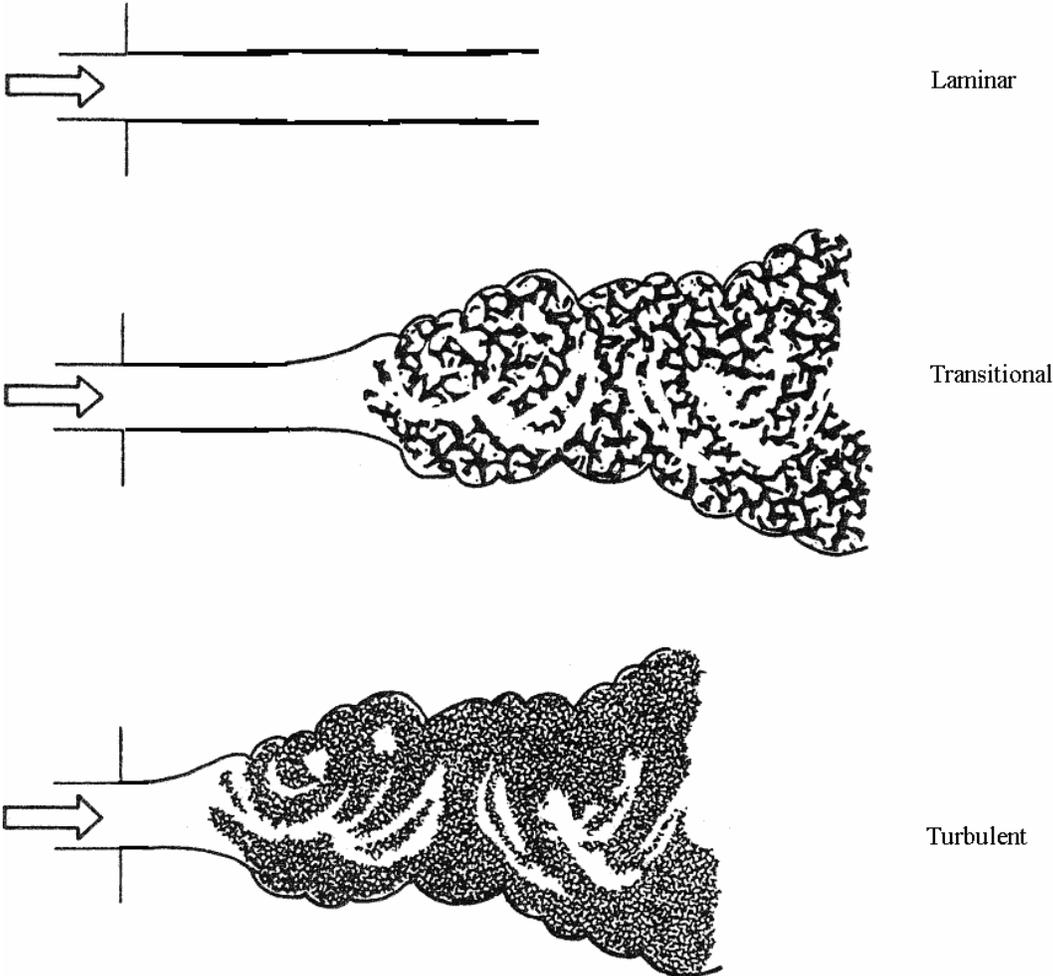
Figure 1.2　　Laminar, transitional and turbulent jet flows

Turbulent motions range in size from the width of the flow to much smaller scales, which can become progressively smaller as the Reynolds number increases. The effect of viscosity becomes important only at the smallest length scales, and it is these eddies that dissipate the energy of the fluid flow (and are consequently referred to as the dissipative length scale).

A combination of these factors promotes mixing in turbulent flow, thus making jets quite suitable for industrial operations where good mixing is desirable. In ducted jets, the Reynolds number has a significant effect on the recirculation zone. It has been shown by Woodfield et al. [20] that an increase in Reynolds number increases the size of the recirculation zone and also moves the start of the recirculation zone further downstream. The increase in size of the recirculation zone, as noted in the previous section on Craya-Curtet number, further increases residence time of fluid within the mixer providing for better mixing. Figure 1.3 shows plots of the axial velocity at 99.9% of the co-flowing stream radius as a function of downstream distance, as computed from 2-D simulations as outlined in section 4.1. The change of the velocity from positive to negative indicates the start of the recirculation zone, while the change from negative to positive indicates the end. In plot (a), Re_j was held constant while C_t was varied from 2.18 to 0.33. As C_t was lowered, we see that the start of the recirculation zone moves upstream, while the end moves slightly downstream. In plot (b), Re_j was varied, while C_t was held constant at 0.65. In this case, we see that an increase in Re_j moves the end of the recirculation zone slightly downstream, while the start is not affected significantly.
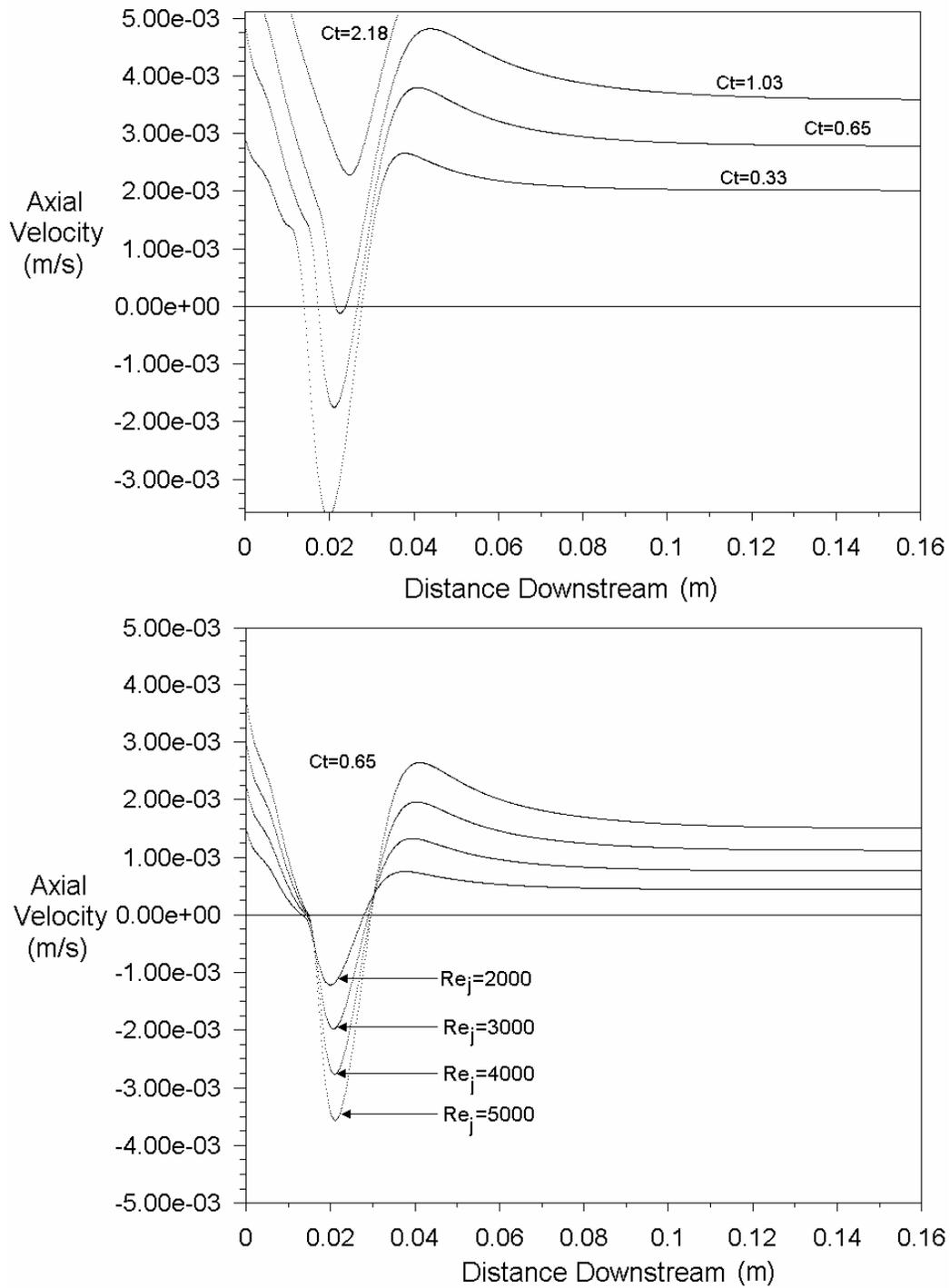
Figure 1.3   Axial velocity near the wall for different C_t and Re_j

We also note that the velocity gradients near the wall increase with Reynolds number. These two plots illustrate the behaviour of the recirculation zone in ducted jets as the governing parameters are varied.

1.4   Image Analysis

1.4.1   Overview

Digital image processing is becoming a widespread technique to analyze scientific data in many disciplines. Human vision, by itself, is inadequate to provide a quantitative description of the image properties. For example, in fluid flow, human vision my be able to distinguish between two types of flow, but cannot determine the velocities. An image is a flat object whose brightness or color may vary from point to point. The variation may be represented mathematically as f(x,y), a real valued function of two spatial variables. A digital image is a discretization of the real image, both in spatial coordinates and brightness. Thus, an image can be considered as a matrix whose indices refer to a particular point, while the element values refer to the brightness of that point. Each value represents the smallest picture element (or pixel). The resolution of an image is the number of pixels present in a particular region.

Techniques in digital image processing may be divided into four principal categories [26]: image digitization, image enhancement and restoration, image coding and image segmentation, representation and description. Digitization is the conversion of continuous brightness and spatial coordinates into discrete components. This category

includes the mathematical treatment of digitization processes and its effect on image quality. Image enhancement and restoration techniques deal with the improvement of a given image for either human or machine perception. These techniques may be used to obtain data from experiments that are too expensive or delicate to recreate. Image encoding procedures reduce the amount of space a digital image takes without significant loss of data. Segmentation is a process that subdivides an image into its constituent regions or objects. Segmentation deals with the changes in grayscale values to extract information from an image, and is an integral part in image representation, because at this step, objects are extracted from the image for further processing.

An important approach to image representation is to quantify the texture content. Although no formal definition of texture exists, it can be thought of as a measure of smoothness, roughness and regularity. There are three methods of measuring texture, namely statistical, structural and spectral. Statistical methods are the simplest methods of describing texture, and use statistical moments of the gray-level histogram of an image or region. Structural approaches identify a "primitive" or a building block of an image (for example, bricks may be thought of as primitives that build a wall), and describe the entire image using these primitives. Spectral approaches use the Fourier spectrum of an image to describe the 2D periodicity of an image, and are useful where global texture patterns are difficult to detect using spatial methods.

Image entropy is a statistical measure of texture and is defined in a manner similar to thermodynamic entropy. Entropic measures are used in many fields of science, like statistical mechanics [27,28], biology and medicine [29,30,31], cognitive science [32,33], geology [34] and pattern recognition [35,36]. Entropic image analysis has also been used to assess the level of image compression [37]. Following Alemaskin et al. [38] and Camesasca et al. [39], an entropy-based measure of mixing was implemented to assess the dispersion of SWNTs in epoxy. A description of the technique used is provided in the next section.

1.4.2 An Entropic Measure of Mixing

Shannon entropy is defined in terms of the probabilities p_j of M discrete random events as [40]

$$S = -\sum_{j=1}^{M} p_j \ln p_j \tag{1.5}$$

with

$$\lim_{p_j \to 0}[p_j \ln p_j] = 0 \tag{1.6}$$

Equation (1.5) is a unique representation of entropy. The base of the logarithm is arbitrary, as long as consistency is maintained. In this dissertation, the natural logarithm will be used. The following requirements are satisfied: the sum of all $p_j = 1$; the lowest entropy (S=0) corresponds to one of the p's being equal to 1, and the rest equal to 0; the highest entropy corresponds to all the p's being equal; S is additive over partitions of outcomes. For purposes of measuring dispersion of nanoparticles in a host matrix,

images of the area of interest (in this case, SEM images) are obtained and the concept of entropy may be applied to these images in either of two ways, as outlined below.

Table 1.2 schematically shows the algorithm for both methods.

In the first method, (referred to here as method A), the pixel grayscale value is treated as the random event. In this case, the image is sub-divided into a number of K x K squares. For each square, the probability over the range of grayscale values and the entropy are computed as

$$P(b) = \frac{N(b)}{K^2} \tag{1.7}$$

$$E = -\sum_{b=0}^{255} P(b) \log_2[P(b)] \tag{1.8}$$

where

      b   = 0,1,2,.......255 for an 8-bit grayscale image

      P(b) = probability of occurrence of grayscale value b

      N(b) = number of occurrences of grayscale value b

The computed entropy for each square is then assigned to the central pixel of the square. This process is repeated for the whole image. The resulting image provides a map of the texture of the original image. Histograms of entropy may be used to determine the frequency of occurrence of regions with different textures.

Table 1.2   Two algorithms for entropic measure of mixing

METHOD A	METHOD B
1.Isolate a K x K square of the image (3 x 3 in example)	1.Distinguish particles from host matrix
	2.Assign particles a pixel intensity value of 255, and host matrix pixels an intensity of 0
$\begin{array}{ccc} G_1 & G_2 & G_3 \\ G_4 & G_5 & G_6 \\ G_7 & G_8 & G_9 \end{array}$	3.Let T=total number of particles in space of interest
	4.Divide the space of interest into M equal sized bins
2.Compute the probability of each grayscale value in the range [0,255] as P(b)=N(b)/9	5.For each bin, compute $P_i=N_i/T$, where N_i = number of particles in bin i
3.Compute the entropy over the range of grayscale values	6.Compute entropy for the whole space of interest
4.Assign this value to the central pixel (G_5)	
5.Repeat for whole image	
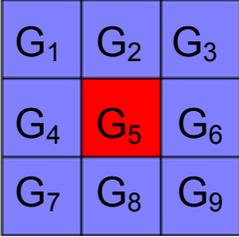
This is a straightforward method that does not require any image pre-processing before the analysis is carried out.

The second method (referred to here as method B) requires that the nanoparticles be distinguishable from the polymer background. Here, the space of interest is divided into M equal area square "bins" and the probability p_j for each bin is estimated by the particle concentration in each bin. The variable S (entropy) can take on values between 0 and $\ln(M)$. The worst mixing is characterized by S=0 (when all the particles are in one bin and the other bins are empty) and the best mixing is characterized by $S=\ln(M)$ (when all bins contain equal number of particles). Thus, the computed entropy can be normalized by $\ln(M)$ to yield an index of mixing between 0 and 1, where 1 corresponds to the best mixing, and 0 to the worst. In this case, entropy can therefore be thought of as a measure of the homogeneity of distribution of particles within a matrix.

Preliminary analyses were conducted on SEM images using the first method and were found to be satisfactory. The second method was then used to assign an index of dispersion for SWNTs in epoxy. From a molecular point of view, a mixture of nanoparticles in a matrix can never attain perfect homogeneity. Thus, the degree of mixing becomes a relative concept. Therefore, an evaluation of mixing at the length scale of the nanoparticles is nearly impossible, and probably unnecessary. However, the degree of mixing may be evaluated at length scales greater than the nanoparticle size. The length scale at which the entropy is evaluated is governed by the bin size. The effect

of variation of the bin size was studied, and the image analysis technique was validated using simulated SEM images generated by executing random walks. The parameters governing the random walks were controlled, and this validation is discussed further in section 2.7. A generalization of the above analysis can be made for systems containing more than one type of particle, and has indeed been done by Alemaskin et al. in [38]. For purposes of this study, however, characterization of mixing with a single type of nanoparticle was sufficient.

The purpose of this analysis was neither to determine the morphology of the SWNT clusters, nor to probe the formation of the tangled network of SWNTs, but rather to analyze their dispersion. Thus, of interest here is the dispersion of the material photographed and consequently we refer to it as the number of occupied pixels. Our goal is a dispersion measure that can be made generic and not limited to the measurement of dispersion of SWNTs in epoxy.

2. EXPERIMENTAL SETUP AND DIAGNOSTICS

2.1 Introduction

A description of the mixer and the mixing process is detailed in the following sections. A solids conveying eductor was purchased from Fox valve and was used for preliminary testing. This was found to be inadequate for operation at low C_t. Other problems were associated with it, and are outlined in the following sections. A series of mixers were designed and machined, although only the simplest configuration was experimentally tested. As outlined previously, the important parameters are the Reynolds number and the Craya-Curtet number. A setup that allowed the jet and co-flowing stream velocities to be varied was designed and calibrated. This setup was then used to mix SWNTs with a series of polymers. The composites were imaged using a Field Emission SEM. In the case of SWNTs in epoxy, the dispersion was quantified using the concept of Shannon entropy. The structural and electrical properties of the composites were also evaluated.

2.2 Description of Mixer Design

Figure 2.1 shows a schematic of different mixer designs and the nomenclature used. The simplest configuration is shown in Figure 2.1 (a). In this configuration, there is a single jet exiting into a straight co-flowing stream. This is the simplest configuration possible.

Co-Flow

Mixing Tube

Jet

(A)

(B)

(C)

(D)
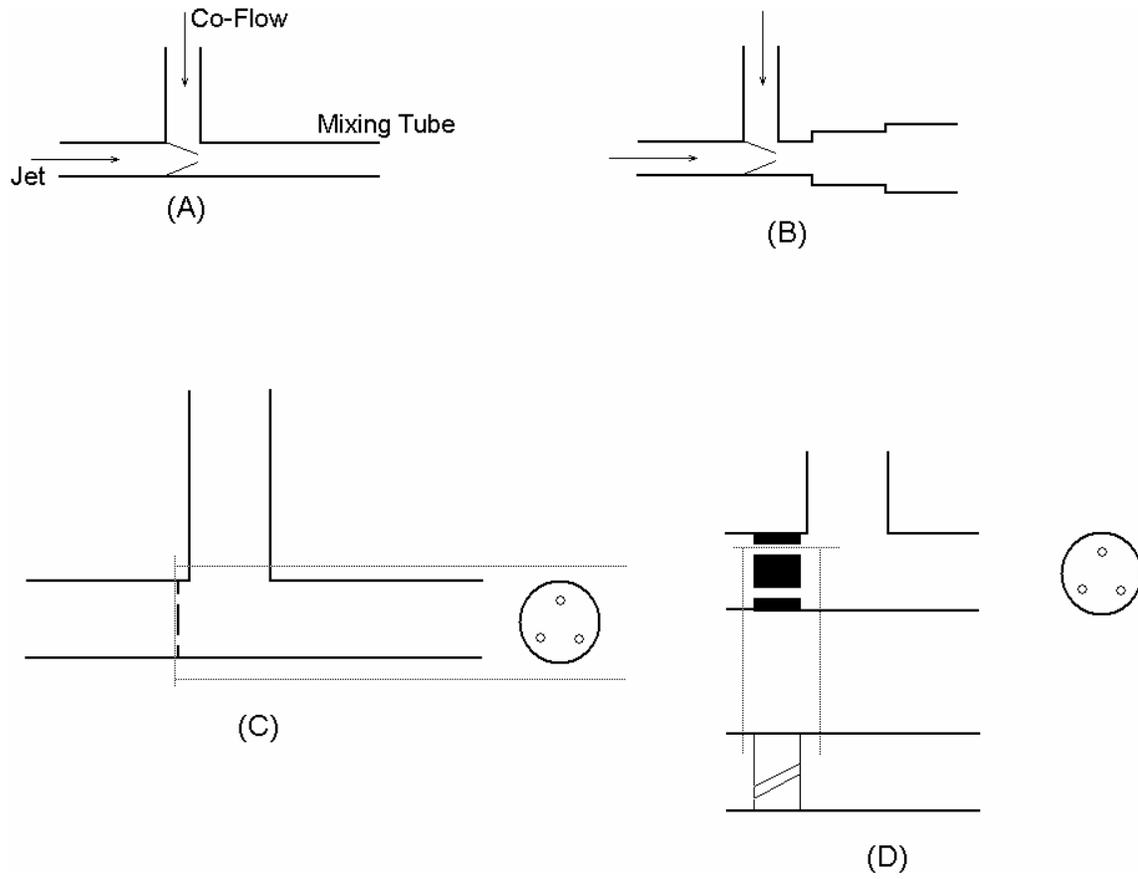
Figure 2.1   Design variations for mixers

Figure 2.1 (b) shows a single jet exiting into a co-flowing stream that has an expansion chamber. In this configuration, recirculation eddies form near the steps, promoting mixing. Figure 2.1 (c) shows a mixer having multiple jets. Figure 2.1 (d) shows a mixer having multiple jets with swirl. In both these configurations, the presence of multiple jets leads to the formation of more than one recirculation zone, promoting mixing. In the mixer having jets with swirl, the velocity of the jets in the axial direction is reduced, while their momentum remains the same. This results in a further increase of the residence time of the fluid within the mixer, leading to better mixing. This dissertation addresses only the first kind of design, i.e. the simplest design. Figure 2.2 shows the dimensions of the mixer that was used in this study. This design addressed some of the problems associated with the commercial solids conveying eductor that was used for preliminary tests. The commercial eductor was similar in design to the mixer we used. It had a diameter ratio (D_j/D_{cf}) of 0.5. The eductor was performing well over most C_t at low flow rates ($u_j \sim 5$ ms^{-1}; Re$_j \sim 75$). Once Re$_j$ was increased to over 1000, the eductor started to clog at $C_t \sim 1$. This was attributed to low D_{cf}. In the new design, D_{cf} was taken to be 0.375", and this fixed the problem of mixer clogging at high Re$_j$ and low C_t. The commercial eductor also had a low L/D ratio of mixing tube (about 1). This caused the jet to exit the mixer in the form of a messy spray when no extra tubing was attached. In the new design, the L/D was taken to be 13, eliminating the messy spray.
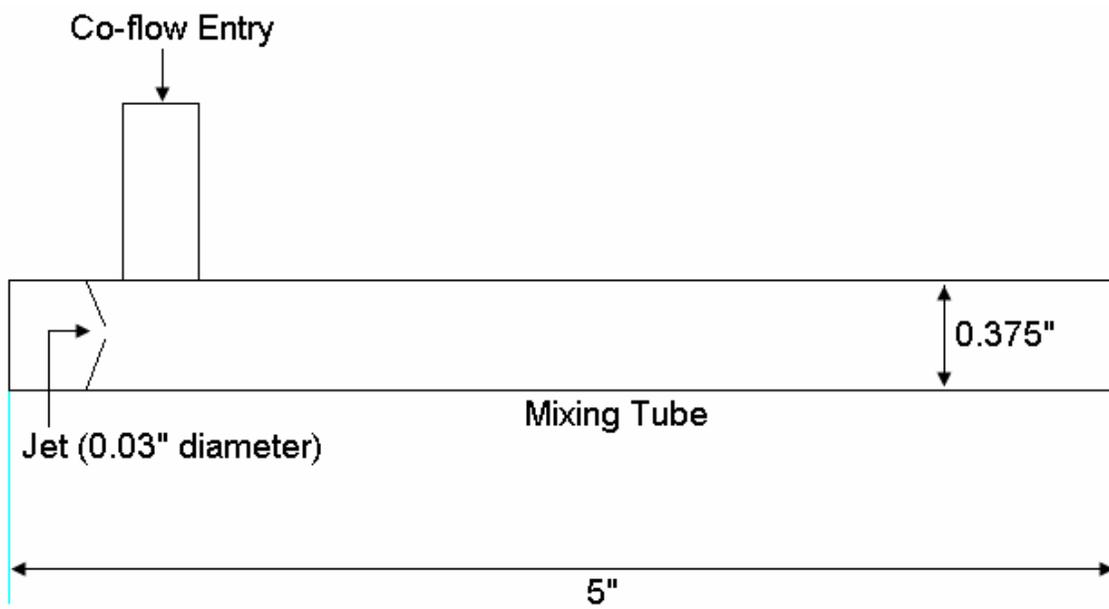
Figure 2.2   Dimensions of mixer used

2.3   *Mixing Setup and Calibration*

Figure 2.3 shows a schematic of the setup used for the experiments. Two fluid reservoirs (Jet reservoir and Co-Flow reservoir) hold the fluid before mixing. These reservoirs were connected to the mixer by means of PVC tubing. The other ends of the reservoirs were connected to high pressure air lines through pressure regulators. The driving force for the mixing was provided by air pressure that was varied by means of the pressure regulators. A choke valve was used to restrict flow to the co-flowing stream. Two shut-off valves allow the flow to be started and stopped. The variation in driving pressure, in conjunction with the use of the choke valve allowed variation of Re and C_t.

Calibration was performed at pressures in the range 20-90 psi for each of the pressure regulators, and for four different positions of the choke valve (¼, ½, ¾ and fully open). The fluid reservoirs were filled with fluid to a known height. The maximum pressure due to liquid head was 0.142 psi, and was neglected. The system was pressurized, and both shut-off valves were opened simultaneously. The time taken for the first reservoir to empty was measured. The height of fluid drained from the other reservoir in this time was also measured. Flow rates through each stream were thus computed and used in conjunction with the mixer geometry to compute C_t and Re_j. Since the choke valve had the most uncertain setting, for each combination of pressures, the choke valve was run through the range of positions. This procedure was repeated thrice, and the average flow rates for each setting were determined.
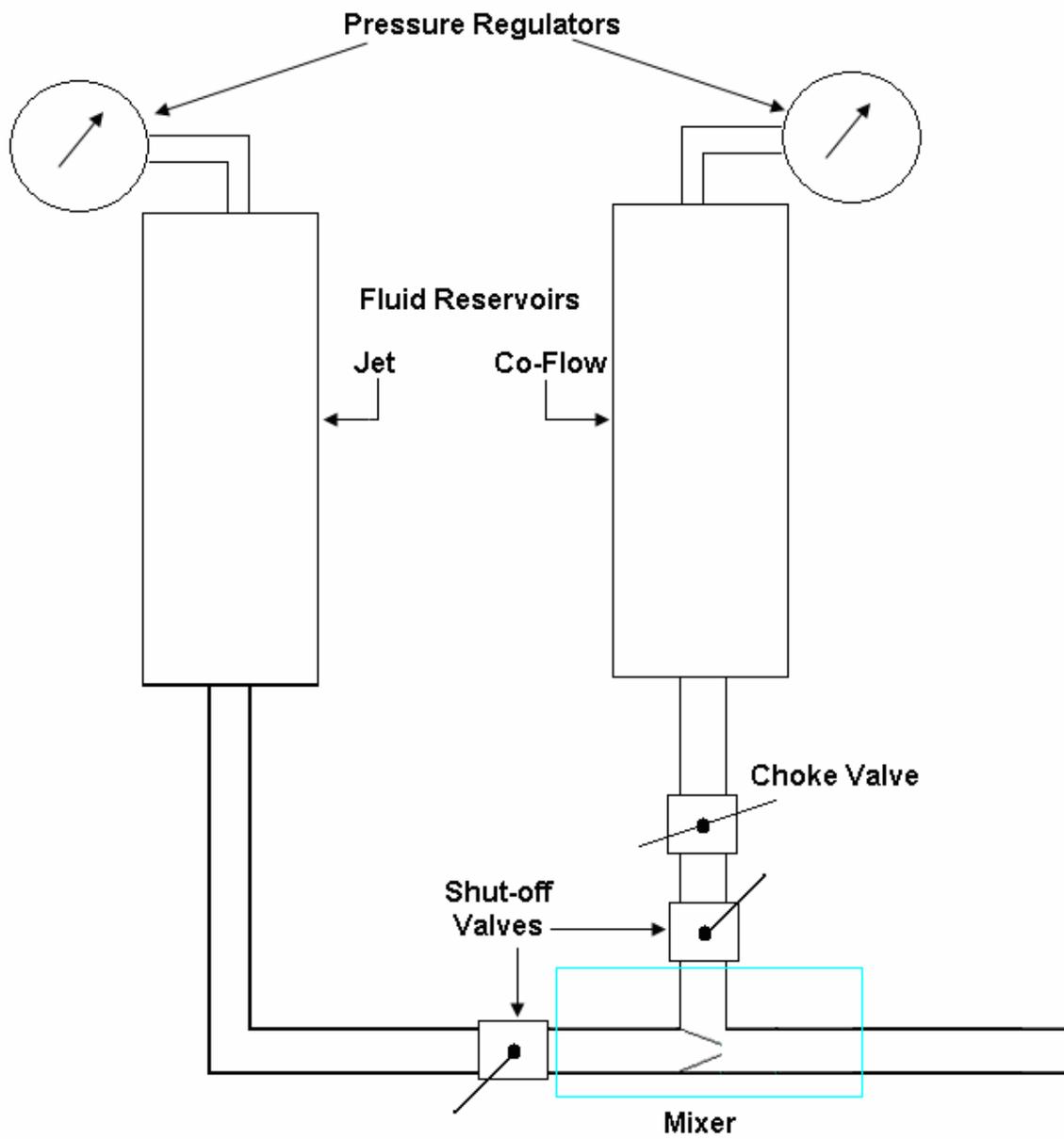
Figure 2.3   Schematic of mixing setup

The range of C_t obtained in this fashion was from 0.26 to 2.18. The maximum Re_j that was obtained was 4500. The ratio of flow rates for each calibration point was also calculated. The accuracy of this calibration was verified during experiments. For each pressure/choke valve setting combination, the ratio of flow rates through each of the streams was known. Each reservoir was filled with a quantity of fluid in that ratio, and it was observed that both reservoirs consistently emptied out at the same time.

Table 2.1 summarizes the different cases that were considered, and the processing parameters.

2.4   *Experimental Procedure and Challenges*

2.4.1   *Stabilizing SWNTs with PVP*

SWNTs are known to be insoluble in a wide variety of solvents. Chemical modification (Fluorination, side wall functionalization, etc.) is one of the ways of making the SWNTs soluble in liquids. This method, however, chemically modifies the structure of the SWNTs, reducing their potential. Another method of stabilizing SWNTs is by wrapping them with polymers. PVP is one such polymer that has been used in the past [41]. Other polymers that have successfully been used include Poly Styrene Sulphonate and Bovine Serum Albumin [42]. Significant research has been focused on the use of stabilizing agents to use the suspended SWNTs in ink-based systems, which are being used for thermal management [43], optical [44] and actuator films [45]. In the present study, PVP

(M_W=10,000) was purchased from Aldrich. A 2 wt% solution of PVP was prepared by stirring the required amount of PVP in distilled water for 24 hours.

Table 2.1   Summary of experiments

Case	C_t	Re_j	Method of Analysis	Comments
Stabilizing SWNTs in PVP solution	0.65	500	TEM	Concentration of SWNTs was 2 wt%
SWNTs in Epoxy	0.33, 0.65, 1.03, 2.18	4000	SEM, Electrical Conductivity, Tensile testing	Composites with various SWNT concentrations were prepared, from 0.0125 to 0.2 wt%, for each C_t. PVP-stabilized SWNTs were also mixed with epoxy
SWNT-Elastomer	2.18	500	Tensile testing	We were unable to perform EM imaging, as the electron beam caused the elastomer to evaporate even at low accelerating voltages
SWNT-Emulsion Polymer	0.65	500	Electrical conductivity	The image analysis was not able to isolate the SWNTs from the emulsion polymer

SWNTs were added to the solution and stirred by hand until the SWNTs were submerged. This resulting mixture was driven through the mixer once at C_t=0.65 to obtain SWNTs stabilized with PVP.

2.4.2 SWNT-Epoxy Composites

SWNT-Epoxy composites were the most extensively studied system in the present work. The epoxy resin used in this study was Di Glicidyl Ether of Bisphenol A (DGEBA), commercially referred to as EPON 862 resin. This resin, along with the curing agent (diethyl toluene diamine) was purchased from Miller-Stephenson. The curing procedure specified by the manufacturer was to heat the epoxy + curing agent in the ratio 1:0.264 to 120°C for 4 hours. Plain EPON 862 resin has a viscosity of 35 P and addition of SWNTs to the epoxy further increases its viscosity, which makes it difficult to handle. A suitable solvent was used to dilute the epoxy prior to addition of SWNTs. Equal volumes of solvent (20% toluene + 80% acetone) and EPON resin were mixed to bring the system viscosity down to 5.1 cP. The diluted mixture of epoxy and SWNTs was driven through the calibrated impingement mixer at a range of different C_t. It was thought initially that the solvent would evaporate before the polymer molecules had completely cross-linked, and thus the required amount of curing agent was added, and the mixture was placed in an oven at 120°C for 4 hours. This, however, was not the case. The presence of solvent caused the mixture to boil, and the finished product had the visual appearance of foam. Thus, it was decided to evaporate the solvent from the epoxy before adding the curing agent.

The time required for the solvent to evaporate was experimentally determined. Control specimens were prepared without the use of any solvent. The ultimate tensile strength of these specimens was comparable with that reported by the manufacturer. Plain epoxy+solvent was placed on a hot-plate at $60^{o}C$ for times ranging from 1-10 hours. Curing agent was added to the resulting liquid and the mixture was cured. Some of the specimens foamed, indicating that all the solvent had not evaporated before the polymer completely cross linked. The specimens that did not foam were tested in tension. It was found that specimens that were prepared by evaporating the solvent for 6 hours or more had an ultimate tensile strength comparable with that of the control specimens. Thus, the output of the impingement mixer (epoxy + solvent + SWNTs) was stirred on a hotplate at $60^{o}C$ for 6 hours to evaporate the solvent. Afterwards, the curing agent was added and hand-mixed thoroughly. The liquid was then poured into a mold and cured in a furnace at $120^{o}C$ for 4 hours. The effect of the high shear within the mixer upon the physical properties of the epoxy was also tested by running plain epoxy through the mixer, curing it, and then testing the specimens in tension. Figure 2.4 shows a comparison of three kinds of specimens that were prepared. The first was plain epoxy without any mixing or solvent. This was the control specimen. The second specimen was prepared using solvent, while the third specimen was prepared using solvent and running the epoxy through the mixer four times. It is seen that the effect of processing has only a minor effect on the tensile characteristics of the epoxy.
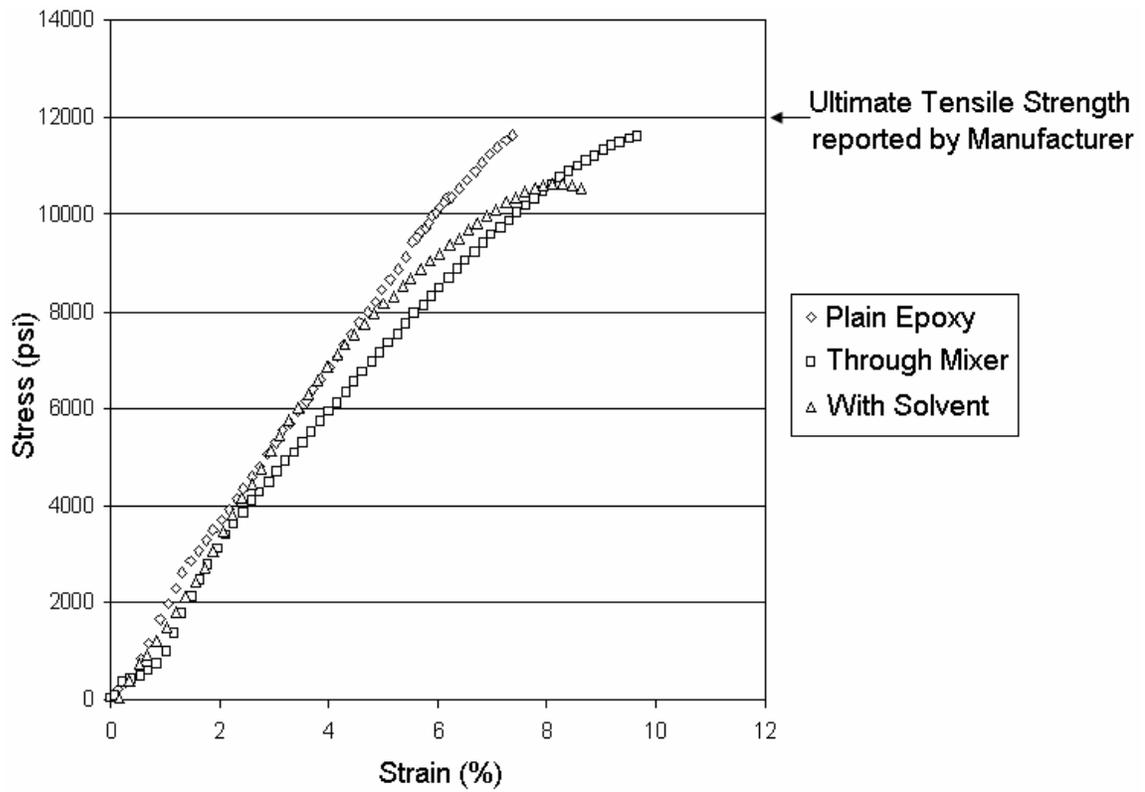
Figure 2.4   Stress vs. strain of plain epoxy

We found that this procedure of curing the epoxy had problems at higher percentages of SWNT loading. In particular, upon evaporation of the solvent, the viscosity of epoxy and SWNTs was such that mixing of the curing agent led to the formation of voids due to air entrainment. Instead, the curing agent was added to the solvent before the liquid was driven through the impingement mixer. In this modified procedure, output from the mixer was poured into the mold and placed in a vacuum at room temperature. The chamber pressure was reduced to below the vapor pressure of the solvent to increase the evaporation rate of acetone and toluene. The resulting mixture was heat-treated for 4 h at 120°C. This procedure presented some problems. In particular, the specimens that were prepared in this fashion had an ultimate tensile strength lower than that of the test specimens. Heating the mold and applying a vacuum at the same time was attempted, but this resulted in the epoxy curing rapidly, trapping the solvent molecules within the matrix. Thus, for this study, SWNT loadings were restricted to 0.2 wt%.

PVP-stabilized SWNTs were also used to prepare epoxy composites. Attempts were made to add the epoxy directly to the suspension of SWNTs in PVP solution, but the epoxy did not adhere to the SWNTs. To overcome this problem, the water was first evaporated from the suspension of SWNTs. The resulting powder was ground using a mortar and pestle for 30 minutes. The resulting fine powder was then added to the epoxy, hand stirred, and driven through the mixer. The output of the mixer was then cured as described above.

Control specimens of epoxy with SWNTs were prepared using the exact same procedure, except for use of the mixer for comparison purposes.

2.4.3 SWNT-Elastomer

The elastomer used for this study was a thermoplastic elastomer commercially referred to as DS-300 elastomer. This elastomer was found to dissolve partially and form a suspension in the same solvent used for epoxy (i.e. acetone + toluene). Required amount of SWNTs were added to this suspension, and the mixture was driven through the mixer. The resulting mixture was poured into a mold and was heated to $350^{o}C$, at which point the elastomer melted and the solvent started to vigorously boil (Boiling point of toluene = $110.62^{o}C$, B.P. of acetone = $56.29^{o}C$). After 30 minutes, all the solvent had evaporated. The mold was removed from the furnace and allowed to cool down to room temperature.

PVP stabilized SWNTs were also used to prepare composites. Elastomer + solvent was added to the PVP-stabilized SWNTs in water and heated on a hotplate with constant stirring. At this point, the water with PVP in it separated from the elastomer + solvent, while the PVP-wrapped SWNTs adhered to the elastomer molecules. The mixture was allowed to settle, and the water was wicked away using filter paper. The elastomer + SWNTs was then run through the mixer and cured as described above.

2.4.4   SWNT-Emulsion Polymers

A poly (vinyl acetate) homopolymer emulsion, having a commercial name Vinac XX210 was used for this study. This emulsion polymer was approximately 55% solids in water with average particle size of 105 nm. SWNTs were stabilized in Gum Arabic following the procedure outlined in [46]. The GA stabilized SWNTs were added to the emulsion polymer creating a master batch. This master batch had the highest concentration of SWNTs. Composites with lower SWNT concentrations were prepared by adding the required amount of emulsion polymer. For all samples, the aqueous composite mixture was kept at a constant 10 wt% solids by adding de-ionized water. Composites were prepared by driving the emulsion polymer + SWNTs + water through the mixer at $C_t =$ 0.65. Films of the composite were cast by pouring the output of the mixer into a shallow mold and drying in a current of air for 48 hours.

2.5   *Structural and Electrical Testing*

The epoxy and elastomer specimens were cast into a dogbone and tested in tension on an Instron 4400 Universal Testing Machine. To measure the electrical properties, the epoxy specimens were machined into cuboids 3 cm x 1 cm x 1 cm in dimension. The sides of the samples were polished. Two ends of the sample were coated with silver paste to ensure good electrical conductivity. A constant voltage of 15 V was applied across these two ends. The voltage drop across a known distance (2 cm) on the surface of the specimen was measured using a Fluke 25 Multimeter having a least count of 0.1 mV.

For each loading/C_t combination, the output of the mixer was poured into three molds, yielding three different samples. The electrical conductivity was taken to be the average of the three measured values. The electrical conductivity of the Vinac-SWNT composite films was measured using a Signatone 4-probe setup. The electrical conductivity of the epoxy composites was measured using the Signatone setup for comparison purposes, and both results were found to be within experimental error. To find the percolation threshold, composites with successively lower SWNT concentrations were prepared. The percolation threshold was taken to be the average of two quantities, namely the lowest SWNT loading that produced an electrically conductive composite, and the highest SWNT loading that produced an electrically insulating composite.

2.6   *EM Imaging*

Electron Microscopy was carried out at the Microscopy and Imaging Center at Texas A&M University. Transmission Electron Microscopy (TEM) was used for imaging the SWNTs stabilized with PVP. Scanning Electron Microscopy was used for all other samples. For TEM, a drop of PVP + SWNTs in water was placed on a Copper TEM grid and the water was gently wicked off using filter paper. While some of the SWNTs were absorbed by the filter paper, enough was left on the TEM grid to allow imaging. The epoxy composites were fractured on an impact tester. A thin slice of this specimen was then cut out, with the fracture surface pointing upwards and attached to a mount using Carbon tape. The sample was then sputter coated with 1 nm of Pt-Pd alloy to improve conductivity and reduce charging. These specimens were first imaged on a JEOL 6400

SEM. The limit of magnification provided by this microscope proved to be inadequate for the SWNT-epoxy composites. Consequently, all SEM imaging was then carried out on a LEO VP 1530 Field Emission SEM. The accelerating voltage used for all images was 1 kV, with a working distance in the range 3-8 mm.

The emulsion polymer composites were frozen in liquid nitrogen and then fractured by hand. The cross section of this specimen was then attached to a mount and imaged. The elastomer, being a thermoplastic, did not react well to the electron beam. The electron beam caused parts of the specimen to evaporate very rapidly, even at low accelerating voltages, and thus, we were unable to obtain any SEM images.

2.7   Image Analysis

2.7.1   Thresholding

All image analysis was carried out using MATLAB^{TM}. In SEM images, SWNTs appear brighter than the polymer by virtue of their high electrical conductivity. Thus, image analysis techniques were used to eliminate the polymer background. Thresholding is an intensity-based process of separating out portions of the image corresponding to objects that are of interest, from regions of the image that correspond to the background regions of an image, and is well suited for purposes of eliminating epoxy background from the SWNT-epoxy composite images. The pixel intensities of grayscale images ranges (typically) from 0 to 255. Thresholding involves finding a cut-off intensity. Pixels

having intensities above this cut-off value are assigned to the foreground, while pixels with intensities below the cut-off are assigned to the background. The result of any thresholding algorithm is an image composed of pixels having an intensity of 0 or 255, corresponding to background and foreground respectively.

Two thresholding algorithms were found to be useful in thresholding the SEM images: 1) iso-data thresholding [47] and 2) maximum entropy thresholding [48] (Refer to Appendix A). Figure 2.5 shows an SEM image of SWNTs in epoxy and the corresponding thresholded image from an iso-data thresholding algorithm. This was found to be inadequate in many cases where texture due to polymer fracture was prevalent. In such cases, thresholding was done using a maximum entropy method, or in some cases, manually. Figure 2.6 shows three images: (a) an SEM image of SWNTs in epoxy where fracture surface of the sample was textured; (b) the output of the iso-data thresholding algorithm when applied to the raw image and (c) the output of the maximum entropy thresholding algorithm when applied to the raw image. It is seen that the iso-data algorithm identifies regions that are clearly polymer fracture as SWNTs. These regions were greatly reduced using the maximum entropy thresholding method. Each of the thresholded images was divided into a number of bins, and the entropy was computed as described in section 1.4. The effect of varying the bin size (for method B) was also studied.
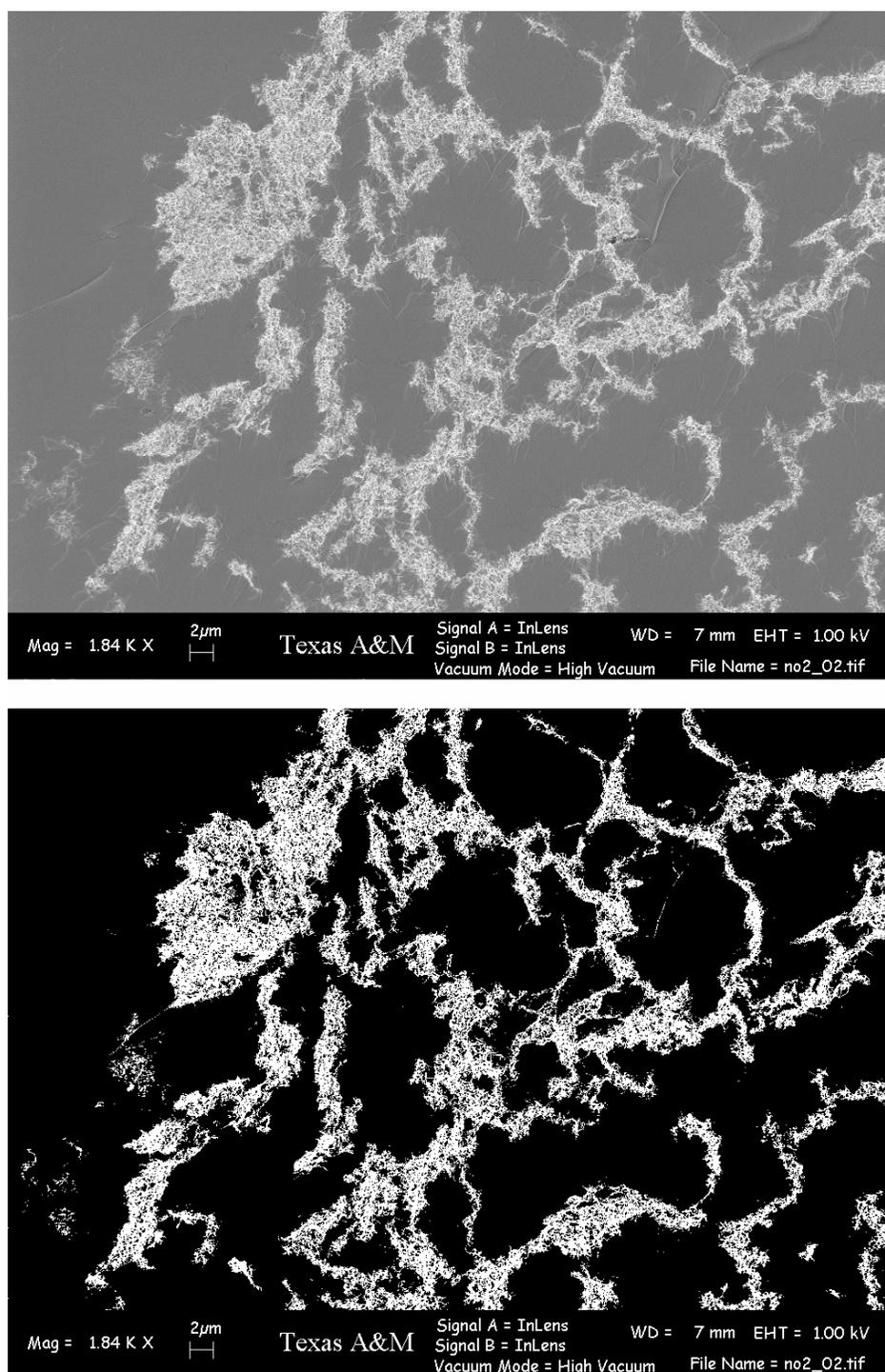
Figure 2.5   SEM image of SWNTs in epoxy and the corresponding thresholded
image (iso-data thresholding algorithm)
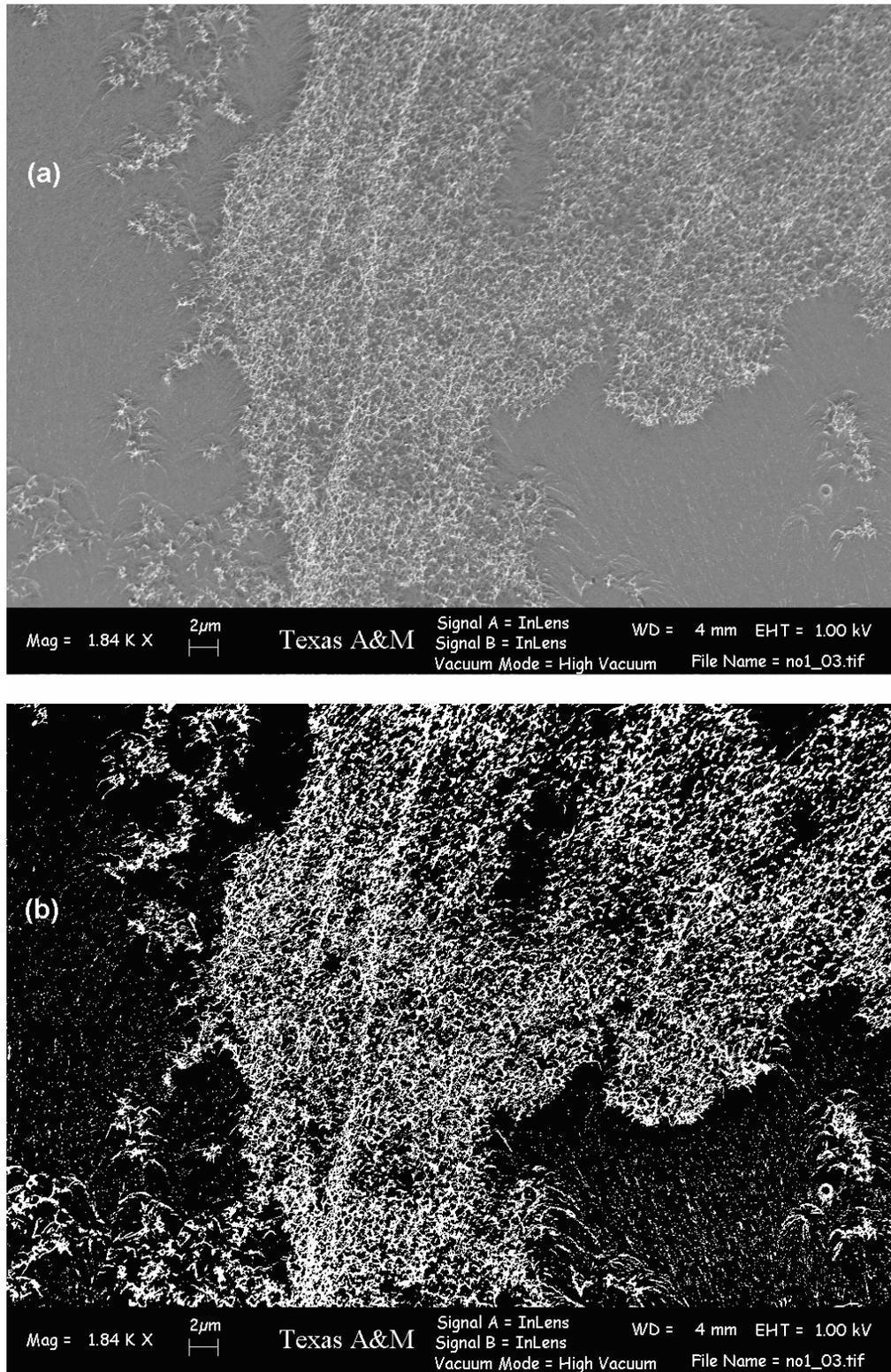
Figure 2.6   Raw image and output of thresholding algorithms
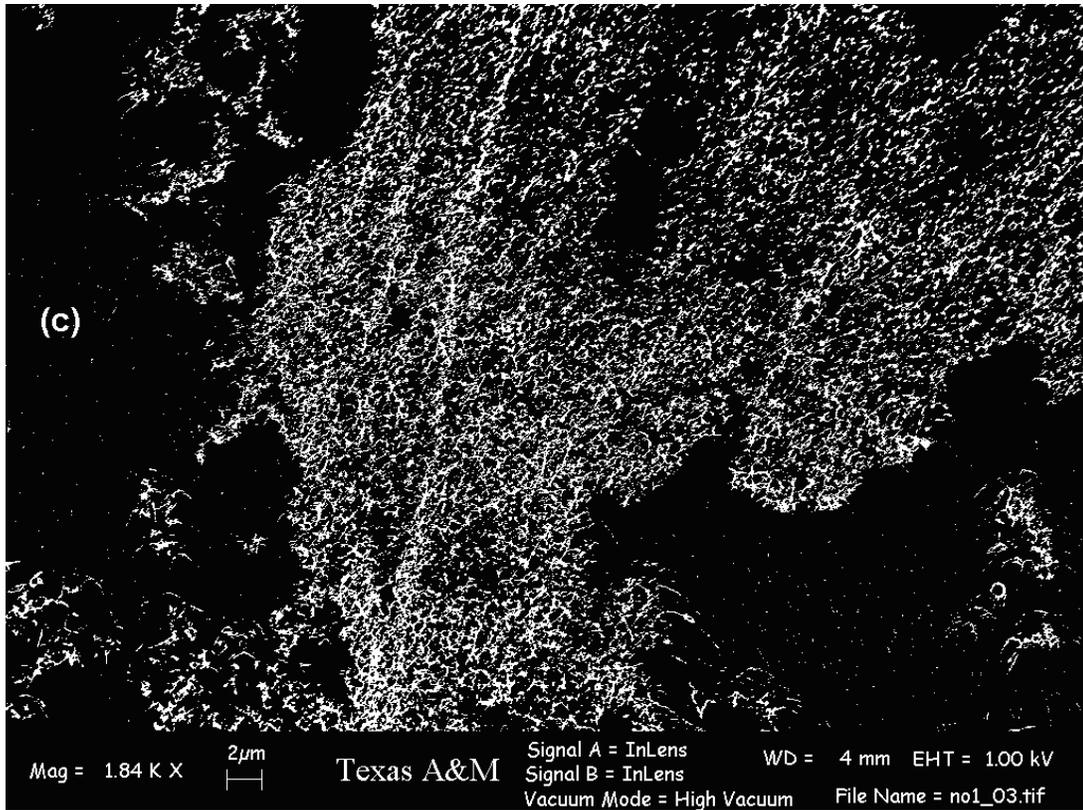
Figure 2.6   Continued

2.7.2   Image Analysis Validation

Figure 2.7 (a) is a thresholded SEM image of a sample that was prepared by hand-mixing the SWNTs into the epoxy, while Figure 2.7 (b) is that of a sample that was prepared using the mixer at $C_t = 0.65$. Both images were obtained under identical beam conditions and magnification. It is seen that the SWNT clusters are broken down into smaller clusters by the mixer. It is also worth mentioning that Figure 2.5 is an image of composites prepared by hand-mixing SWNTs into the epoxy, and Figure 2.6 (a) is that of a sample prepared at high C_t, where we expect poor mixing. Computer generated images were used to simulate this effect and thereby validate the image analysis algorithm. The procedure used to generate these images is briefly described. Random walks were used to simulate SWNT clusters. The average end-to-end distance of a random walk is proportional to the square root of the number of steps in the random walk [49]. Thus, longer random walks correspond to larger SWNT clusters, and thereby, images with longer random walks were taken to represent poorly mixed SWNT composites. On an initially blank image (all pixels = 0), a point was chosen at random. From this point, a random walk having a certain length was executed. Each step of the random walk was assigned a pixel intensity value of 255. This process was continued until the fraction of pixels having intensity values of 255 reached a pre-specified value. For each image, the length of the random walks was fixed. Each random walk was taken to represent a cluster of SWNTs. Figure 2.8 shows two random walk images that illustrates the effect of walk length on cluster size. Black pixels (intensity = 0) represent the polymer background, while white pixels (intensity = 255) represent SWNTs.
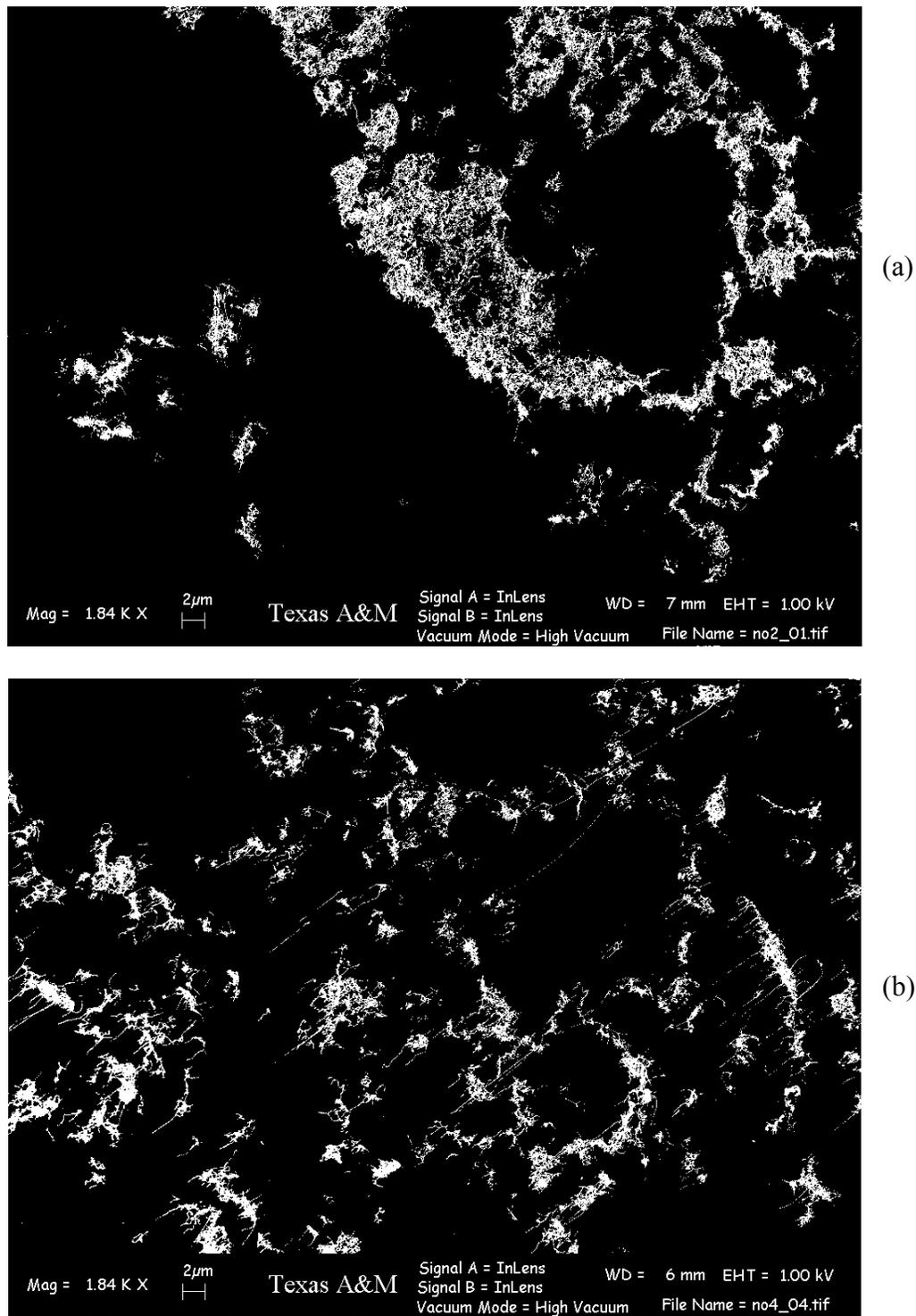
Figure 2.7   Thresholded SEM images (a) hand mixed (b) $C_t = 0.65$
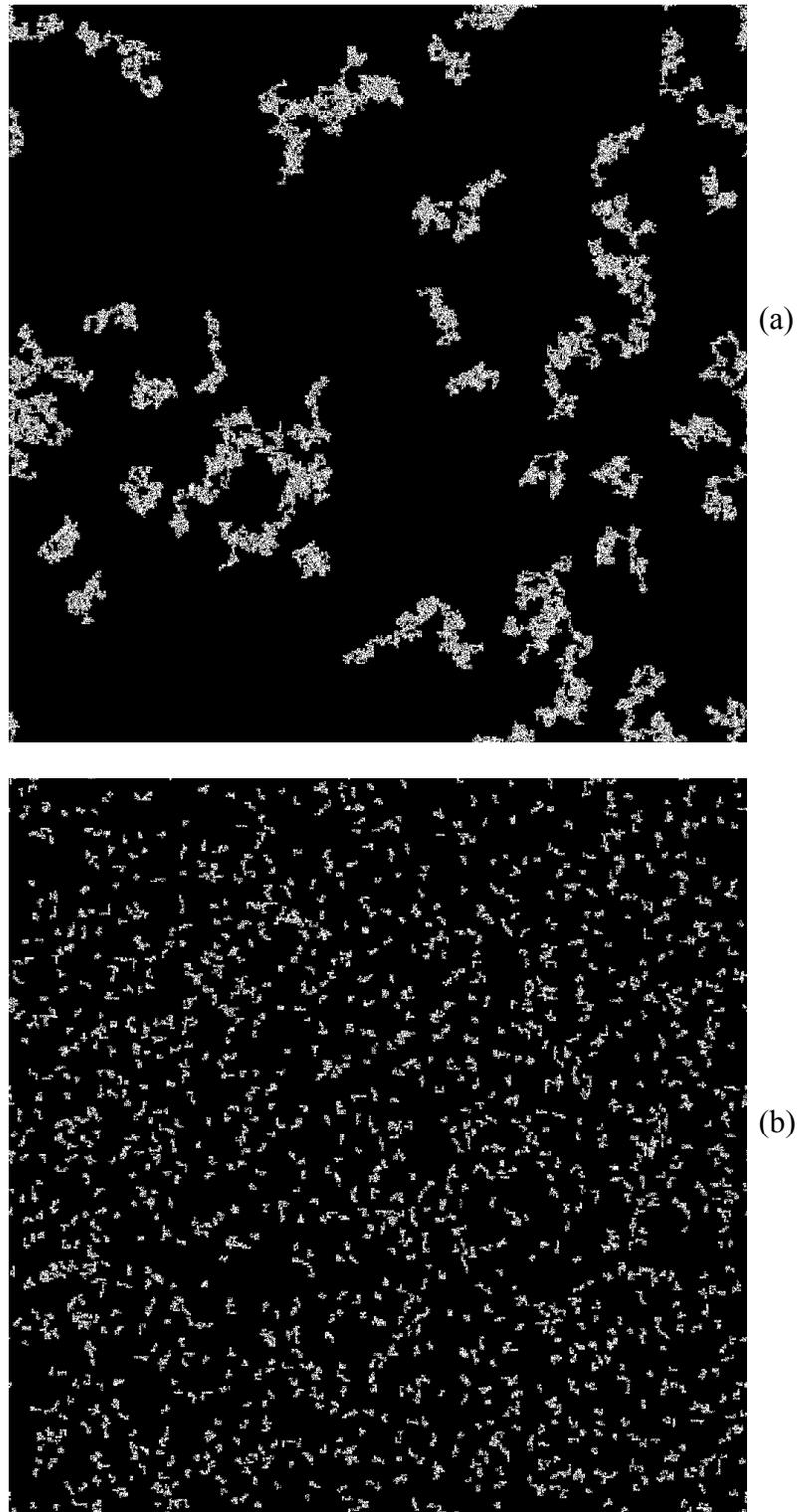
Figure 2.8   Computer generated images. (a) 500 steps (b) 10 steps

For validation purposes, the fraction of pixels that had an intensity value of 255 was kept constant for all images (5 %), as was the size (1000 pixels x 1000 pixels). Figure 2.9 shows a plot of the normalized entropy vs. random walk length computed for the random walk images, for six different bin sizes. Each point is the normalized image entropy computed over a set of six different 1000 x 1000 random walk images. This plot shows that image entropy decreases as the random walk length increases. In other words, as the occupied pixels in an image become more clustered, the entropy decreases. As the occupied pixels become more dispersed and random, the entropy increases. The effect of bin size variation is also seen. The importance of bin size has been studied previously [50,51] and has been shown to define the scale of observation of the system. For a bin size of 10 x 10 pixels, appreciable variation in the entropy is seen only for small random walk sizes. As the bin size increases, the range over which the entropy varies appreciably increases. For the largest bin size of 1000 x 1000 pixels, all random walk images yield a normalized entropy value of 1, as all bins contain equal number of occupied pixels.

Figure 2.10 plots the effect of bin size variation on three different kinds of computer generated images, having the smallest, largest and intermediate random walk lengths. For the smallest random walk length (smallest clusters), it is observed that the normalized entropy reaches a value close to 1 at a bin size of about 100 x 100 pixels, indicating that all bins contain roughly equal number of occupied pixels, and the images are homogeneous at this scale of observation.
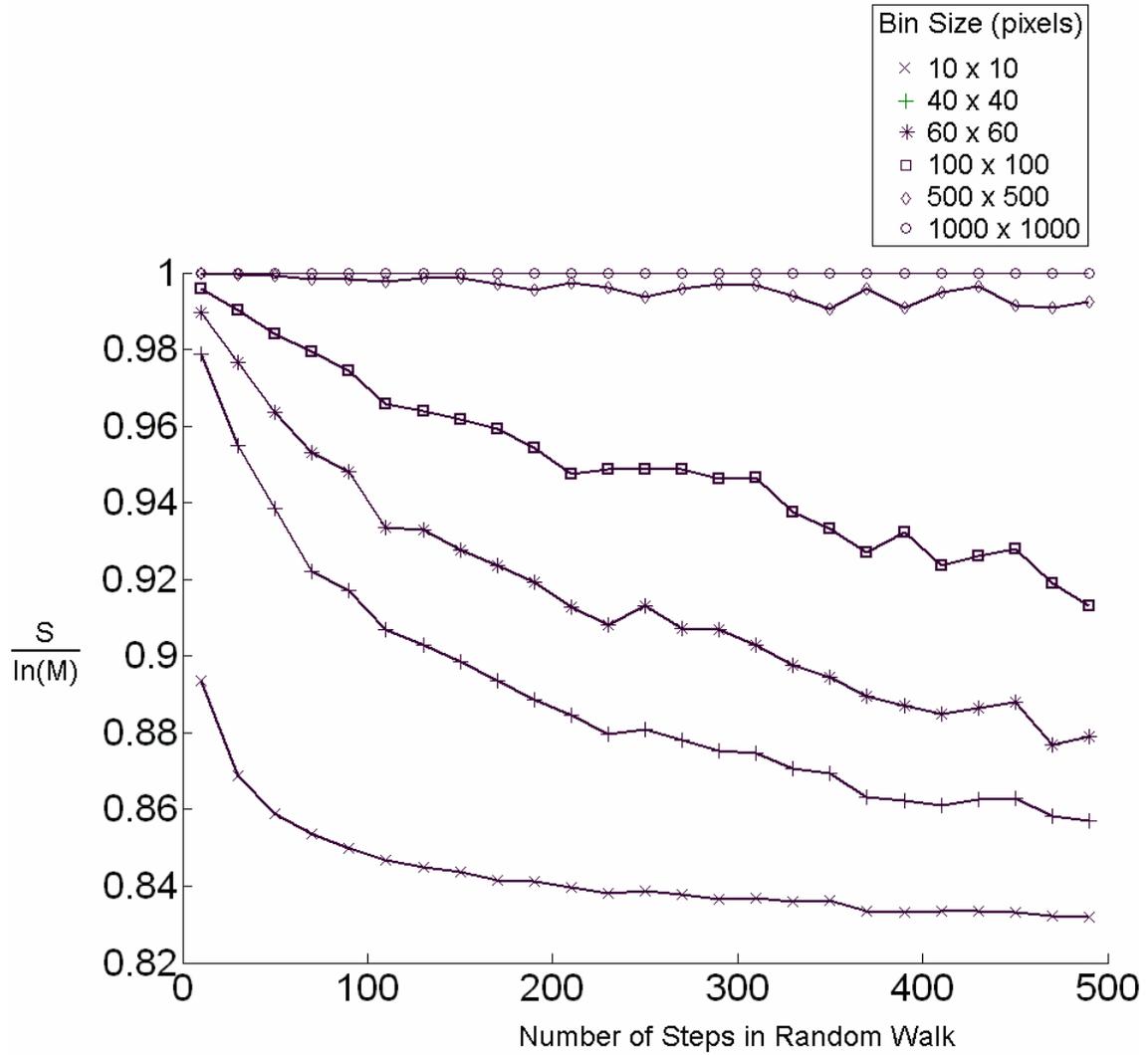
Figure 2.9   Normalized entropy of random walk images
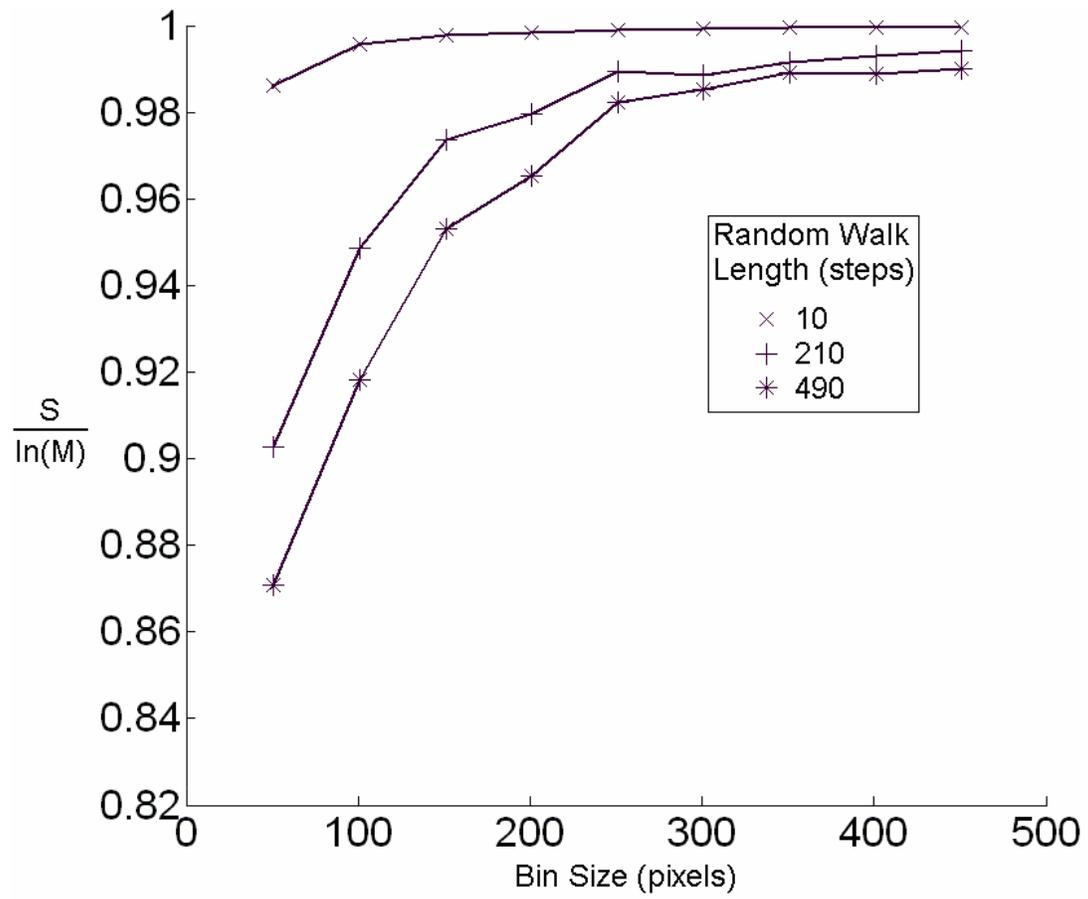
Figure 2.10   Effect of variation of bin size

On the other hand, for images having large clusters, the normalized entropy is less than 1 even at a bin size of 450 x 450 pixels, indicating that the spatial distribution of occupied pixels is inhomogeneous at this scale. It is also worth noting that for a fixed bin size, images with larger clusters (longer random walks) have lower entropy than those with smaller clusters (shorter random walks). Thus, for two sets of images, if the number of occupied pixels is the same, the relative degree of dispersion may be determined by using the same bin size for both. Therefore, this entropic analysis of dispersion using images may be used to quantify dispersion of SWNTs in epoxy composites. This analysis was carried out on SEM images after making sure that the total number of occupied pixels obtained from each set of thresholded SEM images was comparable.

3. EXPERIMENTAL RESULTS*

3.1   Introduction

Stabilization of SWNTs using Poly Vinyl Pyrrolidone (PVP) was studied by Transmission Electron Microscopy. SWNTs were mixed with epoxy by running the mixer at four different values of C_t. Re_j for all these experiments was kept constant. The weight fraction of SWNTs in the epoxy was also varied to study the dependence of electrical resistivity on loading and the results were interpreted using percolation theory. The curing process for the epoxy, as outlined in previous sections, takes a total of 10-12 hours to complete. During this time, although it was not visually obvious, the SWNTs might have settled. The electrically conductive property of SWNTs lends itself to an investigation of settling by using electrical conductivity measurements. These results were interpreted using the sedimentation equations for colloidal particles. The electrical properties of the SWNT-emulsion polymer were also measured, while elastomer-SWNT composites were tested in tension. The epoxy-SWNT composites were imaged on an SEM as described previously. The dispersion was quantified using the entropic measure of mixing, and assigned an index of dispersion ranging from 0 to 1. The effect of bin size (or scale of observation) was also studied.

3.2   *Stabilizing SWNTs with PVP*

Figure 3.1 shows two TEM images of SWNTs, at the same magnification. In Figure 3.1 (a), the SWNTs were imaged as-received, whereas Figure 3.1 (b) is a TEM image of SWNTs stabilized using a 2 wt% PVP solution. At this magnification, it is apparent that stabilizing the SWNTs with PVP leads to a smaller cluster size, which implies a stronger interaction between the SWNTs and PVP. The resulting PVP-SWNT suspension was electrically insulating. This further lends weight to the conjecture that the PVP molecules wrap themselves around the SWNTs and serve to separate out SWNTs within a cluster. The particles seen in the images are impurities (a combination of Fe catalyst and carbonaceous impurities) that results from the production process. Other naturally occurring polymers, like Gum Arabic and starch are also helpful in obtaining a similar effect. In this type of SWNT stabilization, the wrapping polymer bonds to the SWNTs by means of dispersion forces, thereby not disrupting the chemical structure of the SWNTs, and thereby preserving their strength. However, the load transfer characteristics of such a system are lower when compared with when the SWNTs are functionalized. It still remains an open question as to which of the two methods is superior.

(a)

63,000X magnification

Scale: ————————200 nm

(b)
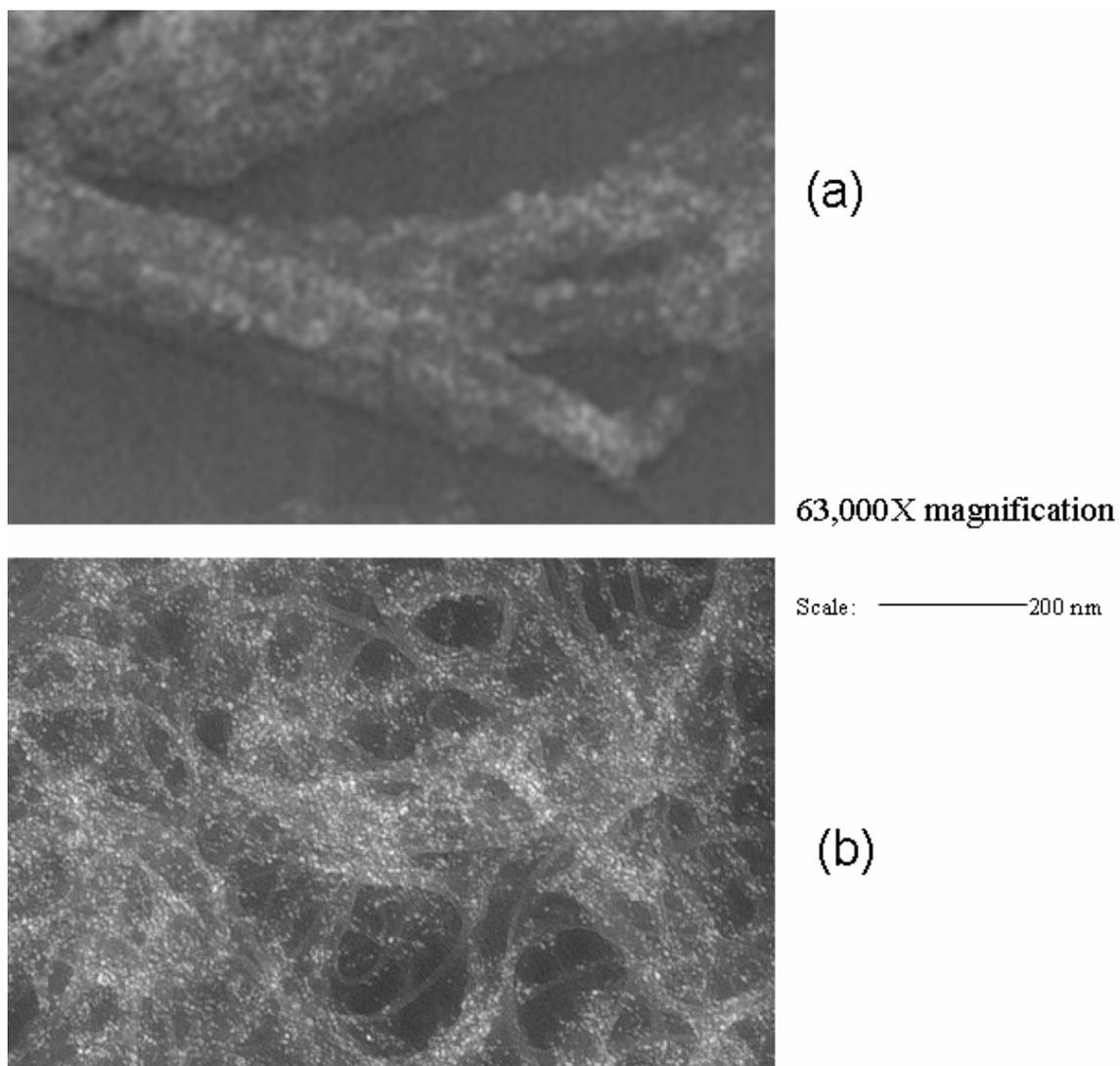
Figure 3.1   TEM images of SWNTs (a) as received (b) stabilized with PVP

3.3   *Structural and Electrical Properties*

3.3.1   SWNT-Epoxy Composites

Figure 3.2 shows the tensile strength of samples as measured by an Instron 4411 Universal Testing Machine. Compared with properties of plain epoxy, there is little change in modulus and ultimate tensile strength of 0.2 wt% SWNT composites without PVP. An increased loading of SWNTs was found to enhance both the modulus and ultimate tensile strength. The results are summarized in Table 3.1. When compared with plain epoxy, 0.2 wt% loading samples without PVP show a decrease in modulus and a slight increase in ultimate tensile strength (<1%). In contrast, 0.2 wt% samples with PVP show an increase in both ultimate strength and modulus of 5 and 27%, respectively. 0.5 wt% samples without PVP show an increase in strength and modulus of 4 and 38%, respectively, when compared with the plain epoxy. The corresponding sample with PVP at the same loading shows an increase in ultimate strength and modulus of 5 and 40%, respectively. It is believed that poor enhancement for composites prepared without PVP results from poor bonding of SWNTs with the epoxy matrix, which results in poor load transfer between the matrix and SWNTs. This hypothesis is supported by the observation that during the acquisition of SEM images, at high magnifications (starting at about 20,000 X), a number of SWNTs present on the fracture surface were seen to respond to the electron beam and exhibit a swaying movement. This is an indication that SWNTs have been 'pulled out' from the epoxy matrix during fracture.
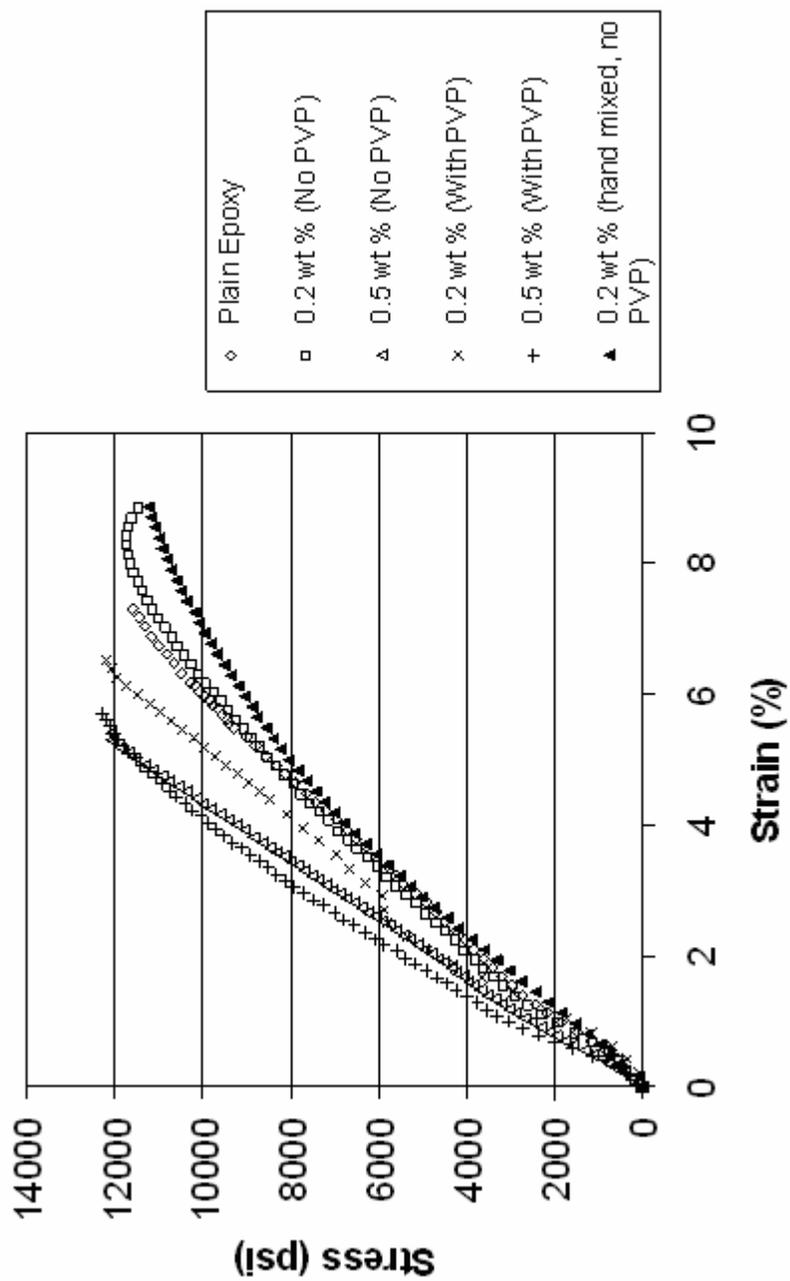
Figure 3.2   Stress *vs.* strain of various epoxy composites

Table 3.1   Tensile strength of epoxy composites

Composite Formulation	Young's Modulus (psi)	Ultimate Tensile Strength (psi)
Plain Epoxy	161280	11620
0.2 wt% without PVP, Hand-Mixed	160725	11229
0.2 wt% without PVP	156840	11712
0.2 wt% with PVP	205630	12200
0.5 wt% without PVP	222810	12100
0.5 wt% with PVP	225470	12280

These results indicate that wrapping of SWNTs with PVP serves two purposes: the first is that PVP separates out individual SWNTs within a cluster, thereby improving their dispersion; the second is that PVP provides a system for efficient load transfer between the epoxy matrix and SWNTs. The use of PVP for dispersion and load transfer has been hinted at by Grunlan and Bannon [41]. PVP wrapped SWNTs have been reported to be robust enough to withstand washing with water for 40 min, and they may be treated as a single unit [52]. The surface energy of epoxy and PVP are, respectively, 35.1 and 49.36 mJ m^{-2} [53,54]. We were unable to find a surface energy measurement for SWNTs, but the surface energies for graphite and MWCNTs were reported to be 120 and 450 mJ m^{-2} [55], and we expect the surface energy of SWNTs to be comparable with these values. Thus comparing the disparity in surface energies, we see that PVP would be expected to improve the load transfer efficiency between the epoxy matrix and SWNTs.

Percolation theory has been used to describe the electrical behaviour of polymers with conducting fillers. Figure 3.3 is a plot of electrical conductivity vs. weight percent loading plotted on a log-log scale. The following formula from percolation theory [46] is used to fit a line to the experimental data:

$$\sigma = \sigma_0 (W - W_C)^S$$
(3.1)

where σ is composite conductivity in S m^{-1}, σ_0 is a scaling factor related to the intrinsic conductivity of the filler material, S is a power law exponent (typically 1.6 - 2 for random systems [56]), W is the weight fraction of filler material, and W_C is the weight concentration of filler material at the percolation threshold.
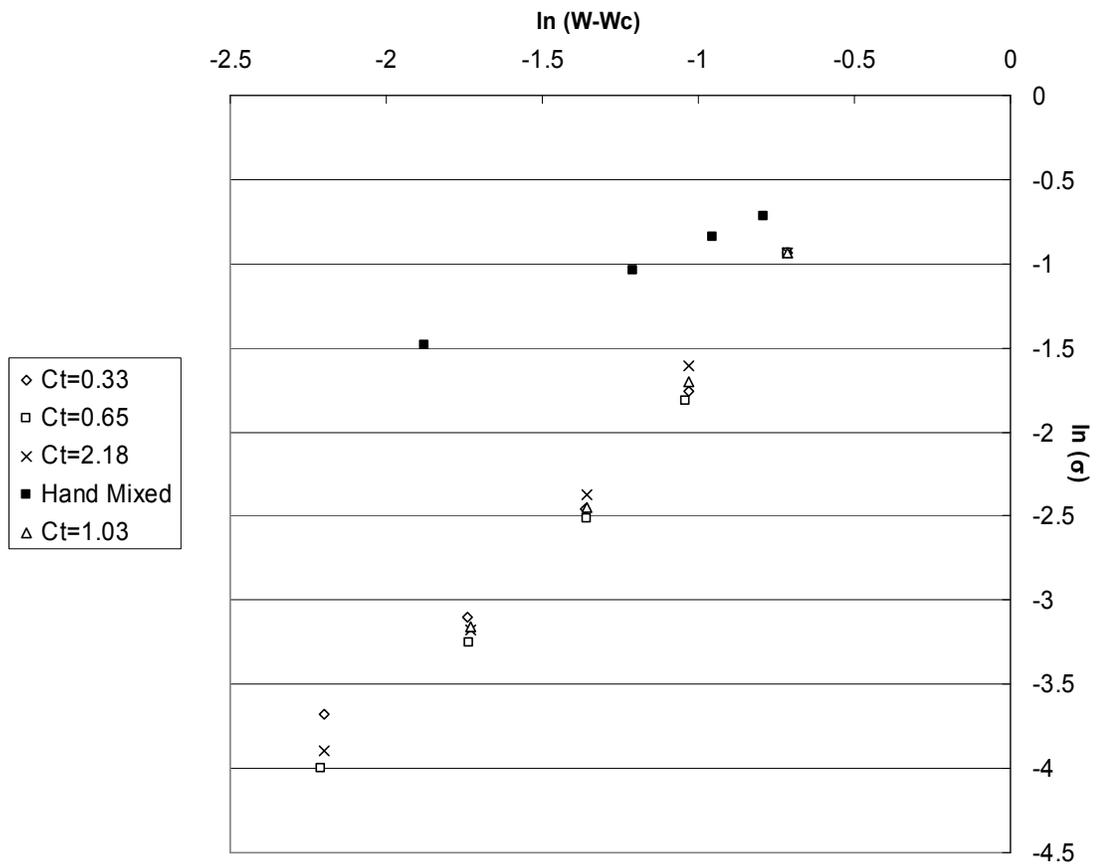
Figure 3.3   Percolation curves for various SWNT-epoxy composites

The hand-mixed composite samples had a percolation threshold of 0.0382 wt % of SWNTs, while composites prepared by impingement mixing had a percolation threshold of 0.0063 wt % of SWNTs. The experimental data for the hand mixed and impingement mixed samples exhibit classical percolation type behavior of Equation (3.1). Table 3.2 summarizes the exponent obtained by fitting a line to the points in Figure 3.3 with the R^2 values. Breaking of larger clusters into smaller ones results in a reduction in the average particle size. It has been shown previously [57] that the percolation threshold decreases with particle size. Thus, we interpret lowering of the percolation threshold as an improvement in the dispersion of SWNTs and that composites prepared by impingement mixing have smaller SWNT clusters, and that their distribution within the epoxy matrix is more random. DC electrical conductivity data obtained in this study is comparable with data obtained by [58]. The effect of dispersion on the electrical conductivity was more prominent at lower volume fractions. At higher volume fractions, the electrical conductivity of the composites was not seen to change appreciably with mixing. The variation in electrical resistivity as a function of C_t is plotted in Figure 3.4 (a), and its change with mixing can clearly be observed on a linear scale. Figure 3.4 (b) shows the same plot, but rescaled to show the effect of mixing on the higher SWNT loading samples. It is observed that for a C_t of 0.65 produces composites with the highest electrical resistivity. This type of behaviour, where as the electrical resistivity first increases, reaches a peak and then decreases, with mixing has been observed previously with high-structure carbon black-polymer composites. [59,60]. The plot also shows the electrical resistivity of hand-mixed samples, which are indicated by $C_t=0$.

Table 3.2   Fitting parameters for various SWNT-epoxy composites

| Sample Type	Exponent S	R^2
Hand Mixed	0.7072	0.9982
C_t=0.33	1.833	0.9797
C_t=0.65	2.0329	0.989
C_t=1.03	2.1895	0.9971
C_t=2.18	2.026	0.9934
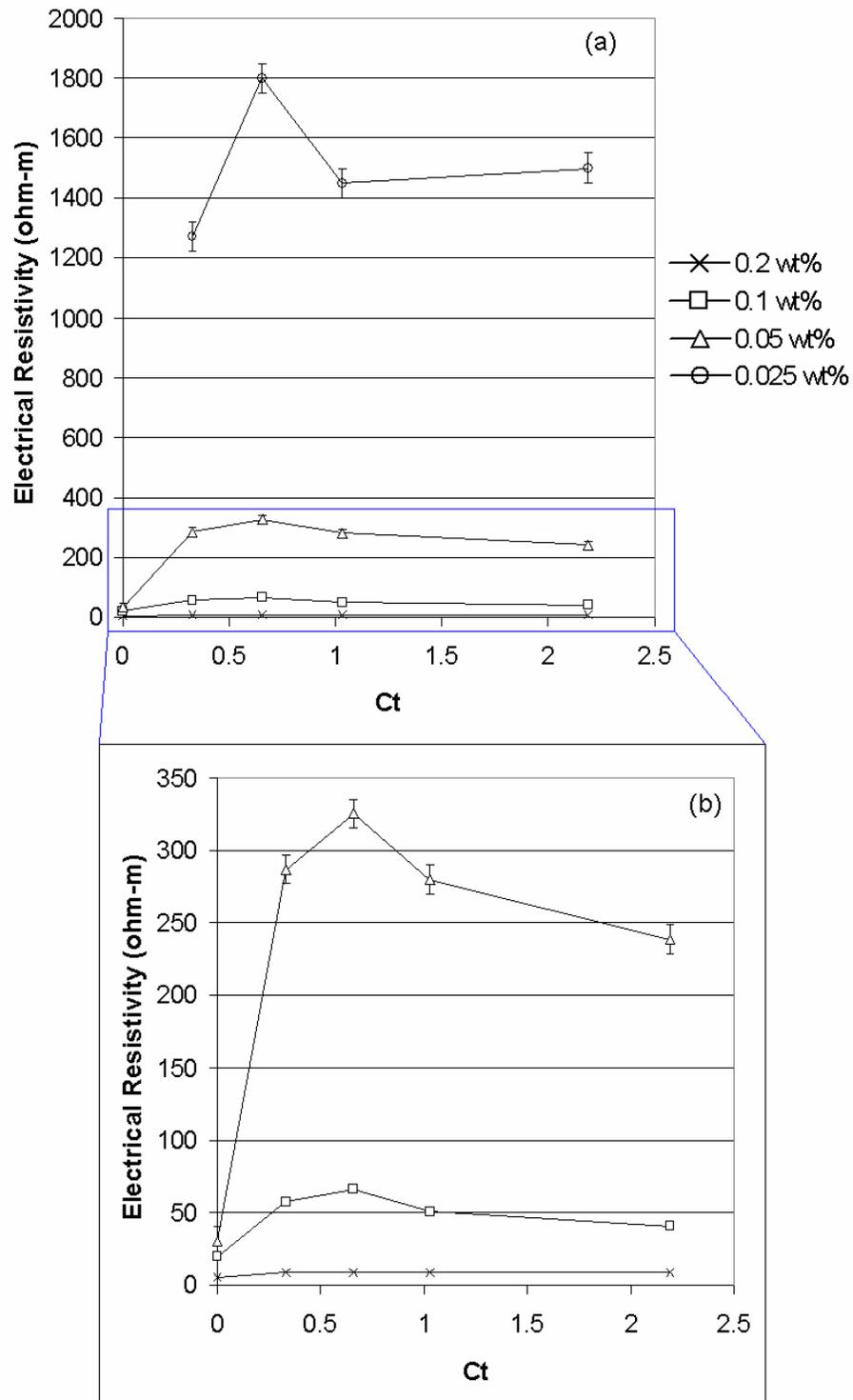
Figure 3.4   Electrical resistivity as a function of C_t

3.3.2 Sedimentation of SWNTs in Epoxy

The settling of SWNTs was studied by measuring the electrical conductivity of the composites. In this study, each composite sample was cut into three equal sections: top, middle and bottom. The electrical resistivity of each of these sections was measured for all specimens. It was consistently observed that the top 1/3 of all specimens had the highest resistivity, while the bottom 1/3 had the lowest resistivity, and the middle 1/3 had resistivity values in between the two. This means that relatively speaking, the top portions of the composites have a lower concentration of SWNTs than the bottom portions. It was also observed that the resistivity of each of the parts of the specimen is lower than that of the whole specimen. The electrical resistivity measurements were then used to approximate the fraction of SWNTs in different portions of the specimen. As an illustrative example, Figure 3.5 (a) is a plot of the electrical resistivity vs. weight percentage loading of SWNTs for a composite prepared at $C_t = 0.33$. Near an SWNT loading of 0.1 wt%, the resistivity curve is fairly linear. Figure 3.5 (b) shows a portion of (a), enlarged. The three horizontal lines correspond to the measured average electrical resistivities of the top, middle and bottom thirds of specimens having 0.1 wt% loading. The differences in resistivity indicate an SWNT concentration difference of 0.0039 wt% between the top and middle, and 0.0056 wt% between the middle and the bottom, yielding a maximum variation in SWNT concentration of 5.6%. Figure 3.6 shows how the electrical resistivity of each of the portions of the specimens varies with C_t and SWNT loading, superimposed upon Figure 3.4.
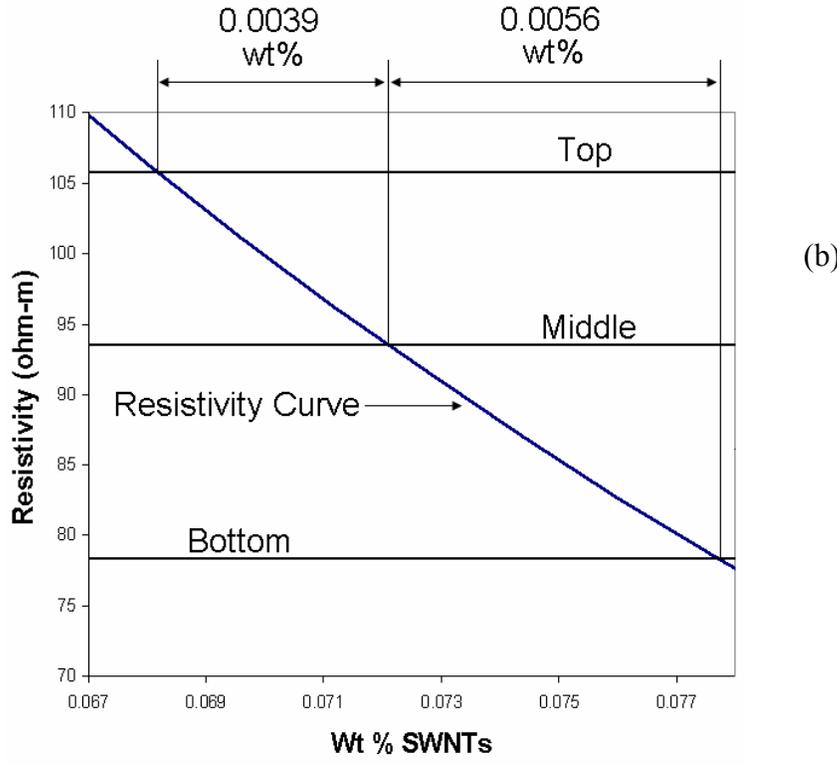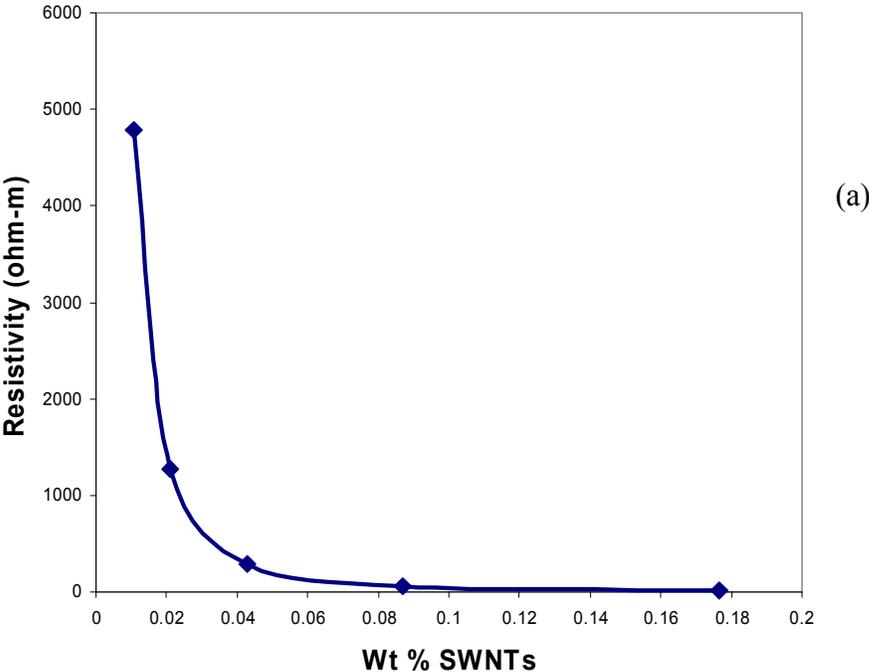
Figure 3.5   Estimation of SWNT fraction in different sections of specimens
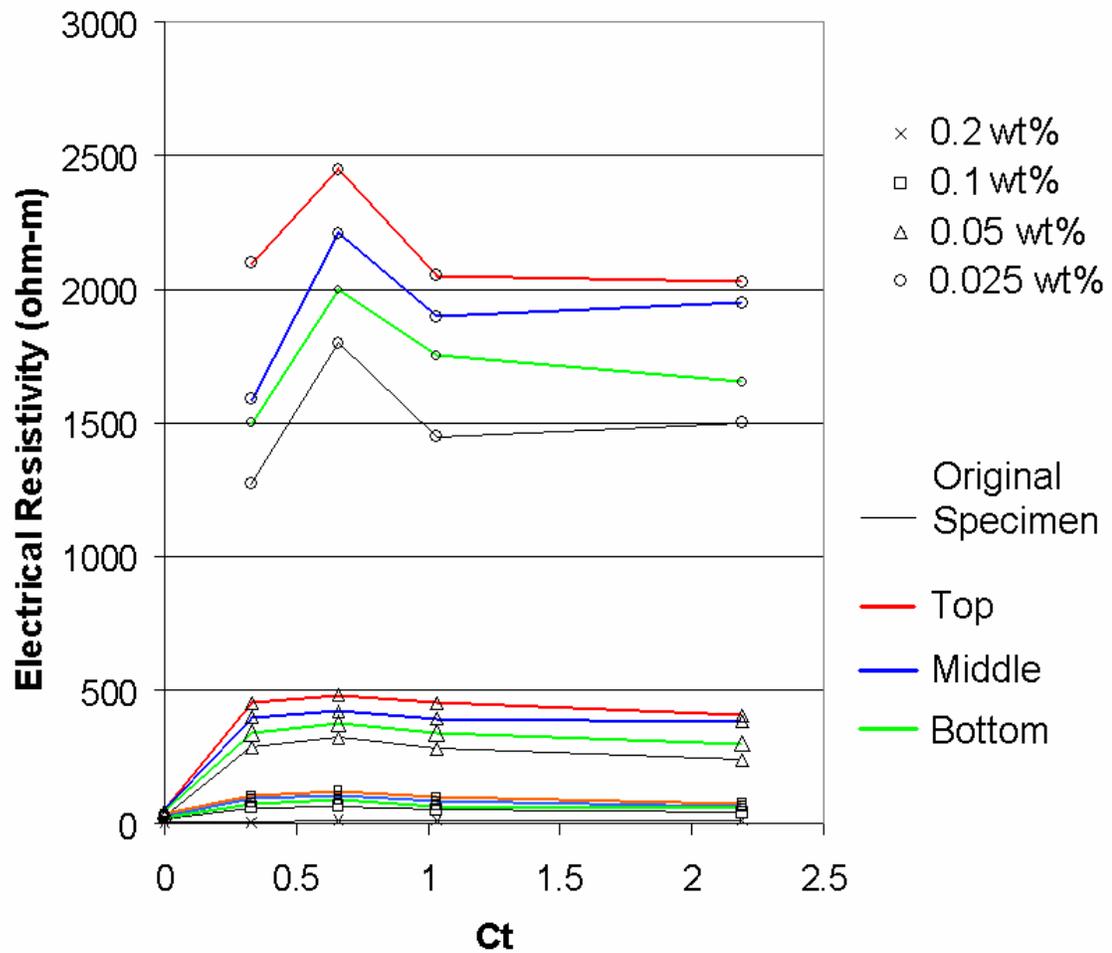
Figure 3.6   Electrical resistivity of portions of composite as a function of C_t

Since the loading of SWNTs is quite small, the sedimentation equilibrium equation for colloidal particles may be used to describe the settling process. The equilibrium configuration of colloidal particles can be determined by balancing the diffusion force with the gravitational force, and the equilibrium concentration as a function of height is given by [61]

$$c(h) = c_o \exp\left(\frac{-mgh}{k_B T}\right) \tag{3.2}$$

where
c = volume fraction at a height h

c_o = volume fraction at h=0

m = reduced mass of individual colloidal particle, $\Delta\rho$ x volume

k_B = Boltzmann constant

T = temperature

The density of epoxy + curing agent specified by the manufacturer was 1157.343 kg m^{-3}, while the density of SWNTs has been reported to be between 1330 and 1400 kg m^{-3}, [62] and therefore taken to be 1365 kg m^{-3}. This yields $\Delta\rho$ of 207.657 kg m^{-3}. The volume of SWNTs was estimated by considering the SWNTs as cylinders having a diameter of 2 nm, and length of 1000 nm. In the case of SWNT-epoxy composites, the overall volume fraction of SWNTs in the specimens is known. This can then be used to estimate (Refer to Appendix B for derivation) the volume fraction of SWNTs in the bottom, middle and top thirds of the container as

$$\phi_B = \frac{3}{L} \int_0^{L/3} c(h)dh \tag{3.3a}$$

$$\phi_M = \frac{3}{L} \int_{L/3}^{2L/3} c(h)dh \tag{3.3b}$$

$$\phi_T = \frac{3}{L} \int_{2L/3}^{L} c(h)dh \tag{3.3c}$$

with

$$c_o = \frac{\phi Lmg}{k_B T}\left[1 - \exp\left(\frac{-mgL}{k_B T}\right)\right]^{-1} \tag{3.4}$$

where   L   = total height of container

                Φ = volume fraction of SWNTs in specimen

                Φ_B = volume fraction of SWNTs in bottom 1/3 of specimen

                Φ_M = volume fraction of SWNTs in middle 1/3 of specimen

                Φ_T = volume fraction of SWNTs in top 1/3 of specimen

It is worthwhile noting that in the above equations, volume fraction may be replaced by volume percent, weight percent or number density throughout. Figure 3.7 plots the theoretical concentration of SWNTs as a function of height for a total concentration of 0.1 wt% SWNTs, across a height of 1.5 cm (the height of the specimens prepared in experiments).
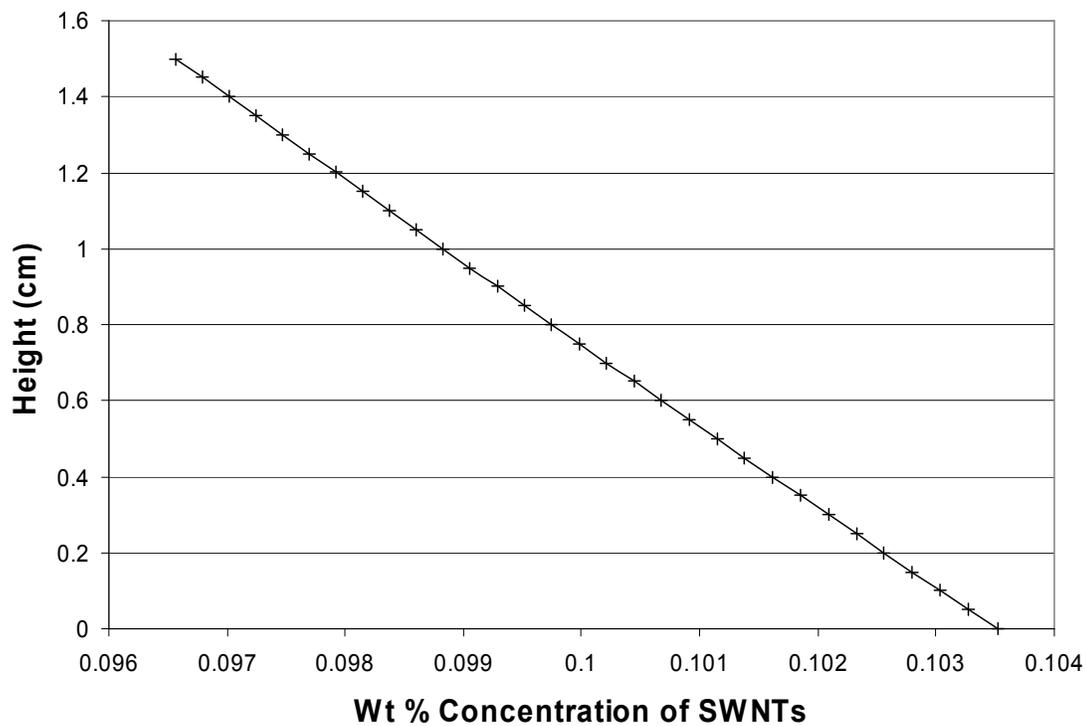
Figure 3.7   Theoretical concentration of SWNTs as a function of specimen height

For the parameters and height range used, a linear profile was obtained. Integrating the profile, we obtain the weight percent concentration in the bottom, middle and top thirds of the specimen to be 0.1023, 0.09998 and 0.09769 wt % respectively. These results show that the concentration varies by about 0.002 wt% of SWNTs between the top, middle and bottom thirds of the specimen, which yields a 2% variation in SWNT concentration.

Two minor points of error are noted between the experimental approximation and theoretical description. Firstly, the fraction of SWNTs in different portions of the specimen as estimated by experiments is lower than the theoretical description. Secondly, the theoretical difference between SWNT concentrations in different portions of the sample is half the difference estimated by electrical resistivity measurements. Three factors are thought to contribute to these discrepancies: 1) It has been tacitly assumed that the electrical resistivity is independent of composite dimensions. The increase in resistivity that is observed when a composite sample is cut into smaller pieces shows that this is not the case. The high aspect ratio of SWNTs makes them form a highly tangled network in the epoxy matrix, and that cutting the specimens results in destruction of conductive pathways that would originally have conducted current from the top of the specimen to the bottom. 2) The SWNTs have an undetermined amount of Fe catalyst impurity present that contribute to increase the measured loading of the SWNTs, but not necessarily to increase the electrical conductivity. 3) The dimensions of the SWNTs were taken to be constant, while in reality the SWNTs are not of equal

length. However, even with these minor discrepancies between the experimental estimation and the theoretical estimation, it may be concluded that the SWNTs do settle over the 12 hour period it takes to cure the epoxy, but this sedimentation is minimal.

These measurements were also used to estimate the average floc size of SWNTs by using the sedimentation equilibrium equation (3.2). Treating these flocs as hard spheres, an average diameter of 3.5×10^{-8}m was obtained. The SEM images, however, indicate much larger floc diameters (on the order of 10^{-6} m). This is expected, as the SWNTs do not close-pack, but form flocs with free volume in between the individual SWNTs, as is evident from the SEM images. This formation of flocs serves to increase the drag force on a floc of SWNTs. The net effect of increased drag on a SWNT floc may be accounted for by using a smaller value for SWNT density, referred to as the effective density. This is a standard method of analyzing the sedimentation of flocs, and Tambo and Watanabe [63] have shown that the log of floc effective density decreases lineary as the log of the floc diameter increases. Thus, to calculate the reduced mass in equation (3.2), assuming the effective density of an SWNT floc to be 1157.307 kg m^{-3}, which is 0.847844 times the original SWNT density, an average floc size of 1×10^{-6} m was obtained, which yields floc diameters on the order of magnitude as those observed in the SEM images.

3.3.3   SWNT-Elastomer

Figure 3.8 shows a result of tensile testing of specimens of the elastomer with different SWNT loadings. It is observed that the plain elastomer stretches to almost 40 times its

original length. Upon addition of 0.5 wt% SWNTs, the maximum strain that the elastomer undergoes before fracture is observed to reduce by a factor of almost 2, while the ultimate stress is not seen to increase greatly. With an addition of 2 wt% SWNTs, however, the maximum stress was seen to increase to almost 500%, with a corresponding reduction in the maximum strain the elastomer undergoes. This means that addition of SWNTs serves to stiffen the elastomer. The observed Youngs moduli for the different SWNT loadings are 4123.9, 8961.6 and 268,265 N/m^2 for 0, 0.5 and 2 wt% loading of SWNTs.

A dramatic increase in the modulus is seen at higher SWNT loadings. However, this reinforcement comes at a price. The ultimate strain of the composites is far lesser than that of the pure elastomer. This behaviour has been observed previously by other researchers using other elastomers as well [64]. The effect of adding PVP stabilized SWNTs to the elastomer is also seen in the figure. The effect is similar to the effect seen in the case of SWNT-epoxy composites. PVP serves as a load transfer mechanism between the SWNTs and elastomer. Thus, the load applied to the bulk of the specimen is transferred more efficiently to the SWNTs, resulting in a stronger composite.
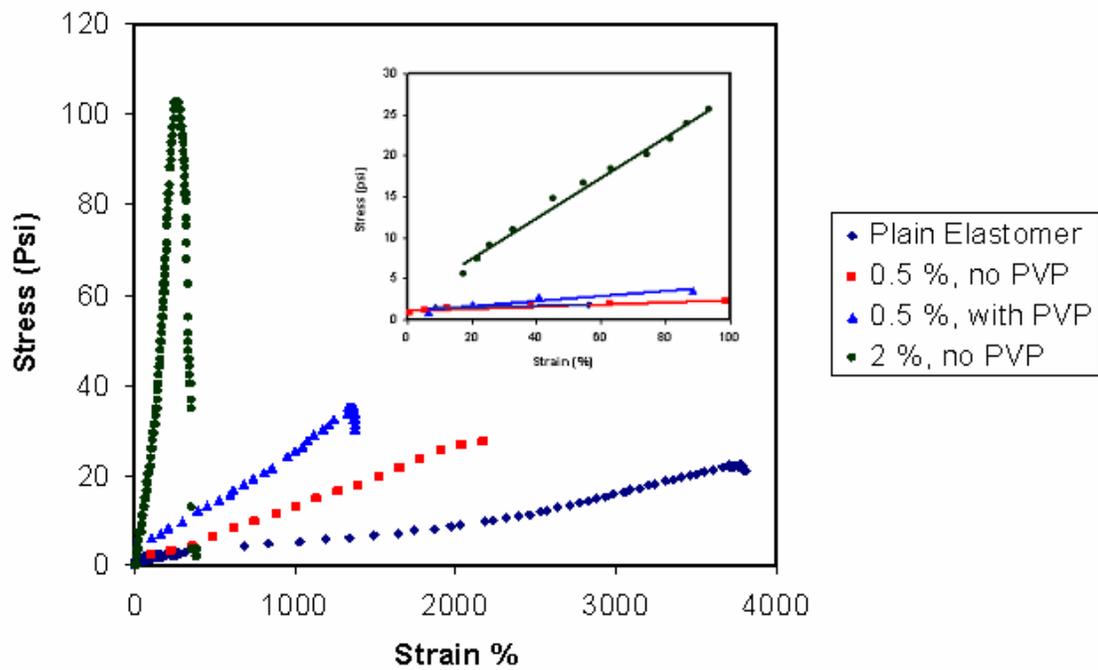
Figure 3.8   Tensile testing of DS-300 elastomer

3.3.4 SWNT-Emulsion Polymers

Figure 3.9 shows the percolation curve obtained for thin films of Vinac XX210 emulsion polymer with SWNTs. The percolation threshold for this system was 0.03 wt% SWNTs. The stabilization of SWNTs with Gum Arabic raises the percolation threshold, as the stabilizing polymer wraps itself around the SWNTs, reducing their effective electrical conductivity. This threshold, however, is far lower than the percolation threshold of systems with conventional fillers. Other factors that contribute to the low percolation threshold are the unique microstructure of the polymer emulsion and the large aspect ratio of SWNTs. Polymer emulsions are known to be fundamentally different from polymer melts. During solidification of a melt based system, the filler particles (SWNTs) are free to aggregate throughout the polymer matrix resulting in an increased percolation threshold. This is not the case in emulsion polymers, where the polymer exists as solid particles suspended in water prior to film formation.
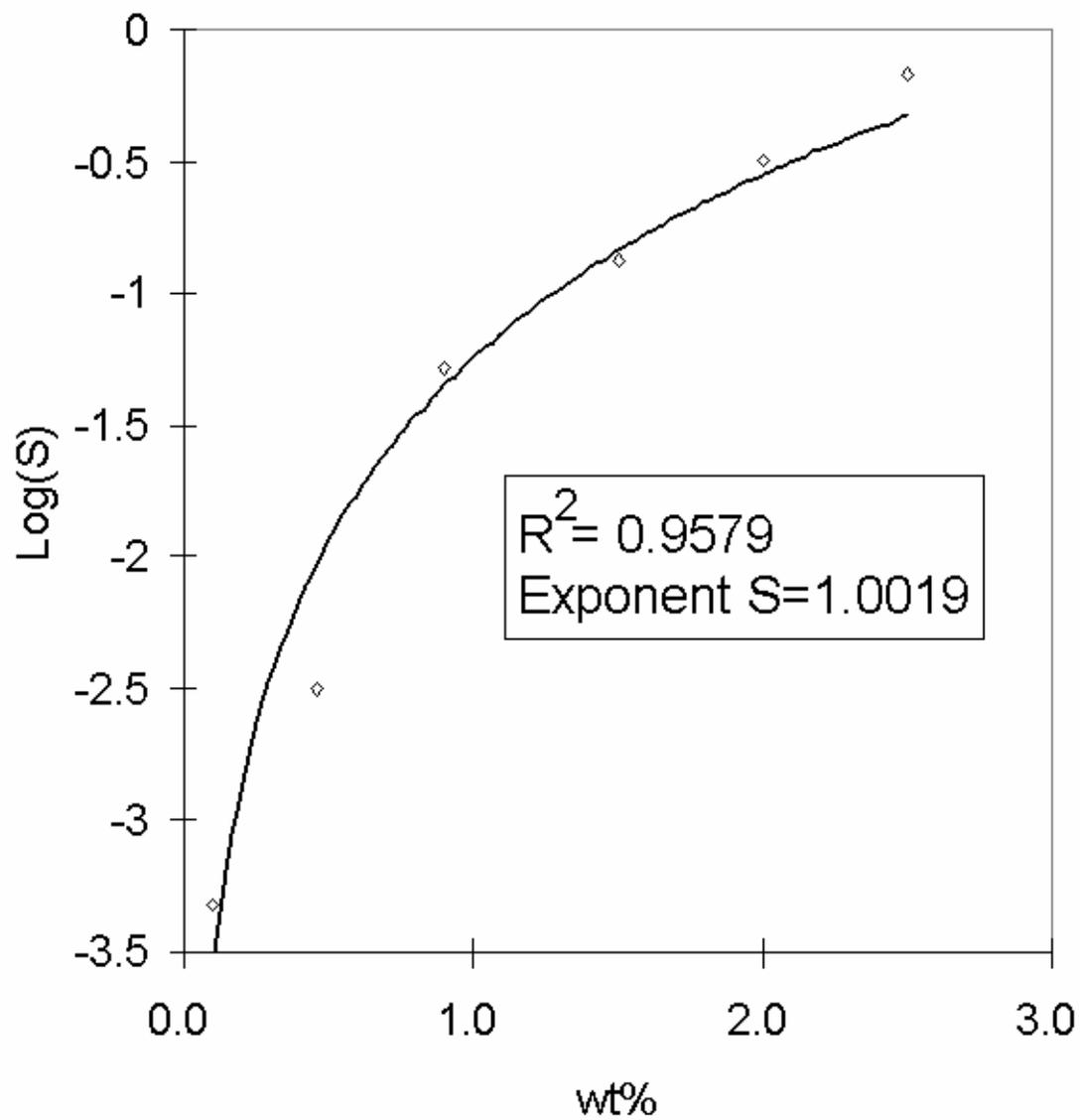
Figure 3.9   SWNT-emulsion polymer percolation curve
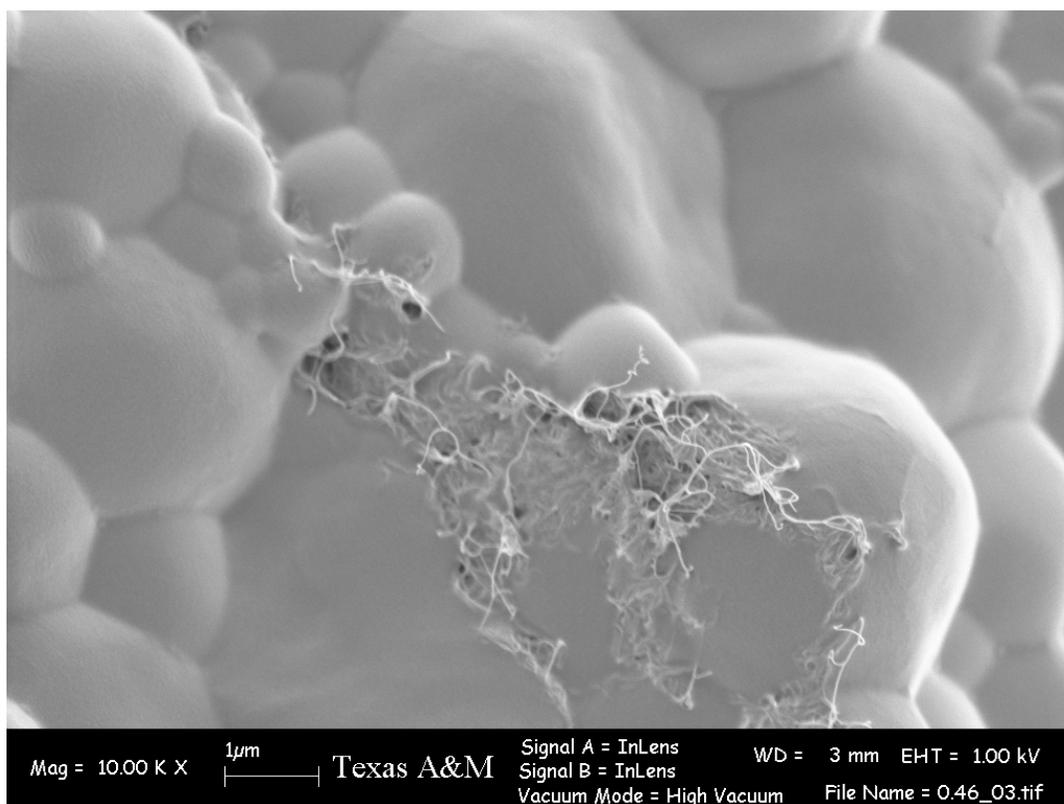
Figure 3.10   SEM image of SWNTs in Vinac emulsion polymer

These solid particles push the SWNTs in the interstitial space between them. This severely restricts the space to which the SWNTs can migrate to, thereby reducing the percolation threshold. The polymer molecules then interdiffuse or coalesce to form a coherent film. This is referred to as the segregated network concept, and was first formalized by Kusy [65]. Figure 3.10 shows an SEM image of the SWNTs in Vinac that shows clearly the interdiffusion of the polymers, and the SWNTs locked in place. For this system of polymer-nanoparticle, we were unable to obtain quantitative measurements of dispersion, as the image analysis algorithms were unable to clearly distinguish between the SWNTs and polymer.

3.4   Image Analysis

A few SEM images are presented to judge the level of dispersion that is obtained by using the mixer for SWNT-epoxy composites. Figure 3.11 (a)-(c) are SEM images of composites prepared by hand-mixing the SWNTs into the epoxy, while Figure 3.11 (d)-(f) are those of composites prepared using the mixer. All these images are of composites having a 0.2 wt% loading of SWNTs, and obtained under identical conditions. The hand mixed composites were seen to have large SWNT clusters, while those prepared using the mixer had smaller clusters. This indicates that the mixer is effective at breaking down large clusters into smaller ones. It must be noted at this point that owing to the magnification chosen, the empty area between SWNT clusters in the hand-mixed composites is not clearly visible. Evidence of shear alignment is also seen in the mixer-prepared composites, especially in Figure 3.11 (d).
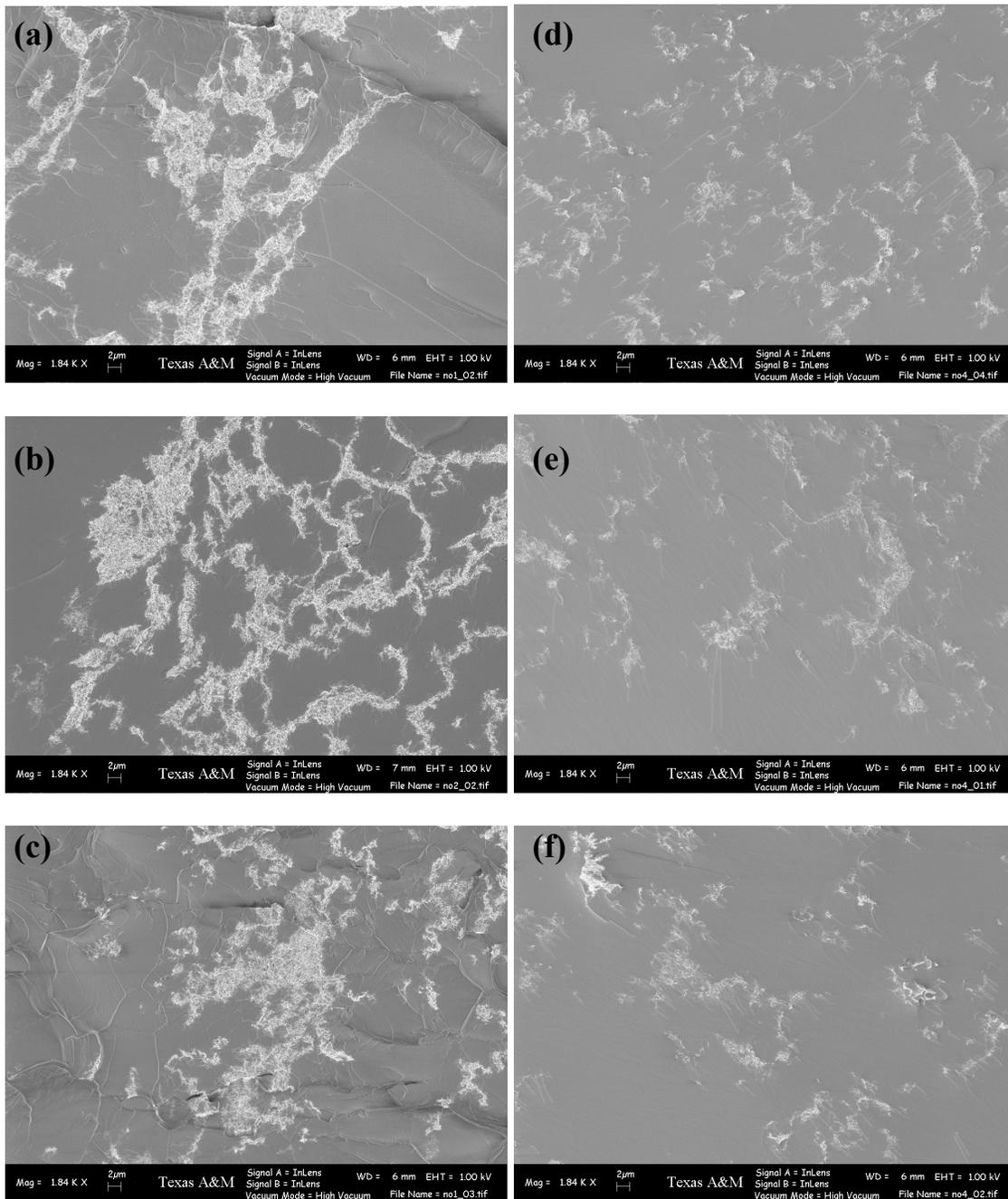
Figure 3.11   SEM images of SWNT-epoxy composites (a),(b),(c) hand mixed (d),(e),(f) mixer run
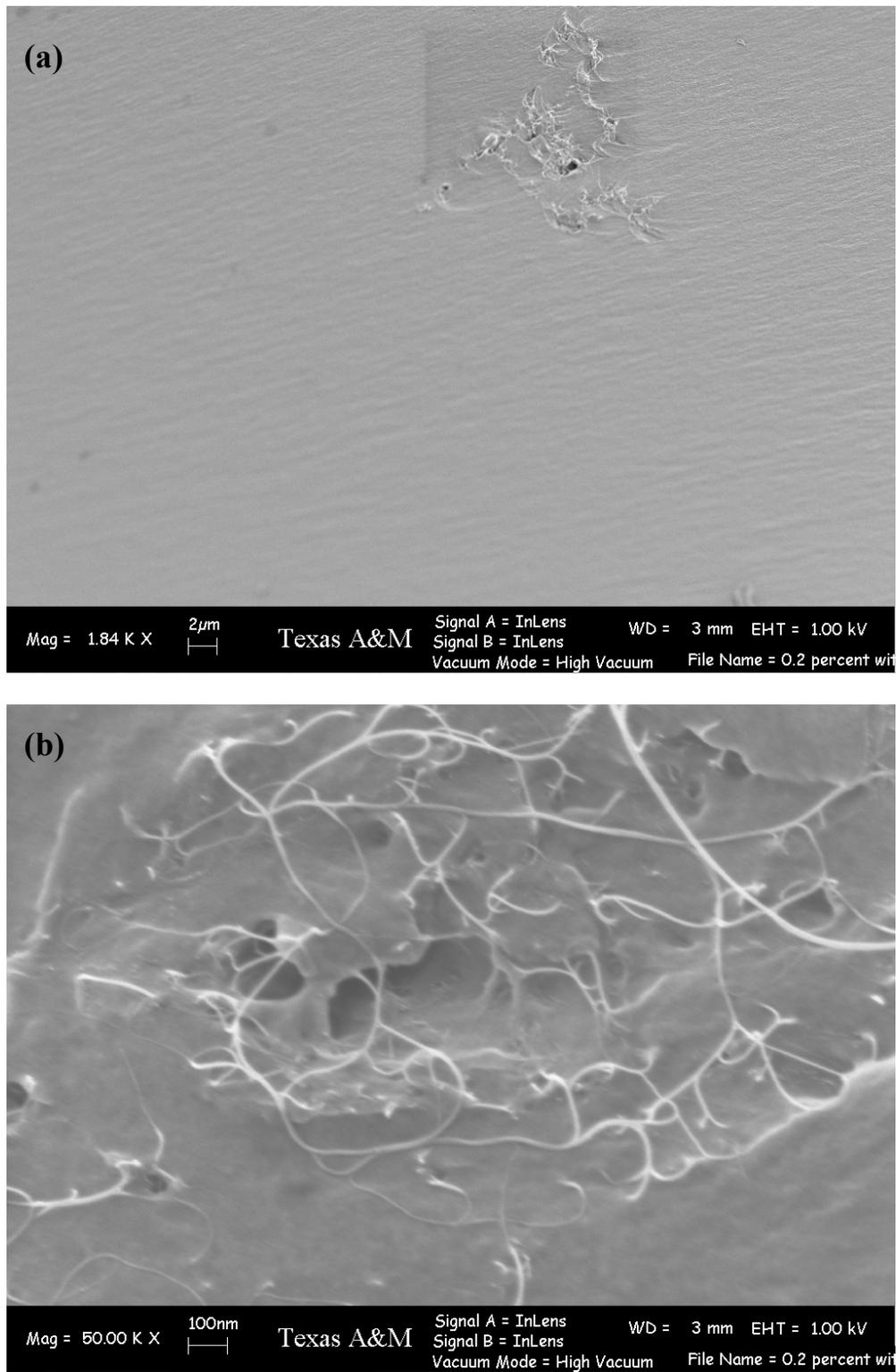
Figure 3.12   SEM images of PVP stabilized SWNTs in epoxy

Composites prepared using PVP-stabilized SWNTs were also imaged. These images show very few SWNT clusters on a highly textured fracture surface, as seen in Figure 3.12 (a). Two phenomena are thought to cause this. Firstly, Since PVP serves to separate the SWNT ropes into individual SWNTs, as shown in section 3.2, the SWNTs are not visible at a magnification of 1840X. Magnifying one of the clusters, as shown in Figure 3.12 (b), a number of SWNTs that appear fainter than the rest are seen. These SWNTs appear to be just below the surface of the epoxy matrix. Secondly, as seen in section 3.3, the interaction of PVP-wrapped SWNTs with the epoxy matrix is stronger than that of the unwrapped SWNTs. Thus, for the unwrapped SWNTs, during the process of fracturing a composite specimen, sites where SWNTs are located serve as voids, resulting in breakage occurring at these sites, and leading to the presence of SWNTs on the fracture surface. In contrast, the PVP-wrapped SWNTs have a stronger interaction with the epoxy matrix. Therefore, the epoxy breaks less preferentially at sites where SWNTs are located, thereby leading to fewer SWNTs present on the fracture surface. Thus, the PVP-stabilized SWNTs were not analyzed by the image analysis algorithms.

Figure 3.13 shows two SEM images (one hand mixed, and the other mixer run) and their corresponding entropy (texture) map, as computed using method A as described in section 1.4. Three levels of entropy can be distinguished: 1) SWNT clusters, that have an entropy of about 5.5; 2) Borders of these clusters and the texture obtained due to polymer fracture having entropy of about 4.5; 3) Polymer background, having entropy of about 3.25.
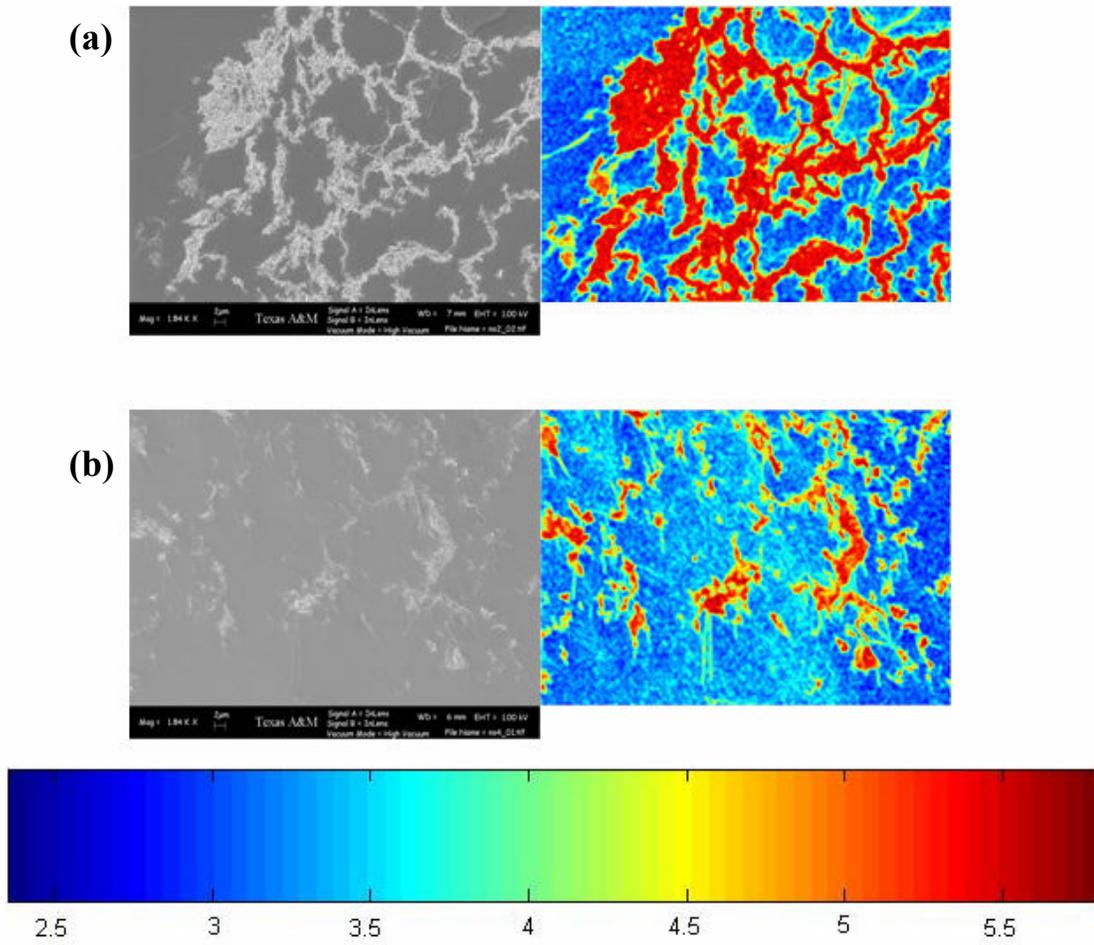
Figure 3.13   SEM images and corresponding entropy image (a) hand mixed (b) mixer run
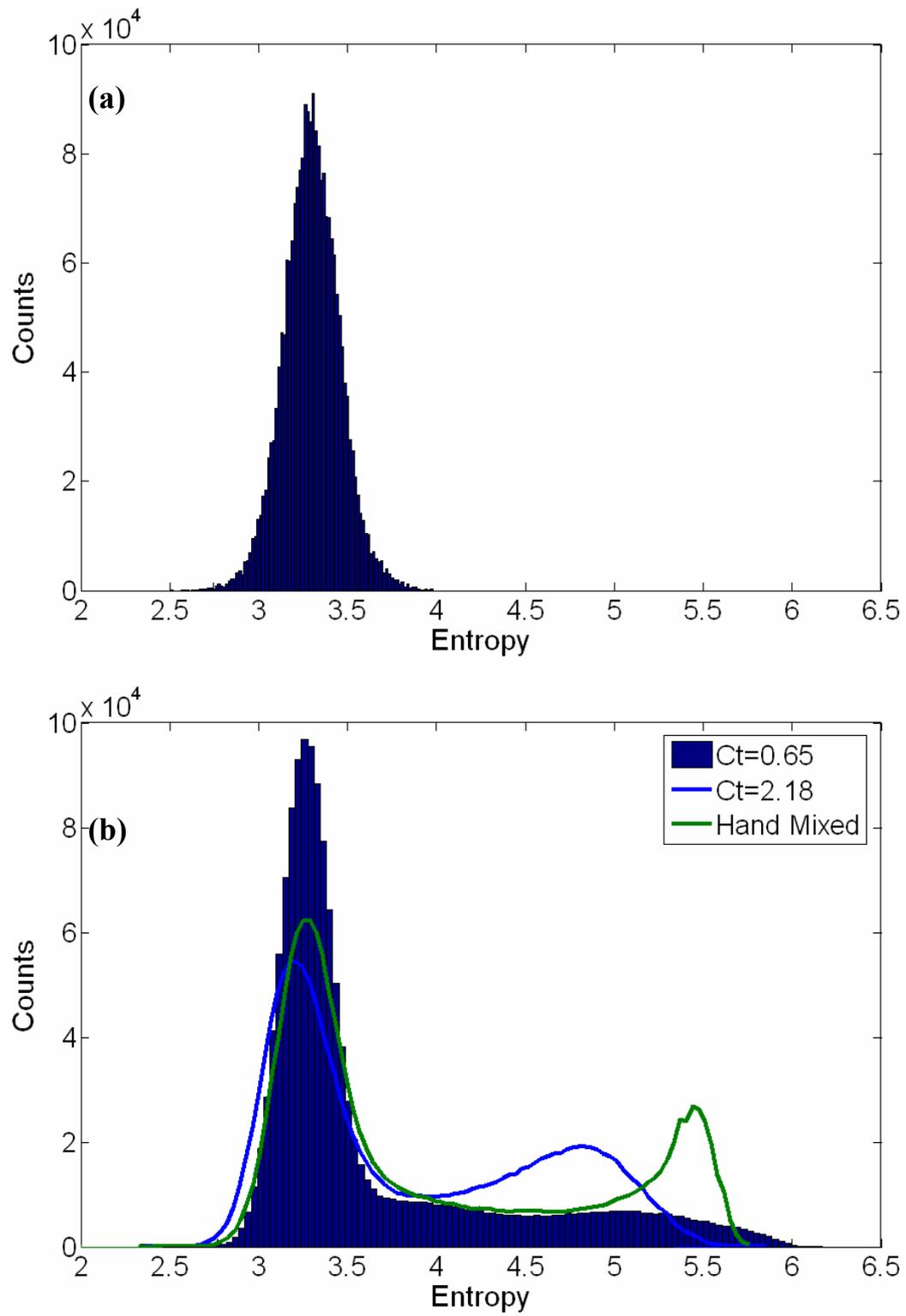
Figure 3.14   Entropy histograms of (a) plain epoxy (b) SWNT-epoxy composites

Four different sets of SEM images were considered, namely images of the plain epoxy, hand-mixed composites, and composites prepared at C_t=2.18 and C_t=0.65. Histograms of the entropy occurrences were plotted. A total of 10^6 data points were divided into 100 bins to plot the histograms. Figure 3.14 (a) shows the histogram obtained from plain epoxy images. A single peak at an entropy of ~3.25 is seen. Figure 3.14 (b) shows histograms from the composites prepared by hand-mixing and the mixer. For composites prepared by hand-mixing, two distinct peaks are seen. The peak on the left at entropy of ~3.25 is due to the polymer background, while the second peak at entropy ~5.5 corresponds to SWNT clusters. For the composite prepared using the mixer at C_t=2.18, the SWNT-peak is seen to shift to the left and broaden, indicating that some of the SWNT clusters are broken down into smaller clusters. For the composite prepared at C_t=0.65, this peak is seen to flatten out almost completely. This indicates that the mixer is indeed efficient at breaking SWNT clusters into smaller ones. For C_t=0.33 composites, the histogram of the SEM images was identical to the histogram of C_t=0.65 composites. An average entropy may be computed for such a histogram, but the choice of weighting factors was not clear. This prompted the use of method B, as described in section 1.4 to assign an index of dispersion that is representative of the degree of dispersion of SWNTs in epoxy.

Table 3.3 summarizes the parameters used in the image analysis of the composite specimens using method B.

Table 3.3   Summary of image analysis parameters

| Composite	Number of Images	Total Physical Area Analyzed (μm^2)	Number of Occupied Pixels (P)	Percentage Area covered by occupied pixels	$\dfrac{P - P(Handmixed)}{P(Handmixed)} x100$
Hand Mixed	153	552347.8	7352107	6.791	0
C_t=2.18	153	552347.8	7314219	6.756	-0.515
C_t=1.03	153	552347.8	7296586	6.739	-0.755
C_t=0.65	153	552347.8	7285134	6.729	-0.910
C_t=0.33	153	552347.8	7278629	6.723	-0.999
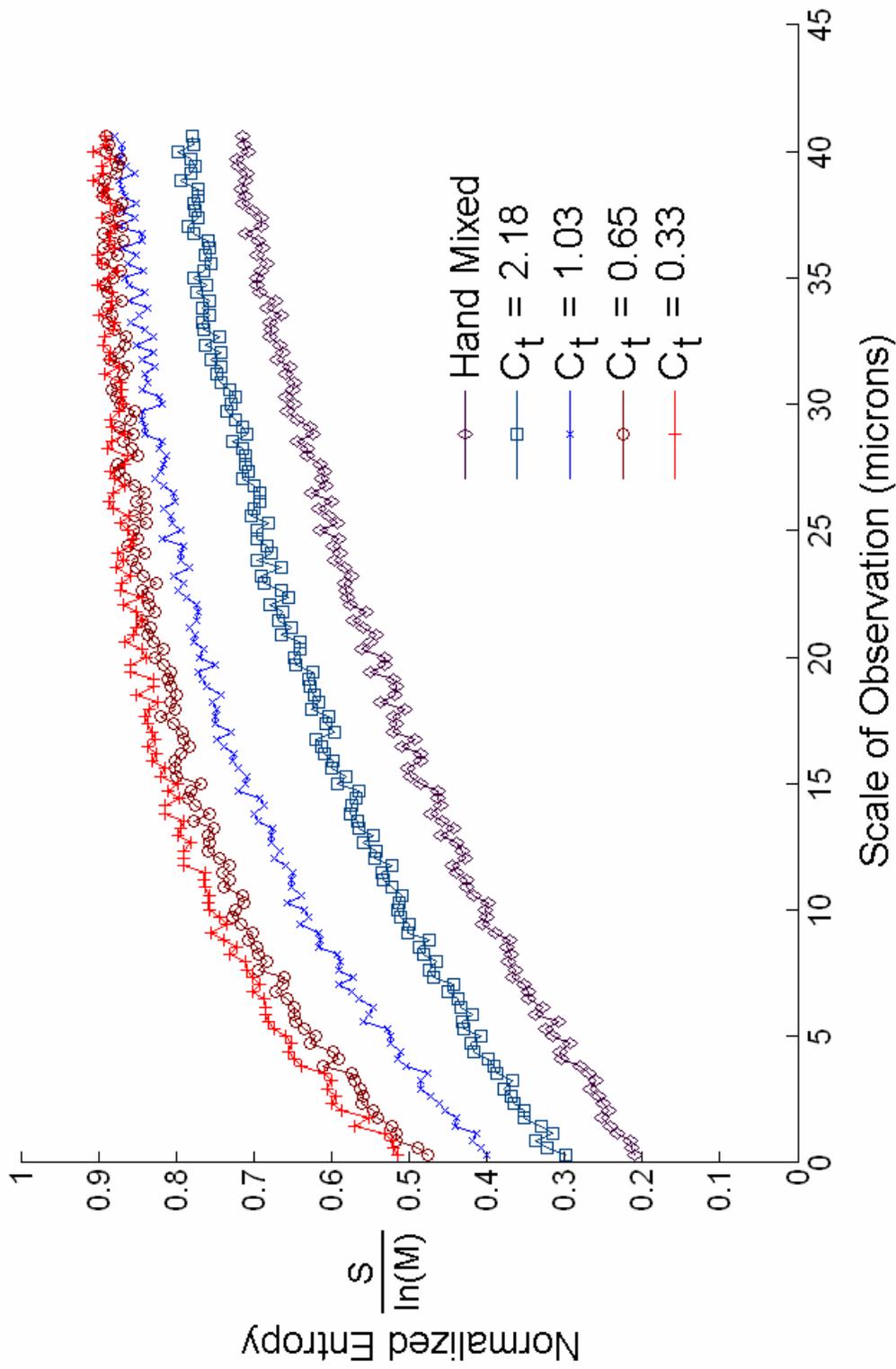
Figure 3.15   Normalized entropy for various composites as a function of bin size

It is noted from Table 3.3 that the total area analyzed is the same for all sets of images, and the difference in number of occupied pixels over which the analysis is carried out is within 1%. Figure 3.15 shows a plot of the entropic index of mixing as a function of bin size for the five different composite samples. For the lowest bin size (scale of observation), an entropic index in the range 0.2-0.5 was obtained. The lowest index was for the hand-mixed composites, while the highest was for composites prepared at C_t=0.33. This index was seen to increase with the scale of observation for all composites, maintaining the lowest index for hand-mixed composites, and the highest for composites prepared at C_t=0.33. Thus, it may be concluded that the dispersion of SWNTs becomes more homogeneous with decreasing C_t. This behaviour is consistent with the electrical conductivity measurements obtained in section 3.3. The difference in the entropic index between composites prepared at C_t=0.65 and those prepared at C_t=0.33 was small. This indicates that the flocs of SWNTs in these composites are of comparable size. Electrical conductivity measurements, on the other hand, indicate a significant difference between these two composites. This discrepancy is thought to be caused by the low resolution of the SEM images that are unable to capture details smaller than 58 nm. Higher resolution images coupled with a smaller scale of observation are expected to yield better results.

4. NUMERICAL TECHNIQUE

4.1 Introduction

The steady-state Reynolds Average Navier Stokes Equations that were solved are given in index notation as

$$\overline{u}_j \frac{\partial \overline{u}_i}{\partial x_j} = g_i - \frac{\partial \overline{P}}{\partial x_i} - \frac{\partial \overline{u_i' u_j'}}{\partial x_i} + \nu \frac{\partial^2 \overline{u}_i}{\partial x_j^2} \qquad (4.1)$$

where the overbar represents average values

All computations were performed using FLUENT. A 2D axisymmetric solver was used to perform preliminary computations on coaxial ducted jets, to study the effect of Re_j and C_t variation. A square cell arrangement was used for this purpose. A 3D solver was used to perform computations on a domain that used the actual mixer geometry. For these computations, a tetrahedral meshing scheme was used. For all 3D simulations, the cell volume used was 1.95×10^{-13} m^3, while the total domain volume was 7.75×10^{-6} m^3. A standard k-ε turbulence model was used. A SIMPLE pressure solver was used to couple velocity and pressure. A first order upwinding scheme was used for momentum, turbulence kinetic energy and turbulence dissipation rate. The solution was considered to be converged when the largest residual (among continuity, velocity, k and ε) was less than 10^{-6}. Figure 4.1 shows the side view of the 3-D computational domain.
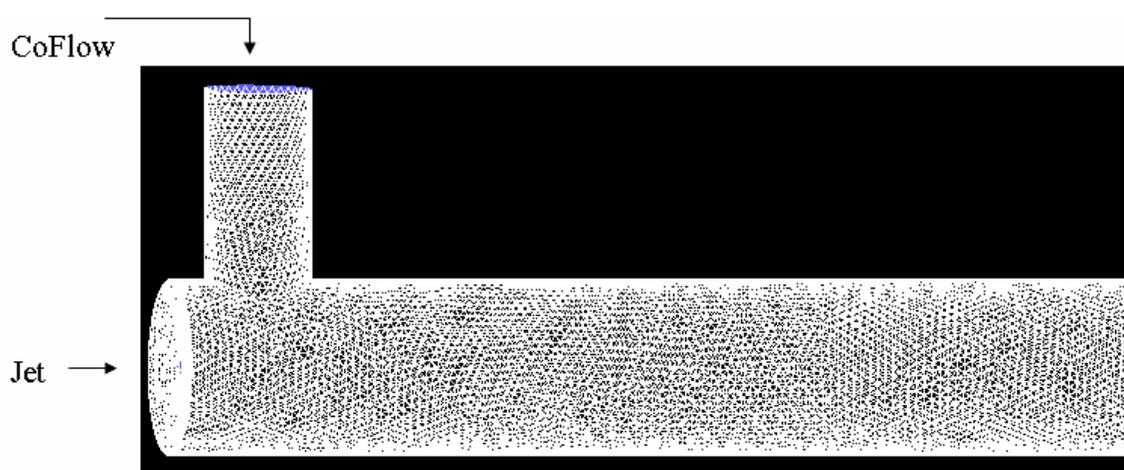
Figure 4.1   Side view of computational domain

In the computational domain, the length of the mixing tube was longer than the actual mixer. This was necessary because of the exit boundary condition which required that the flow not be recirculating at the exit. To study the effect of C_t variation, four simulations were run at C_t values of 0.33, 0.65, 1.03 and 2.18. Re_j for all of these was kept constant at 4000. The parameters used for these simulations correspond to the experimental parameters that were used to disperse SWNTs in epoxy, as outlined in section 2.4.2. The effect of increasing Re_j was studied via more numerical simulations, in which, the Re_j values used were 3000, 5000 and 6000.

The computations were checked for grid independence by coarsening the grid and running simulations at $C_t = 0.33$. Two simulations with coarser grids were run. These grids had cell volumes 8 and 27 times that of the original grid. Figure 4.2 shows the original fine grid and the two coarser grids, while Figure 4.3 shows the corresponding pathlines obtained for these grids. The pathlines for the coarser grids show that the size of the primary recirculation zone is comparable for all three grids. Since dispersion is a function of the size of the primary recirculation zone, the simulations were considered grid independent for purposes of SWNT dispersion. Multiple eddies are seen within the primary recirculation zone for the coarser grids, which indicates that the small-scale behaviour of the recirculation zone cannot be captured accurately by the coarser grids.
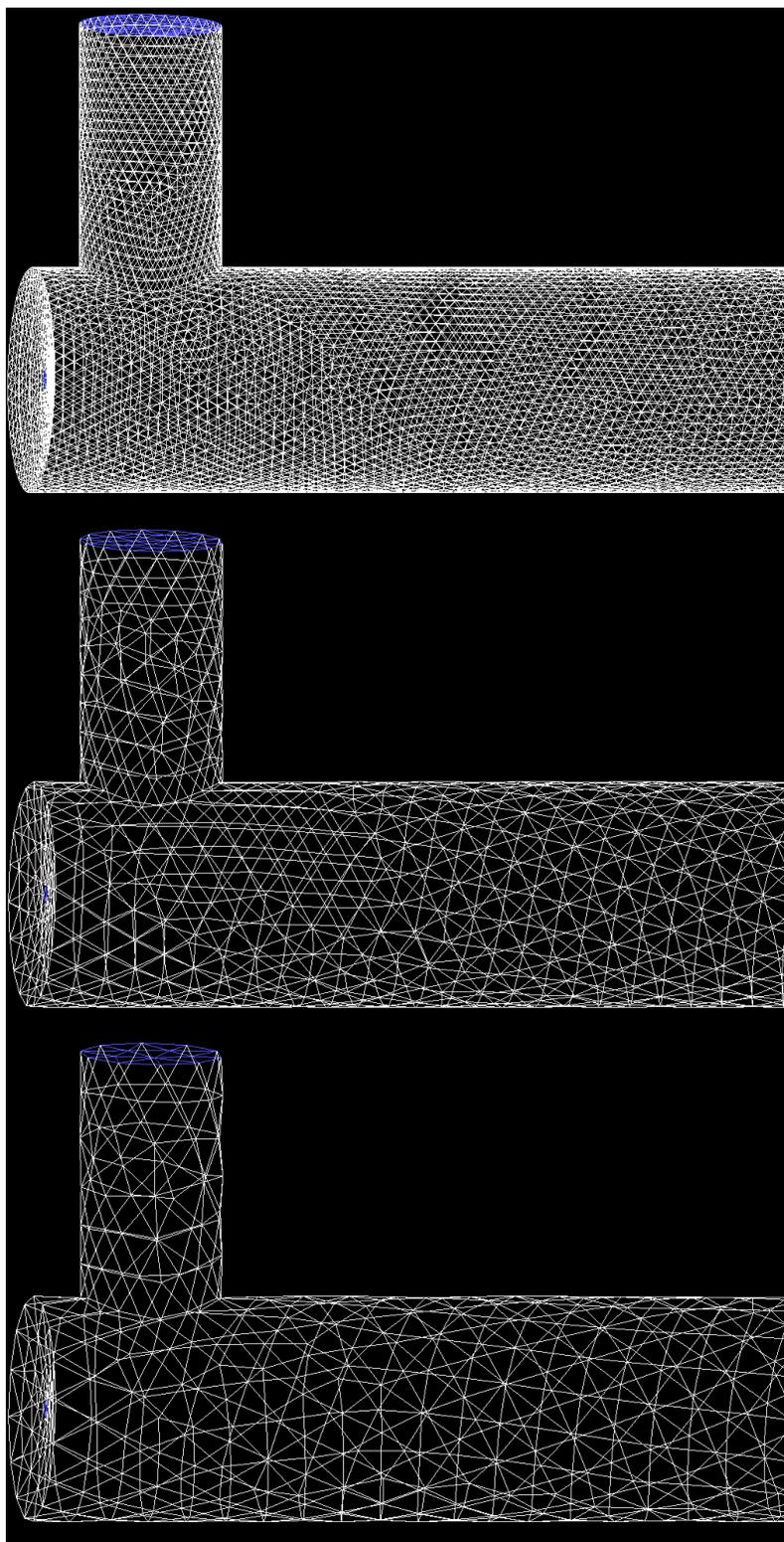
Figure 4.2   Three different grids to check for grid independence

Approximate end of recirculation zone
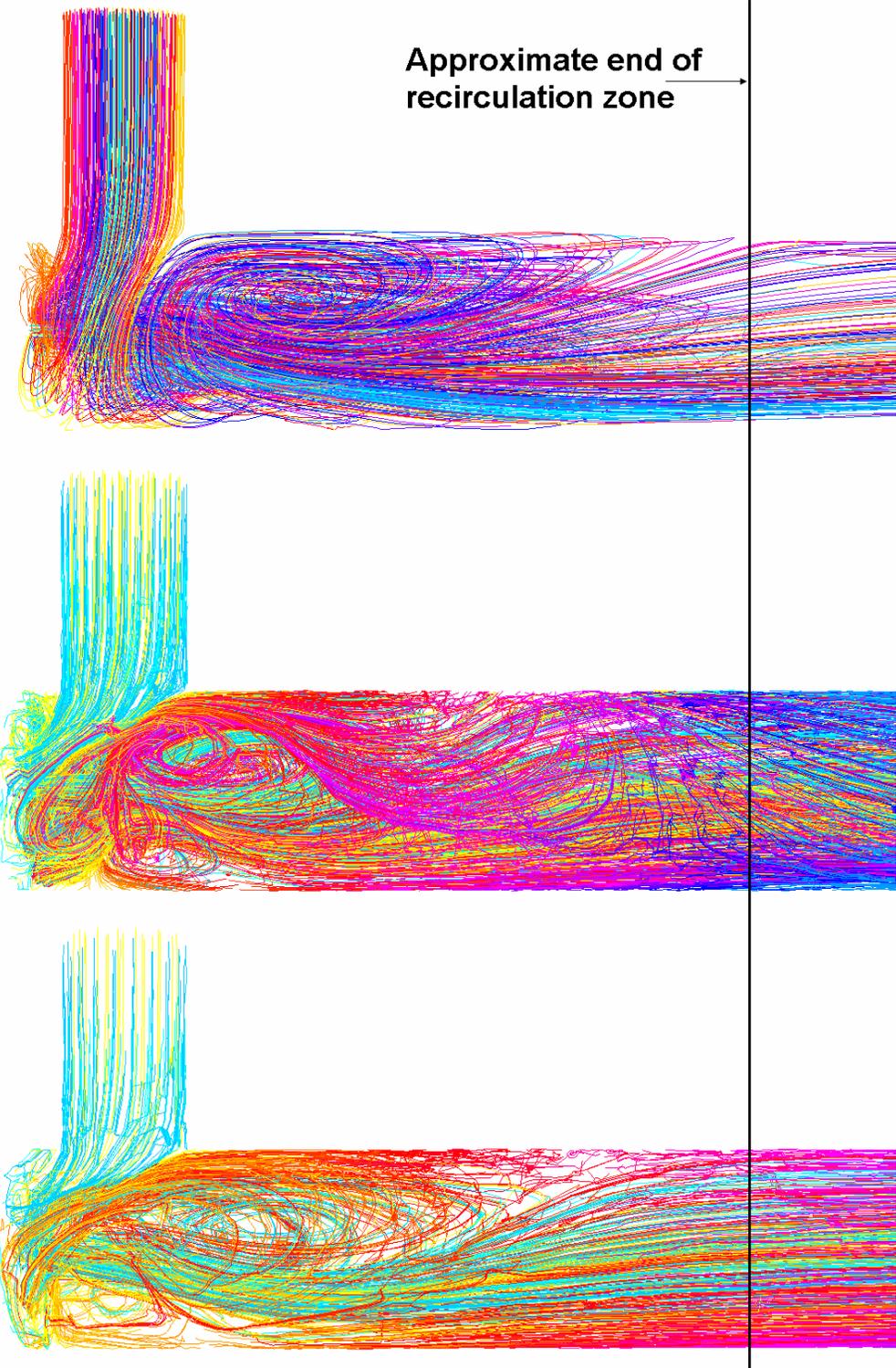
Figure 4.3   Pathlines obtained for coarser grids

4.2   *Numerical Results*

Pathlines for the flow field were computed, and are shown in Figure 4.4-Figure 4.7 for the four different cases. It is seen that when operating above the critical C_t, there is a single recirculation zone that forms in the mixer (Figure 4.4 and Figure 4.5). This is due to the 90-degree bend that the co-flowing stream undergoes. As C_t is reduced below its critical value to 0.65, a second recirculation zone is seen to form at the bottom of the mixing chamber. This is because the momentum demands of the jet are not met by the co-flowing stream, as outlined in section 1.3. At $C_t=0.65$ (Figure 4.6) the recirculation zone due to the bend is anticlockwise, while the second recirculation zone is clockwise. At $C_t=0.33$ (Figure 4.7), the single recirculation zone is clockwise. This leads to the conclusion that the second recirculation zone grows and engulfs one due to the 90-degree bend. Comparing the two extreme cases, it is seen that at $C_t=2.18$, a significant portion of the fluid entering the mixer exits without undergoing significant recirculation.
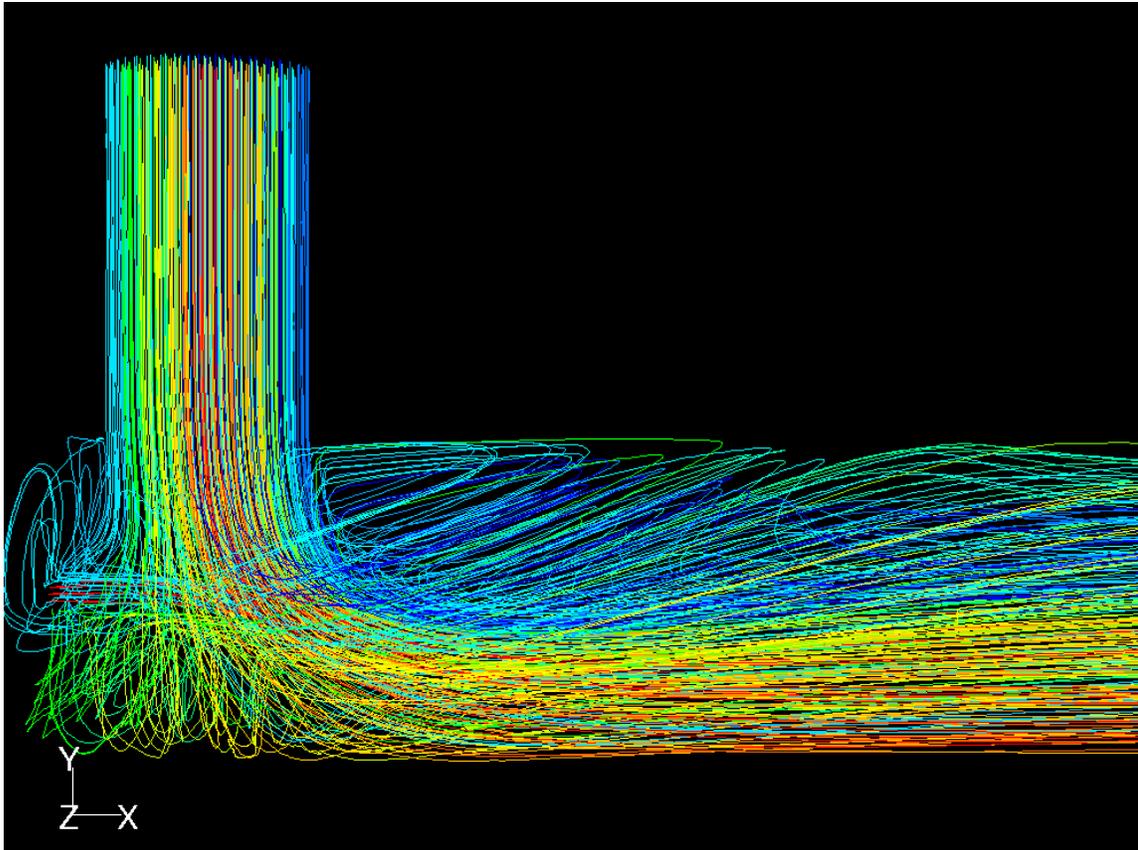
Figure 4.4   Pathlines obtained for C_t=2.18, Re_j=4000
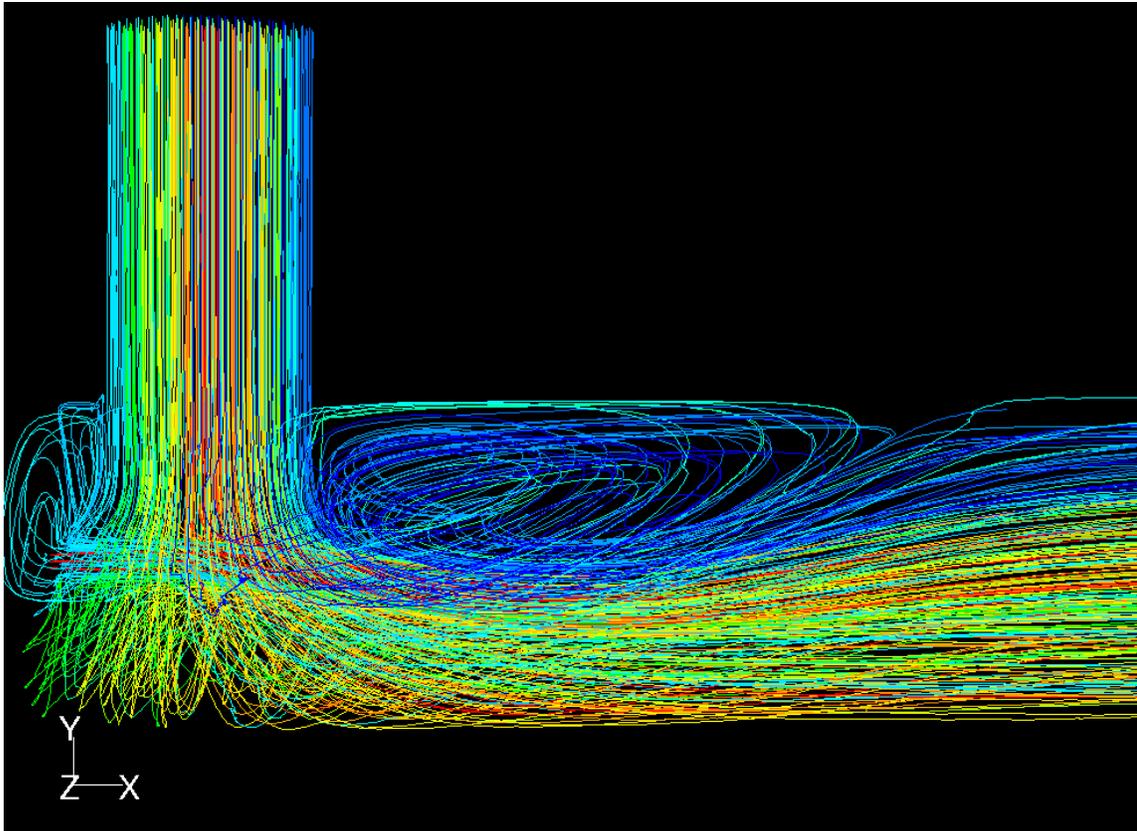
Figure 4.5   Pathlines obtained for C_t=1.03, Re_j=4000
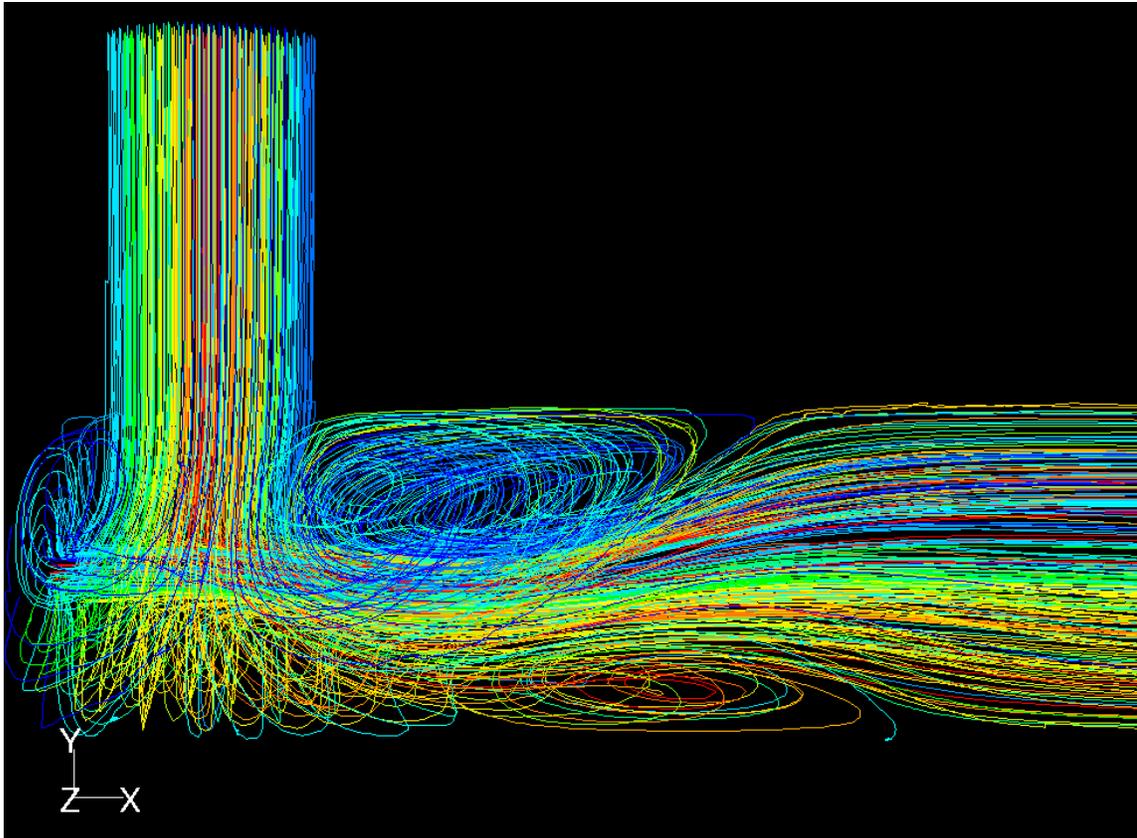
Figure 4.6   Pathlines obtained for C_t=0.65, Re_j=4000
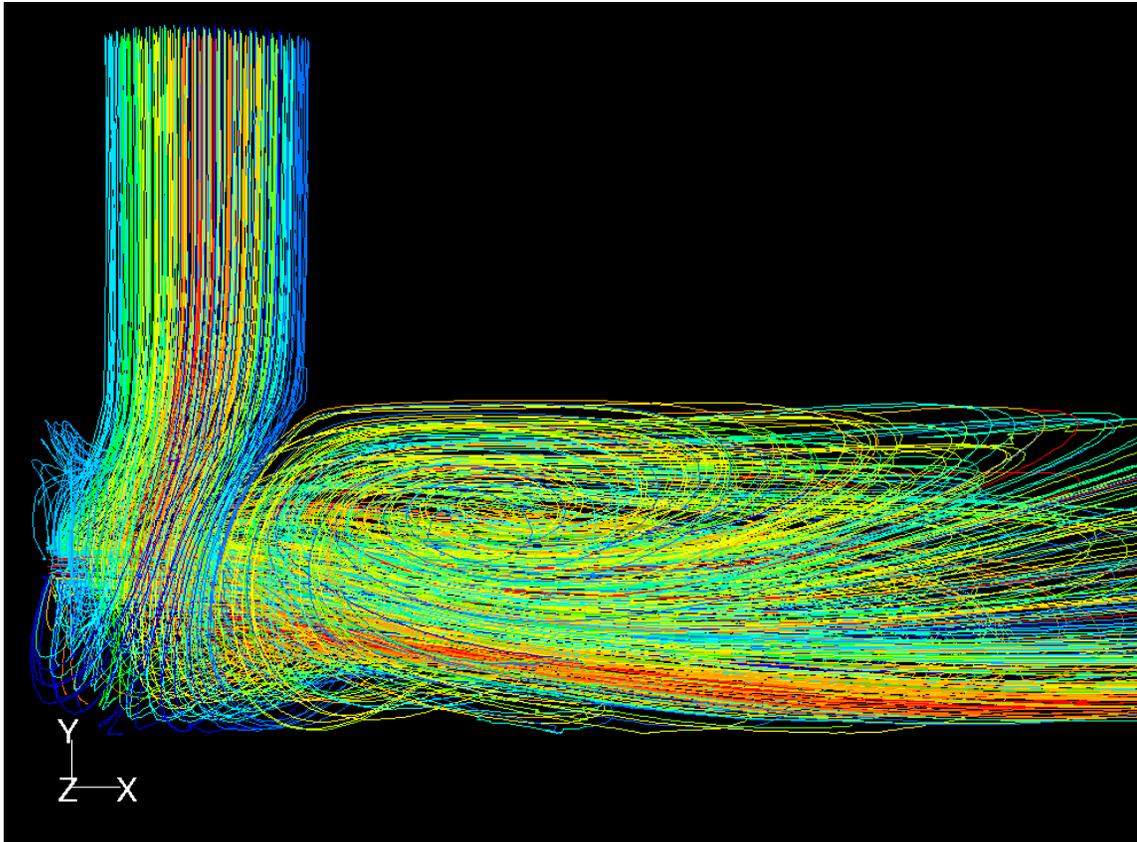
Figure 4.7   Pathlines obtained for C_t=0.33, Re_j=4000

At C_t=1.03, the size of the first recirculation zone is seen to increase slightly. When the second recirculation zone forms at C_t=0.65, a larger portion of the fluid that enters the mixer is vigorously mixed, and at C_t=0.33, the recirculation zone fills the whole mixing chamber, and a large portion of the fluid that exits the mixer is well mixed. Thus, it may be concluded that as C_t is lowered, the appearance and subsequent increase in the size of the recirculation zone increases the residence time of fluid within the mixer, leading to better mixing.

Figure 4.8 shows the pathlines obtained for C_t=0.33 and Re_j=6000. It is observed that the shape and size of the recirculation zone does not change significantly with a change in Re_j, although the size is seems to increase by a small amount. This observation is the same as that obtained in the case of co-axial jets, as seen in section 1.3. Thus, increasing Re_j is expected to improve the degree of dispersion that can be obtained using the mixer.

4.3   *Comparison with Experiments*

For the cases where C_t = 2.18 and C_t = 1.03, the dispersion of SWNTs was not the highest obtainable. As C_t is lowered to a value below the critical C_t, the formation and subsequent increase in the size of the recirculation zone leads the nanoparticles that are present in the fluid to undergo recirculation for a longer time. This means that the flocs of SWNTs in the fluid are exposed to high shear for a longer period of time, leading to better dispersion of nanoparticles.
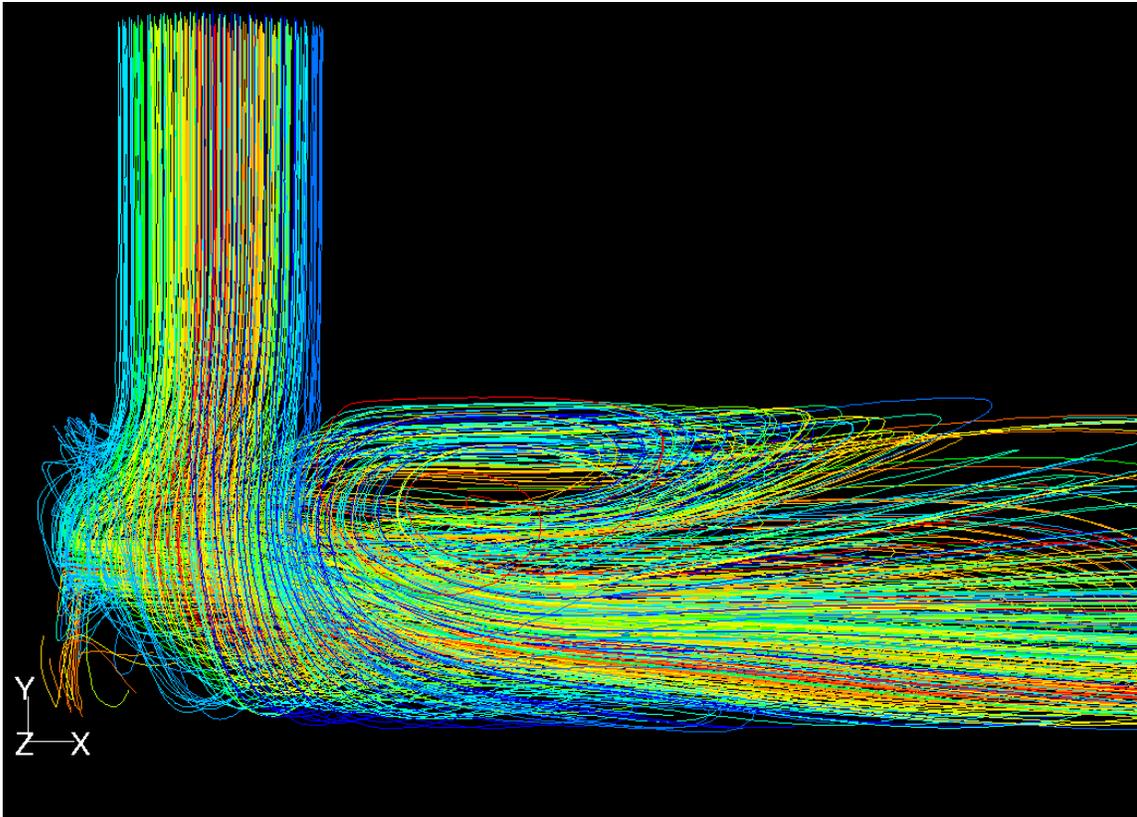
Figure 4.8   Pathlines obtained for C_t=0.33, Re_j=6000

Evidence for this is seen in the image analysis and electrical conductivity measurements. The behaviour of aggregation and breakup of colloidal particles in turbulent shear flow has previously been studied by Serra et al. [66], who found that the typical floc size is on the order of the Kolmogorov length scale, or dissipative length scale. This length scale for the mixer is given by

$$\eta = \frac{D_j}{\left(\mathrm{Re}_j\right)^{0.75}}$$
(4.2)

Inserting the operating parameters of the mixer, we get a dissipative length scale of 1.5 microns. From the SEM images of composites prepared using the mixer in Figure 3.11, we do indeed see that the typical floc size is indeed on the order of this size. Larger flocs were also seen in the SEM images. The occurrence of large flocs was more prominent in SEM images obtained from composites prepared at $C_t > 1$, and poor mixing is thought to be a contributing factor. Figure 4.9 shows two SEM images of a composite prepared at $C_t = 2.18$ that illustrates the presence of a range of floc sizes. This is thought to be because at high C_t, a large portion of fluid leaves the mixer without undergoing significant recirculation.
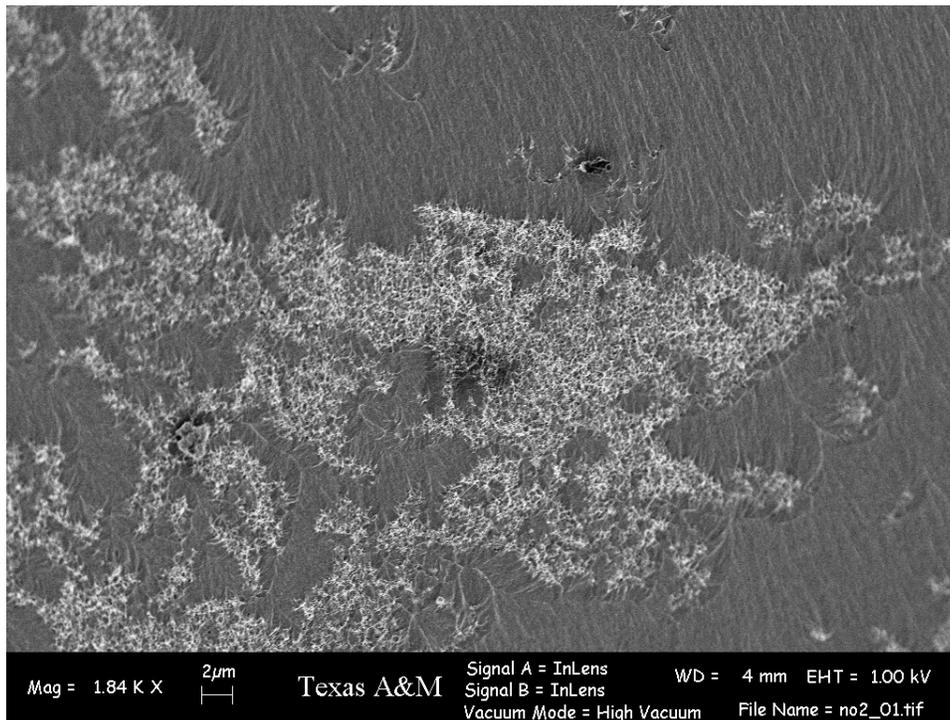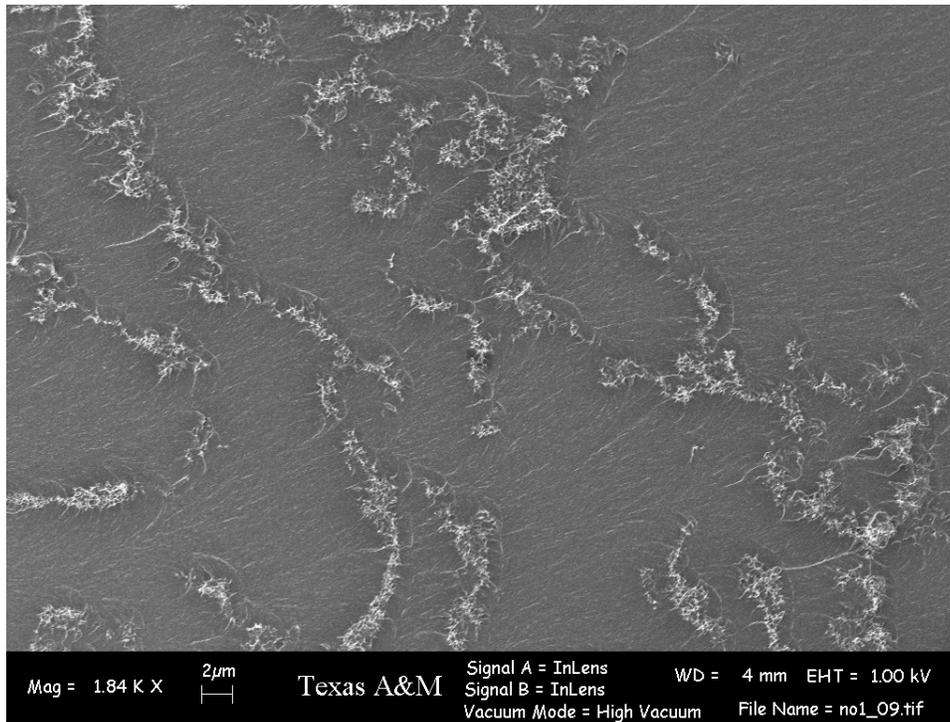
Figure 4.9   SEM images of composites prepared at C_t=2.18

5. CONCLUSIONS AND RECOMMENDATIONS

A continuous impingement mixing process has been designed and studied using experiments and numerical simulations. The experiments involved dispersing SWNTs in different polymers. The dispersion of SWNTs was studied by electrical conductivity measurements and SEM image analysis. Distinguishing SWNTs from the polymer matrix in the SEM images was performed by an Iso-data thresholding algorithm and a maximum entropy thresholding algorithm. Using the concept of Shannon Entropy, an entropic index of mixing was assigned to a set of SEM images that was representative of the degree of dispersion of SWNTs. Sedimentation of SWNTs was studied by measuring electrical resistivity of the composites. The SWNTs were also stabilized using PVP to yield better dispersion. The significant conclusions of this work are summarized below.

- Impingement mixing is a novel, relatively simple process for effective dispersion of nanoparticles in polymers.

- A key governing parameter was the Craya-Curtet Number (C_t), which is the ratio of co-flowing stream momentum to jet momentum. When this number is decreased below the critical value of 0.75, a recirculation zone was seen to form within the mixer. Further reduction of this parameter enlarged the recirculation zone.

- Another parameter of importance was the Reynolds number (Re_j). Increasing this parameter was seen to increase (albeit by a small amount) the size of the

recirculation zone. It is believed that increasing Re_j would further promote mixing, but not significantly.

- Sedimentation of SWNTs was not found to be a significant issue, as the small diameter of SWNTs makes them more susceptible to Brownian motion, thereby reducing the tendency to settle under gravity. For larger nanoparticles, the importance of sedimentation is expected to increase with nanoparticle size.

- The entropic index of mixing may be used for any nanoparticle-polymer combination, where the nanoparticles can be distinguished from the polymer.

In future work, it is possible to use the flow field, as calculated by simulations, to obtain a floc size distribution, and thereby compute a theoretical degree of dispersion. Indeed, some work has been done in this direction by other research groups [66], although only the simplest case (cylindrical Couette flow) has been considered.

The following recommendations are proposed for future experiments:

- The current system is set up to handle small volumes of material. Pumps may be used if handling larger volumes of material is required.

- The epoxy was cured to its full extent before any testing was carried out. This was not entirely beneficial for purposes of image analysis, as it introduced texture on the polymer fracture surface. Incomplete curing of the epoxy would cause the material to have a clean fracture surface that would then minimize the use of thresholding algorithms.

- It was also thought that an excess amount of PVP was present in the epoxy composites. Washing the PVP-stabilized SWNTs repeatedly with water would remove any excess PVP.

- This mixing process cannot effectively handle highly viscous fluids. The polymers that were tested using this mixing process were all diluted with a solvent which was then evaporated. In many cases, heating the polymer will serve to reduce its viscosity and thus eliminate the need for solvent, thereby reducing the process time and also reducing the sedimentation of nanoparticles. This method, however, cannot easily be applied in the case of emulsion polymers.

- The minimization of sedimentation can be used to study more accurately the effect of C_t on the mixing process. Indeed, the image analysis showed little difference between composites prepared at $C_t=0.65$ and those prepared at $C_t=0.33$. This was attributed to long curing times.

- The image analysis technique has its limitations in distinguishing between SWNTs and polymer background. Human intervention was necessary in some cases.

- Sedimentation of nanoparticles can be studied more accurately using a laser light scattering system.

- The low concentration of PVP-stabilized SWNTs hindered the study of their dispersion in a polymer matrix as it was difficult to locate SWNTs on the surface of the composites. A high concentration of SWNTs would facilitate this study.

- Measurement of dispersion of SWNTs in the elastomer was difficult in the conventional SEM. Environmental SEMs (E-SEMs) are designed to operate at varying chamber pressures and may be used to obtain images of composites which may then be processed using the image analysis scripts.

- Some shear-induced alignment was seen in the SWNT composites. While it is extremely difficult to obtain aligned SWNTs in a polymer, it would be worthwhile to study the dependence of SWNT alignment on the dispersion and composite properties.

In summary, the mixing process developed over the course of this dissertation is an "enabling" process which has been shown to be efficient at dispersing SWNTs in a variety of polymers. It is a continuous flow process, as opposed to a batch process that is capable of handling large amounts of material without geometrical scale-up. It is believed that this process may be used for virtually any polymer-nanoparticle combination. Measurement of dispersion continues to be a significant question. The entropic analysis used in this dissertation is but one of the numerous statistical routes that may be employed. Image analysis is fast gaining importance in the scientific community, as a cheap, reliable and effective means of data analysis. Advances in computing will further aid in the popularity of this technique.

REFERENCES

1. Wei D., Dave R. and Pfeffer R. 1998 *J. Nanopart. Res.* **4** 21

2. Zilg C., Thomann R., Mülhaupt R. and Jurgen F. 1999 *Adv. Mater.* **11** 49

3. Pattanayak A. and Jana S.C. 2005 *Polymer* **46** 3275

4. Shao W., Wang Q. and Ma H. 2004 *Polym. Int.* **54** 336

5. Pu H. and Jiang F. 2005 *Nanotechnology* **16** 1486

6. Ciambelli P., Sarno M., Gorrasi G., Sannino D., Tortora M. and Vittoria V. 2005 *J. Macromol. Sci. Phys.* **44** 779

7. Li F., Zhou S., Gu G., You B. and Wu L. 2005 *J. Appl. Polym. Sci.* **96** 912

8. Alexandre M. and Dubois P. 2000 *Mat. Sci. Eng. R.* **28** 1

9. Grunlan J.C., Mehrabi A.R. Bannon M.V. and Bahr J.L. 2004 *Adv. Mater.* **16** 150

10. Burke N.A.D., Stöver H.D.H., Dawson F.P., Lavers J.D., Jain P.K. and Oka H. 2001 *IEEE T. Magn.* **37** 2660

11. Dyke C.A. and Tour J.M. 2004 *J. Phys. Chem. A.* **108** 11151

12. Petrov P. Lou X., Pagnoulle C., Jérôme C., Calberg C. and Jérôme R. 2004 *Macromol. Rapid Comm.* **25** 987

13. Ramanathan T., Liu H. and Brinson L.C. 2005 *J. Pol. Sci. Pol. Phys.* **43** 2269

14. Andrews R., Jacques D., Minot M. and Rantell T. 2002 *Macromol. Mater. Eng.* **287** 395

15. Wilson J.L., Poddar P., Frey N.A., Srikanth H., Mohomed K., Harmon J.P., Kotha S. and Wachsmuth J. 2004 *J. Appl. Phys.* **95** 1439

16. Sennett M., Welsh E., Wright J.B., Li W.Z., Wen J.G. and Ren Z.F. 2003 *Appl. Phys. A-Mater.* **76** 111

17. Curtet R. 1958 *Combust. Flame* **2** 383

18. Craya A. and Curtet R. 1955 *Acad. Sci. Paris* **241** 621

19. Hill P.G. 1965 *J. Fluid Mech.* **22** 161

20. Brighton J.A. and Exley J.T. 1971 *ASME Trans. D – J. Basic Engg.* **93** 192

21. Woodfield P.L., Nakabe K. and Suzuki K. 2000 *Proc. 14th Symposium of the Japanese Society of Computational Fluid Dynamics* Paper No. C04-1

22. Becker H.A., Hottel H.C. and Williams G.C. 1962 *Proc. Ninth Symposium (International) on Combustion,* **9** 7

23. Barchilon M. and Curtet R. 1964 *Fluids Engg. Conf.* Paper No. 64-FE-23:1-17

24. Revuelta A., Martínez-Bazán C., Sánchez A.L. and Liñán A. 2004 *Phys. Fluids.* **16** 208

25. Lane A.G.C. and Rice P. 1981 *Trans. I. Chem. E.* **60** 171

26. Gonzalez R.C. and Woods R.E. 2002 *Digital Image Processing,* (Englewood Cliffs, NJ: Prentice Hall)

27. Styer D.F. 2000 *Am. J. Phys.* **60** 1090

28. Brandenberger A., Mukhanov V. and Prokopec T. 1993 *Phys. Rev. D.* **48** 2443

29. Schmitt A.O. and Herzel H. 1997 *J. Theor. Biol.* **188** 369

30. Zimmer Y., Tepper R. and Akselrod S. 1996 *Ultrasound Med. Biol.* **22** 1183

31. Smolikova R., Wachowiak M.P. and Zurada J.M. 2004 *Comput. Biol. Med.* **35** 355

32. Devezas T.C. and Corredine J.T. 2002 *Tech. Forecast. Soc. Change* **69** 317

33. Hale J. 2003 *J. Psycholinguistic Research.* **32** 101

34. Bodun P.O., Shibusawa S., Sasao A., Sakai K. and Honaka H. 2000 *J. Terramechanics* **37** 3

35. Cheng H.D., Chen C.H., Chiu H.H. and Xu H. 1998 *IEEE T. Image Process.* **7** 1084

36. Cheng H.D., Jiang X.H. and Wang J. 2002 *Pattern Recogn.* **35** 373

37. Tavakoli N. 1993 *J. Vis. Commun. Image R.* **4** 271

38. Alemaskin K., Camesasca M., Manas-Zloczower I. and Kaufman M. 2004 *AIP Conference Proceedings* **712** 169

39. Camesasca M., Manas-Zloczower I. and Kaufman M. 2005 *J. Micromech. Microeng.* **15** 2038

40. Shannon C.E. 1948 *Bell System Tech. J.* **27** 379

41. Grunlan J.C. and Bannon M.V. 2003 *Mat. Res. Soc. Symp. Proc.* **772** M9.1.1

42. Elbl-Weiser K. 2002 *Nanotechnology in Chemistry, BASF News Release, P346e* 11

43. Biercuk M.J., Llaguno M.C., Rodosavljevic M., Hyun J.K., Johnson A.T. and Fischer J.E. 2002 *Appl. Phys. Lett.* **80** 2767

44. Vivien L., Anglaret E., Riehl D., Bacou F., Journet C., Goze C., Andrieux M., Brunet M., Lafonta F., Bernier P. and Hache F. 1999 *Chem. Phys. Lett.* **307** 317

45. Landi B.J., Raffaelle R.P., Heben M.J., Alleman J.L., VanDerveer W. and Gennett T. 2002 *Nano Lett.* **2** 1329

46. Grunlan J.C., Mehrabi A.R., Bannon M.V. and Bahr J.L. 2004 *Adv. Mater.* **16** 150

47. Ridler T.W. and Calvard S. 1978 *IEEE T. Syst. Man. Cybern.* **SMC-8** 630

48. Sahoo P.K., Soltani S.,Wong K.C. and Chen Y.C. 1988 *Computer Vis. Graph. Im. Process.* **41** 233

49. Barber M.N. and Ninham B.W. 1970 *Random and Restricted Walks: Theory and Applications* (New York: Gordon and Breach)

50. Wang W., Manas-Zloczower I. and Kaufman M. 2001 *Int. Polym. Proc.* **16** 315

51. Wang W., Manas-Zloczower I. and Kaufman M. 2003 *AICHE J.* **49** 1637

52. Ausman K.D., O'Connell M.J., Boul P., Ericson L.M., Casavant M.J., Walters D.A., Huffman C., Saini R., Wang Y., Haroz E., Billups E.W. and Smalley R.E. 2001 *Proc. 15th Int. Winterschool on Electronic Properties of Novel Materials Euroconf., (Kichberg, Tirol, Austria) (AIP Conf. Proc.* vol 519) ed H. Kuzmany, J. Fink, M. Mehring and S. Roth, (New York: American Institute of Physics) p 226

53. Page S.A, Mezzenga R, Boogh L, Berg J.C. and Månson J.E. 2000 *J. Colloid Interf. Sci.* **222** 55

54. Çayakara T, Yerlikaya Z and Kantoğlu Ö. 2004 *J. Appl. Polym. Sci.* **91** 1893

55. Yu M.F., Yakobson B.I. and Ruoff R.S. 2000 *J. Phys. Chem.* B **104** 8764

56. Deutscher G., Kapitulnik A. and Rappaport M. 1983 *Percolation Structures and Processes,* ed Deutscher G., Zallen R., and Adler J., Eds., Annals of the Israel Physical Society, v. 5, (New York: American Institute of Physics)

57. Eduardo-Roman H. and Yussouff M., 1987 *Phys. Rev. B* **36** 7285

58. Sandler J., Shaffer M.S.P., Prasse T., Bauhofer W., Schulte K. and Windle A.H. 1999 *Polymer* **40** 5967

59. Cembrola R.J., 1982 *Polym. Eng. Sci.,* **22** 601

60. Yu G., Zhang M.Q. and Zeng H.M. 1998, *J. Appl. Polym. Sci.,* **70** 559

61. Hunter R.J. 2001 *Foundations of Colloid Science* (Oxford, England: Oxford University Press)

62. Lu J.P. 1997 *Phys. Rev. Lett.* **79** 1297

63. Tambo N. and Watanabe Y. 1979 *Water Res.* **13** 409

64. Frogley M.D., Ravich D. and Wagner D.H. 2003 *Compos. Sci. Tech.* **63** 1647

65. Kusy R.P 1977 *J. Appl. Phys.* **48** 5301

66. Serra T., Colomer J. and Casamitjana X. 1997 *J. Colloid. Interf. Sci.* **187** 466

APPENDIX A

THRESHOLDING ALGORITHMS

Any m x n grayscale image may be denoted by the discrete function I(x,y), subject to

$1 \leq x \leq m$; $1 \leq y \leq n$

$0 \leq I(x,y) \leq 255$ (for an 8-bit grayscale image)

Thresholding involves choosing a "threshold" grayscale value and segmenting the image according to

If $I(x,y) \geq T$ then $I(x,y) = 255$ [object]

Else $I(x,y) = 0$ [background]

Here, T is the threshold value computed by the thresholding algorithm

Iso-Data Thresholding Algorithm:

1. Choose starting threshold T_0 as half the range of intensities (in this case, 128)

2. Compute a new threshold value as

$$T_{new} = \frac{\left(m_{f,old} + m_{b,old}\right)}{2} \tag{A.1}$$

    where

      $m_{f,old} =$ mean of all I(x,y) satisfying $I(x,y) \geq T_{old}$

      $m_{b,old} =$ mean of all I(x,y) satisfying $I(x,y) < T_{old}$

3. This process is repeated until $T_{new} = T_{old}$

Maximum Entropy Algorithm:

1. Compute probability of occurrence of each grayscale value as

$$p_i = \frac{n_i}{N} \tag{A.2}$$

   where

   $n_i =$ number of occurrences of grayscale value i

   $N =$ total number of pixels

2. For all t in the range 0 to 255, compute the following sums:

$$H_b(t) = -\sum_{i=0}^{t} \frac{p_i}{P_t} \ln\left(\frac{p_i}{P_t}\right)$$

$$H_w(t) = -\sum_{i=t+1}^{255} \frac{p_i}{1-P_t} \ln\left(\frac{p_i}{1-P_t}\right) \tag{A.3}$$

   with $P_t = \sum_{i=0}^{t} p_i$

3. The optimum threshold T is chosen to be the value of t for which the sum

   $H_b(t)+H_w(t)$ is maximum

APPENDIX B

DERIVATION OF SEDIMENTATION EQUATIONS

Consider a container having cross sectional area A and filled to a height L with a liquid having a known volume fraction Φ of nanoparticles suspended in it, shown schematically in Figure B.1. If c(h) denotes the volume fraction of nanoparticles present at a height h, the total volume of nanoparticles V_N in the container is given by integrating the concentration, as given by the sedimentation equilibrium equation (3.2) as

$$V_N = A\int_0^L c(h)dh \tag{B.1}$$

and the total volume fraction is, therefore given by

$$\phi = \frac{Volume\ of\ Nanoparticles}{Volume\ of\ Container} = \frac{V_N}{AL} = \frac{1}{L}\int_0^L c_o \exp\left(\frac{-mgh}{k_BT}\right)dh \tag{B.2}$$

which gives

$$c_o = \frac{\phi Lmg}{k_BT}\left[1 - \exp\left(\frac{-mgL}{k_BT}\right)\right]^{-1} \tag{B.3}$$
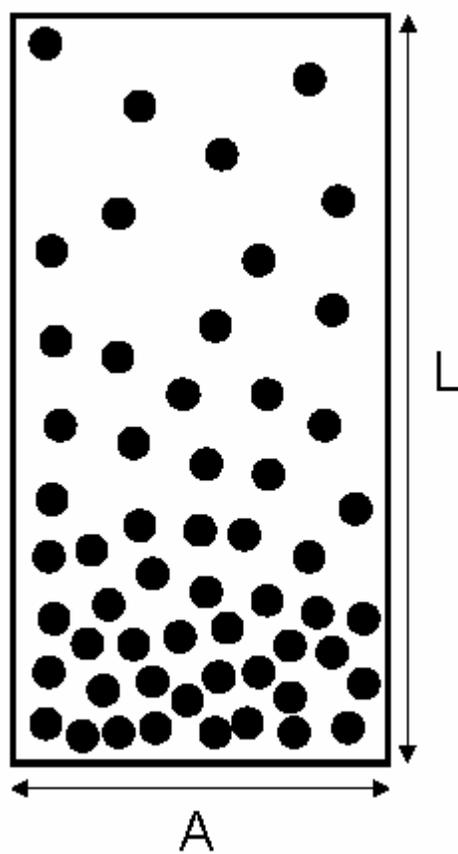
Figure B.1   Schematic of sedimentation equilibrium of colloidal particles

Similarly, the volume fraction of nanoparticles in the bottom, middle and top thirds of the container can be computed as

$$\phi_B = \frac{V_N}{A\dfrac{L}{3}} = \frac{3}{L}\int_0^{L/3} c(h)dh \tag{B.4.a}$$

$$\phi_M = \frac{V_N}{A\dfrac{L}{3}} = \frac{3}{L}\int_{L/3}^{2L/3} c(h)dh \tag{B.4.b}$$

$$\phi_T = \frac{V_N}{A\dfrac{L}{3}} = \frac{3}{L}\int_{2L/3}^{L} c(h)dh \tag{B.4.c}$$

APPENDIX C

IMAGE ANALYSIS SCRIPTS

(1) Iso-Data Thresholding

```matlab
% This Function Thresholds a given image based on the ISO-DATA
% Algorithm
% Inputs: Image matrix, Start threshold value
% Output: Thresholded Image

function [b]=thresh(a,anew_t)
b=a;
c=b;
prev_t=0;
prev_t=double(prev_t);
new_t=anew_t;
new_t=double(new_t);
sizes=size(a);
imax=sizes(1,1);
jmax=sizes(1,2);
while abs(prev_t-new_t)>0.000000001
    c=b;
    prev_t=new_t;
    up_sum=0.0;
    u_count=0;
    d_count=0;
    down_sum=0.0;
    for i=1:imax
        for j=1:jmax
            if(b(i,j)>=new_t)
                up_sum=up_sum+double(b(i,j));
                u_count=u_count+1;
            else
                down_sum=down_sum+double(b(i,j));
                d_count=d_count+1;
            end
        end
    end
    if(up_sum<=0)
        u_avg=0;
    else
        u_avg=up_sum/u_count;
    end
    if(down_sum<=0)
        d_avg=0;
    else
        d_avg=down_sum/d_count;
```

```
            end
        new_t=(u_avg+d_avg)/2;
    end
    for i=1:imax
        for j=1:jmax
            if(b(i,j)>=new_t)
                b(i,j)=255;
            else
                b(i,j)=0;
            end
        end
    end
```

(2) Maximum Entropy Thresholding

```
% This function thresholds images based on the maximum entropy
% thresholding algorithm
% Inputs: Image
% Output: Thresholded Image

function [ret]=ethresh(im)

sizes=size(im);
probs=zeros(256,1);
ret=im;
for i=1:sizes(1)
    for j=1:sizes(2)
        probs(im(i,j)+1)=probs(im(i,j)+1)+1;
    end
end
probs=probs/(sizes(1)*sizes(2));
maxsum=0;
t_opt=0;
for t=0:255
    h_b=0;
    h_w=0;
    pt=sum(probs(1:t+1));
    for i=0:t
        if(pt~=0)
            pp=probs(i+1)/pt;
        else
            pp=0;
        end

        if(pp~=0)
            h_b=h_b-pp*log(pp);
        end
    end
    for i=t+1:255
        if(pt~=1)
            pp=probs(i+1)/(1-pt);
```

```
            else
                pp=0;
            end
            if(pp~=0)
                h_w=h_w-pp*log(pp);
            end
        end
        if( (h_b+h_w) > maxsum)
            maxsum=h_b+h_w;
            t_opt=t+1;
        end
    end
    for i=1:sizes(1)
        for j=1:sizes(2)
            if(im(i,j)>=t_opt)
                ret(i,j)=255;
            else
                ret(i,j)=0;
            end
        end
    end
end
```

(3) Entropy calculation: Method A

```
% This function computes image entropy (method A)
% Inputs: Image, Bin size (odd number)
% Output: Image of computed entropies

function [ret]=iment(im,bin)

sizes=size(im);
ret=zeros(sizes);
halfbin=int16(bin/2);
halfbin=double(halfbin);
binsq=bin*bin
for i_cent=halfbin:sizes(1)-halfbin+1
    for j_cent=halfbin:sizes(2)-halfbin+1
        probs=zeros(256,1);
        for i=i_cent-halfbin+1:i_cent+halfbin-1
            for j=j_cent-halfbin+1:j_cent+halfbin-1
                probs(im(i,j)+1)=probs(im(i,j)+1)+1;
            end
        end
        probs=probs/(binsq);
        entr=0;
        for i=1:256
            if(probs(i)~=0)
                entr=entr-probs(i)*log(probs(i));
            end
        end
        ret(i_cent,j_cent)=entr;
```

```
        end
        disp(strcat(num2str(i_cent),'/',num2str(sizes(1))));
    end
    ret=ret(halfbin:sizes(1)-halfbin+1,halfbin:sizes(2)-halfbin+1);
```

(4) Entropy Calculation: Method B

```
% This function computes single species entropy over
% a set of images
% Images are stored in current directory
% Filenames may be changed
% fnam = Filename
% f_tot = Number of last file
% bindim = bin size (in pixels)
% bindet(i) = Number of particles in bin i
% Function Returns:
%   1. Entropy
%   2. Total Number of Bins
%   3. Total Number of Particles

function [ret1 ret2 ret3]=ent(bindim)

fnam='t';
f_tot=33;
particles=0;
totpix=0;
binnum=1;
for files=1:f_tot
    im=imread(strcat(fnam,num2str(files),'.tif'));
    imsiz=size(im);
    if(imsiz(1)==768)
        im=im(1:691,:);
    else
        im=im(1:2073,:);
    end
    imsiz=size(im);
    irem=rem(imsiz(1),bindim);
    jrem=rem(imsiz(2),bindim);
    im=im(1:imsiz(1)-irem,1:imsiz(2)-jrem);
    imsiz=size(im);
    for i=1:imsiz(1)/bindim
        for j=1:imsiz(2)/bindim
            i_st=(i-1)*bindim+1;
            i_end=i*bindim;
            j_st=(j-1)*bindim+1;
            j_end=j*bindim;
            p_count=0;
            for ii=i_st:i_end
                for jj=j_st:j_end
                    if(im(ii,jj)==255)
                        p_count=p_count+1;
                    end
```

```
                end
            end
            bindet(binnum)=p_count;
            binnum=binnum+1;
        end
    end
end
ret3=sum(bindet);
prob=bindet/ret3;
log_p=log(prob);
siz=size(log_p);
siz=siz(2);
for i=1:siz
    if(log_p(i)==-Inf)
        log_p(i)=0;
    end
end
ret1=-sum(immultiply(prob,log_p));
ret2=binnum-1;
```

VITA

Name: Santhana Gopinath Ganapathy Subramanian

Date and Place of Birth: October 21, 1978

                               Bombay, Maharashtra

                               India

Permanent Address: "Gananath", No. 25,

                               Fourth Cross,

                               Jaibharath Nagar,

                               Bangalore, Karnataka 560 033

                               India

Education: B.E. (Mechanical Engineering), December 2000

                               University of Mysore, Mysore, India

                               M.S. (Mechanical Engineering), December 2003

                               Texas A&M University, College Station, Texas

                               Ph.D. (Mechanical Engineering), August 2006

                               Texas A&M University, College Station, Texas